Universitat de Girona

AUTOMATIC SOURCE DETECTION IN ASTRONOMICAL IMAGES

Marc MASIAS MOYSET

Dipòsit legal: Gi. 1373-2014
http://hdl.handle.net/10803/275990

PhD Thesis

Automatic source detection in astronomical images

Marc Masias Moyset

2014

PhD Thesis

Automatic source detection in astronomical images

Marc Masias Moyset

2014

Doctoral Programme in Technology

Supervised by:

Jordi Freixenet, Marta Peracaula and Xavier Lladó

Work submitted to the University of Girona in partial fulfilment of the requirements for the degree of Doctor of Philosophy

Publications

Journals

- [**A&C 2014**] M. Masias, X. Lladó, M. Peracaula and J. Freixenet. "Multiscale distilled sensing: astronomical source detection in long wavelength images". Astronomy and Computing, submitted.

- [**NewA 2014**] M. Peracaula, A. Torrent, M. Masias, X. Lladó, J. Freixenet, J. Martí, J.R. Sánchez-Sutil, A.J. Muñoz-Arjonilla and J.M. Paredes. "Exploring three faint source detections methods for aperture synthesis radio images". New Astronomy, submitted.

- [**ExA 2013**] M. Masias, M. Peracaula, J. Freixenet and X. Lladó. "A quantitative analysis of source detection approaches in optical, infrared, and radio astronomical images". Experimental Astronomy, 36(3), pp. 591-629. 2013.

- [**MNRAS 2012**] M. Masias, J. Freixenet, X. Lladó and M. Peracaula. "A review of source detection approaches in astronomical images". Monthly Notices of the Royal Astronomical Society, 422(2), pp. 1674-1689. 2012.

Conferences

- [**ADASS 2013**] M. Masias, J. Freixenet, M. Peracaula and X. Lladṕ. "Multiscale source detection for long wavelength astronomical images". 23rd International Conference on Astronomical Data Analysis Software and Systems. ASP Conference Series, to appear. Waikoloa, Hawaii, USA. October 2013.

- [**ICIP 2013**] M. Masias, X. Lladó, M. Peracaula and J. Freixenet. "Multiscale distilled sensing: a source detection method for infrared and radio astronomical

images". 2013 IEEE International Conference on Image Processing. ICIP 2013 - Proceedings, pp. 2378-2382. Melbourne, Australia. September 2013.

- [**ADASS 2011**] M. Masias, J. Freixenet, X. Lladó and M. Peracaula. "Quantitative evaluation of source detection strategies in astronomical images". 21st International Conference on Astronomical Data Analysis Software and Systems. ASP Conference Series, 461, pp. 793-796. Paris, France. November 2011.

List of Acronyms

AIPS Astronomical Image Processing System

ALMA Atacama Large Millimeter/submillimeter Array

ATCA Australia Telescope Compact Array

CCD Charge-Coupled Device

CGPS Canadian Galactic Plane Survey

CRT Continuous Ridgelet Transform

CC-trees Connected Component trees

Dec Declination

DS Distilled Sensing

ESD Extended Source Detection

FDR False Discovery Rate

FITS Flexible Image Transport System

FN False Negative

FP False Positive

FSD Faint Source Detection

FWHM Full Width at Half Maximum

GALEX Galaxy Evolution Explorer

GMRT Giant Metrewave Radio Telescope

GN González-Nuevo

HDU Header and Data Units

HST Hubble Space Telescope

INTEGRAL INTErnational Gamma-Ray Astrophysics Laboratory

ISO Infrared Space Observatory

MAP Maximum-A-Posteriori

MCMC Markov-Chain Monte Carlo

MDS Multiscale Distilled Sensing

MF Matched Filter

MHWF Mexican Hat Wavelet Family

MHWT Mexican Hat Wavelet Transform

MSVST Multiscale Variance Stabilisation Transform

MVM Multiscale Vision Model

NVSS NRAO VLA Sky Survey

PCA Principal Component Analysis

PCA-NN Principal Component Analysis Neural Networks

PDS Phoenix Deep Survey

PRF Point Response Function

PSD Point Source Detection

PSF Point Spread Function

RA Right Ascension

RCF Radial Contrast Function

SAD Search And Destroy

SD Source Detection

SDSS Sloan Digital Sky Survey

SE Structural Element

SKA Square Kilometre Array

SNR Signal-to-Noise Ratio

SOFIA Stratospheric Observatory For Infrared Astronomy

SWT Stationary Wavelet Transform

TN True Negative

TP True Positive

TSD True Sources Detected

VICOROB Computer Vision and Robotics

WALT Wavelets And Local Thresholding

WISE Wide-field Infrared Survey Explorer

WT Wavelet Transform

XMM-Newton X-ray Multi-Mirror Mission-Newton

List of Figures

List of Tables

Contents

Resum

Aquesta tesi se centra en la detecció automàtica de fonts (objectes) en imatges astronòmiques. L'ús d'eines automàtiques per a realitzar aquest tipus de tasca esdevé d'una gran importància en l'àmbit astronòmic degut a la creixent quantitat de dades i a la ineficiència i imprecisió de les inspeccions manuals. En primer lloc, s'analitza de forma exhaustiva l'estat de l'art d'aquest tema, presentant una nova classificació de tècniques i destacant els seus principals punts forts i febles. Complementàriament, també es proporciona una avaluació quantitativa d'alguns dels mètodes més destacats. En segon lloc, es presenten tres propostes diferents per a la detecció de fonts febles en imatges de radiointerferometria (síntesi d'obertura): la primera, anomenada WALT, combina la transformada wavelet amb una binarització local; la segona, anomenada RCF, es basa en el comportament estructural d'una funció de contrast radial; i la tercera, realitza una classificació supervisada de píxels per mitjà de característiques locals i d'un mètode de boosting. Finalment, també es presenta una nova proposta per tractar amb imatges infraroges i de radiofreqüència. Aquest mètode, anomenat multiscale distilled sensing (MDS), es basa en l'ús combinat de la transformada wavelet i un mètode molt innovador anomenat distilled sensing. Els resultats experimentals i l'avaluació duta a terme amb imatges sintètiques i reals han demostrat que el rendiment de les quatre propostes és millor que el d'altres mètodes de l'estat de l'art, tant pel que fa a fiabilitat com a completesa.

Resumen

Esta tesis se centra en la detección automática de fuentes (objetos) en imágenes astronómicas. El uso de herramientas automáticas para realizar este tipo de tarea es sumamente importante en el ámbito astronómico debido a la creciente cantidad de datos e a la ineficiencia e imprecisión de las inspecciones manuales. En primer lugar, se analiza de forma exhaustiva el estado del arte de este tema, presentando una nueva clasificación de técnicas y destacando sus puntos fuertes y débiles. Complementariamente, también se proporciona una avaluación cuantitativa de algunos de los métodos más destacados. En segundo lugar, se presentan tres propuestas diferentes para la detección de fuentes débiles en imágenes de radiointerferometría (síntesis de apertura): la primera, llamada WALT, combina la transformada wavelet con una binarización local; la segunda, llamada RCF, se basa en el comportamiento estructural de una función de contraste radial; y la tercera, realiza una clasificación supervisada de píxeles mediante características locales y un método de boosting. Finalmente, también se presenta una nueva propuesta para tratar con imágenes infrarrojas y de radiofrecuencia. Este método, llamado multiscale distilled sensing (MDS), se basa en el uso combinado de la transformada wavelet y un método muy innovador llamado distilled sensing. Los resultados experimentales y la avaluación llevada a cabo con imágenes sintéticas y reales han demostrado que el rendimiento de las cuatro propuestas es mejor que el de otros métodos del estado del arte, tanto en cuanto a fiabilidad como a completitud.

Abstract

This thesis is focused on the automatic detection of sources (objects) in astronomical images. The use of automatic algorithms to perform such a task becomes of great importance in the astronomical field because of the increasing amount of data and the inefficiency and inaccuracy of manual inspection. In the first place, we exhaustively analyze the state of the art on this topic, presenting a new classification of techniques and pointing out their main strengths and weaknesses. A complementary quantitative evaluation of some of the most remarkable methods in the literature is also provided. Afterwards, we present three different proposals to detect faint sources in radio aperture synthesis images: the first, a method that combines the multiscale wavelet transform and local thresholding (WALT); the second, a method based on the structural behaviour of an intensity radial contrast function (RCF); and the third, a supervised method that classifies pixels by means of local features (filtered patches) and a boosting classifier. Finally, we also present a new proposal to deal with infrared and radio images. This method, called multiscale distilled sensing (MDS), is based on the combined use of the wavelet transform and an innovative method called distilled sensing. The experimental results and the evaluation performed with synthetic and real data points out that the performances of our four proposals are better than state-of-the-art approaches in terms of both reliability and completeness of the detections provided.

Chapter 1

Introduction

The universe contains billions of astronomical objects in constant evolution. With the desire of better understanding the cosmos, astronomers obtain thousands of images of these objects. These astronomical images provide information about the great variety of celestial objects (sources) existing in the universe, the physical processes taking place in them, and the formation and evolution of the cosmos. Over the last few years high-resolution mappings and catalogues of astronomical objects have been published by many observatories that use vanguard technology located both on the Earth's surface and in orbit [1, 19, 95, 68, 4]. These telescopes work not only in the optical domain, but in the whole range of the electromagnetic spectrum. Therefore, it is a common practice to acquire images with instruments that capture photons of frequencies not perceptible to human eyes like radio frequencies or X-rays [10].

Observing the same section of sky at different frequencies produces different types of images. Combined and comparative analyses of these images provide more comprehensive information about the objects in this area. However, detecting objects in astronomical images is not an easy task even for experienced astronomers. They are at distances measured in light-years, so it is very likely that they will appear as faint bright points or blended with other objects. Also, it is possible that some spots in these images may be considered as objects when actually they are not. For all these reasons, astronomical images need an exhaustive analysis in order to detect precisely when an object is present and when not. The optimal way to carry out these analyses would be with astronomical experts searching for the various objects to be found in these images. However, due to the large amount of data and the fact that many objects can be almost imperceptible, a search by humans is inefficient, very slow, and inaccurate, if not almost impossible. Hence, it is necessary to develop highly robust, fast, efficient, and computer automated algorithms to detect the astronomical objects by means of image processing and computer

vision techniques.

The automatic detection of sources in astronomical images seems to be quite a straightforward task compared to other computer vision problems: the typical scenario is dealing with light-emitting sources on dark backgrounds. Nevertheless, there are some difficulties associated with astronomical images that make this a complicated task. On the one hand, many astronomical objects do not show clear boundaries since their intensities are similar to the detection levels (i.e. those close to the background level) and they are mixed with noise components. On the other hand, especially in the case of wide-field deep images showing multiple sources, the sizes and intensities of the different objects present may vary considerably. Therefore, the images can have a high dynamic range (i.e. ratio between the highest and lowest intensity level) and a large spatial dynamic range (i.e. ratio between the largest and smallest detectable structure). These facts may cause image display problems due to the limited range of intensities perceptible by human vision.

Therefore, the main challenge of object detection in astronomical images is to separate those pixels that belong to astronomical bodies from those that belong to the background or noise to be able to specify the coordinates where these bodies are located afterwards. Since this goal may require searching through connected regions of pixels constituting objects, this task is also referred to as object segmentation in the computer vision community [82]. Nevertheless, in this document we will often refer to the localization of the central coordinates of the sources as detection. The final outcome of this detection process is a list of the objects' coordinates found (also known as the catalogue). The use of automatic tools to perform this task becomes of great importance in the astronomical field because of the increasing amount of data (usually many large-sized images per survey or observation with up to thousands of sources) and the inefficiency and inaccuracy of manual inspection.

1.1 Astronomical images

Despite the fact that all astronomical images are greyscale images with a high dynamic range, there are several types of images used for different purposes and with different characteristics.

1.1.1 Types of astronomical images

People are able to perceive visible light through their eyes. This light is within the electromagnetic spectrum through which the Sun emits most of its radiated energy. In fact,

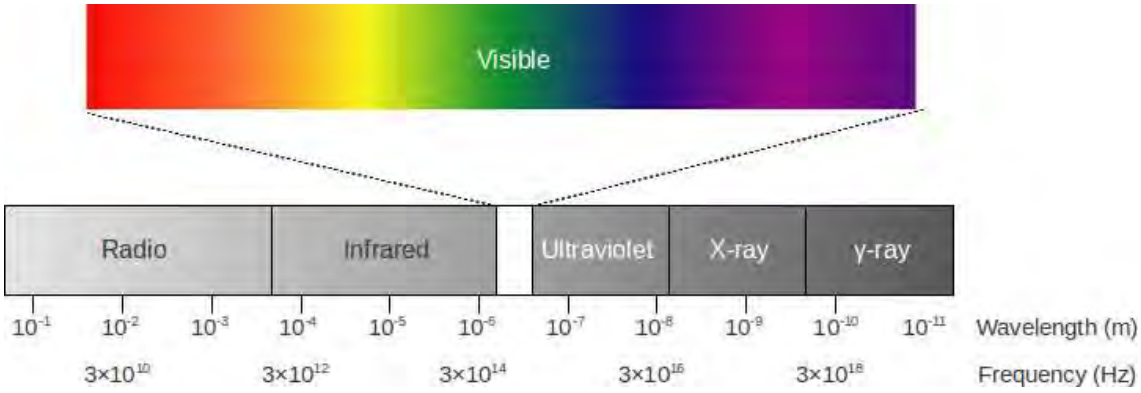

Figure 1.1: Electromagnetic spectrum.

visible light is only a small portion of all the electromagnetic radiation that travels through space. Initially, the study of the universe was focused mainly on the visible band, with the building of observatories that included optical telescopes with associated devices like spectrometers or photometers. However, due to the large amounts of relevant information in the invisible bands, astronomers also made efforts to develop an astronomy able to capture non-visible radiation emitted at different frequencies (and therefore, different wavelengths) as can be seen in the electromagnetic spectrum in Figure 1.1. On the one hand, there is radiation emitted at frequencies lower than the visible range (with wavelengths between 400 and 700 nm), such as radio and infrared. On the other hand, there is the radiation emitted at frequencies higher than the visible range, such as ultraviolet, X-rays, and γ-rays.

Various celestial bodies, gas, dust, and other elements may be visible at specific frequencies, and therefore, different types of images are used depending on the elements to visualize. Moreover, a common practice in astronomy is to superimpose images at different frequencies in order to combine the information provided at each band and are therefore called multiband images. An analysis of the sky at different frequencies allows the study of the phenomena of the universe, from the least energetic to the most, from the coolest to the hottest radiation.

Most non-visible bands, except for radio and the zones of infrared and ultraviolet near visible light, are blocked by the atmosphere, and for this reason, astronomy in these bands could not be developed until the advent of the space age in the sixties and seventies. Until this time, optical astronomy allowed astronomers to observe stars and other phenomena which emit at medium temperatures such as the sun. A couple of examples of optical

Figure 1.2: Two examples of telescopes. On the left, the Hubble Space Telescope in orbit. On the right, the ALMA interferometer.

telescopes are the Hubble Space Telescope [69] (shown in orbit in Figure 1.2, left) and the W. M. Keck Observatory [106] (in Hawaii). Nevertheless, astronomy at radio frequencies was developed in the thirties, before than at any other frequency, since it was directly linked to the development of the radio receiver. Radio astronomy is carried out by means of directional radio antennas and, unlike optical images, radio images have poor resolution (the ability to see in detail given by the ratio of the wavelength and the instrument diameter). The astronomers calculated that to achieve the same resolution in radio as with optical, they would need instruments 100,000 times greater (a non-viable size, since it is technologically impossible to build antennas over 100 meters). To solve this problem, they decided to form images by correlating (by pairs) the signal reached by multiple antennas located in fields, laid out in very large arrays (along kilometres). These antennas point to the same stellar object, but, as they are spaced out, the light reaches them at different moments albeit tiny, simulating a huge antenna with a diameter of kilometres. Afterwards, the different signals are correlated and, with some mathematical operations, a high resolution image is formed. The whole set of antennas is called a radio interferometer. Some examples of interferometers are the Very Large Array [95], the Very Long Baseline Array [68], the Atacama Large Millimeter/submillimeter Array (ALMA) [112] (shown in Figure 1.2, right) and the Square Kilometre Array (SKA) [18] (in development).

Astronomers can observe the so-called near-infrared (infrared radiation close to the visible part of the spectrum) with the same devices used in optical. The same happens with near-ultraviolet radiation. As infrared radiation moves away from visible light, the telescope must be placed at a higher altitude, even above the atmosphere. Infrared observations are used to observe emissions of cold clouds of gas and dust. Some examples

of infrared telescopes in space are the Herschel Space Observatory [79], the Spitzer Space Telescope [108], and the Wide-field Infrared Survey Explorer (WISE) [19], even though the Hubble Space Telescope can observe at near-infrared frequencies as well. Some others have been placed in aeroplanes, such as the Stratospheric Observatory for Infrared Astronomy (SOFIA) [24] or on the Earth's surface, such as the James Clerk Maxwell Telescope at the Keck Observatory. To achieve better resolution, there are even infrared interferometers, such as the one at the Keck Observatory.

Observations at high frequencies are usually performed from the upper atmosphere or from space using rockets and satellites. In ultraviolet, it is possible to visualize massive young stars and very old ones, which are very hot, and therefore, emit in an area of the spectrum close to blue and ultraviolet. Some examples of space telescopes that observe at ultraviolet frequencies are the Hubble Space Telescope (HST) and the Galaxy Evolution Explorer (GALEX) [60]. With X-rays, the energies are very high and show violent phenomena or sources with extremely hot gases. In γ-rays, very violent phenomena such as black holes, supernova explosions, or the destruction of atoms are especially detected. Some of the X-ray satellites in use today include the X-ray Multi-Mirror Mission-Newton (XMM-Newton) [45] and the Chandra X-ray Observatory [107], whereas some of the γ-ray satellites currently in orbit are the INTErnational Gamma-Ray Astrophysics Laboratory (INTEGRAL) [111], the Astro-Rivelatore Gamma a Immagini Leggero (AGILE) [66] and the Fermi Gamma-ray Space Telescope [4].

1.1.2 Celestial coordinate system

A common practice in astronomy is to measure the position of objects by means of a celestial coordinate system. They are usually spherical systems, although they also have a rectangular implementation. The most commonly used is the equatorial coordinate system which consists of projecting the latitudes and longitudes of the Earth onto the celestial sphere (an imaginary sphere concentric with Earth with a radius that can be considered as infinite). Equatorial coordinates are expressed as a pair: the latitudinal direction is called declination (Dec - measured in degrees from -90° to 90°) and the longitudinal direction is called right ascension (RA - measured in degrees from 0° to 360° or in hours from 0 to 24).

Other alternative celestial coordinate systems are used as well. The galactic coordinate system uses the Sun as the origin and the galactic plane (coincident with the plane of the Milky Way galaxy) as its fundamental plane. The galactic latitude (b - measured

in degrees from -90° to 90°) is the angular distance above or below the galactic plane, whereas the galactic longitude (l - measured in degrees from 0° to 360°) is the angular distance along the galactic plane. On the other hand, the ecliptic coordinate system uses the Earth as its origin and the ecliptic (the plane that includes the orbits of the Earth and the Sun) as its fundamental plane. The ecliptic latitude (measured in degrees from -90° to +90°) is the angular distance above or below the ecliptic, whereas the ecliptic longitude (measured in degrees from 0 to 360) is the angular distance along the ecliptic.

1.1.3 The FITS format

FITS is the acronym for Flexible Image Transport System [75] and is the standard computer data format widely used by astronomers to store, transmit and manipulate data files. Unlike many image formats, FITS is designed specifically for scientific data, and for this reason, it offers the possibility of attaching additional data as photometric and spatial calibration information. It is basically designed to store scientific datasets consisting of multidimensional arrays and 2-dimensional tables containing rows and columns of data. FITS is also often used to store non-image data, such as electromagnetic spectra, photon lists, data cubes, or even structured data. FITS files allow extensions containing data objects. For instance, one file may store different exposures of the same area of the sky such as X-rays and infrared exposures.

FITS was originally developed in the late seventies to provide a way to exchange astronomical data between computers of different types, with different word lengths, and different means to express numerical values. It was in 1981 when the first version of the FITS format became standardized, and after successive updates, the last version released was the 3.0, approved in July 2008.

The most commonly used type of FITS data is a data array of arbitrary dimension (for example, the image) and one or more headers. The file consists of several structures called HDU (header and data units) including a header and the data described by the header. The primary HDU contains an n-dimensional array of pixels (e.g. a 1-D spectrum, a 2-D image, or a 3-D data cube). Additional HDUs may appear after the primary one, and are called FITS extensions. Three types of extensions are available: image extensions, which are n-dimensional arrays of pixels, like in a primary array; ASCII table extensions, which are rows and columns of data in the ASCCI character format; and binary table extensions, which are rows and columns of data in a binary representation.

An interesting point is that the information is stored in headers in a humanly readable

way, so that users can examine the headers and understand the file's content such as the size, date and time, origin, coordinates, binary data format, free-form comments, history of the data, and anything else. For more detail, see the FITS standard [75].

1.2 Astronomical sources

An astronomical source is the origin of something that suggests the presence of an astronomical object. Hereafter we are going to use the terms source and object without distinction as those stellar bodies that can be detected in images.

Behind the sources detected we can find a variety of different astronomical bodies. For instance, in our own Solar System we find a star (the Sun), eight planets, at least five dwarf planets (objects massive enough to be nearly spherical and which have not cleared a path around a star), hundreds of natural satellites, thousands of comets and millions of asteroids, among others. Beyond the Solar System, apart from the objects already mentioned, we find an incalculable number of other sources such as stars and galaxies as well as gas, dust and cosmic rays.

Stars are basically composed of hydrogen and helium and are formed when a region achieves enough density of matter (gas and dust) due to a gravitational instability. Thus, a compact sphere with enough gravity at its center is formed. Afterwards, it starts to fuse hydrogen in its core producing large amounts of energy. Once the hydrogen in the core is exhausted (after up to billions of years), the evolution of the star depends on its mass, so that it can become a white dwarf (a stable cool star) or a red giant (a stable star that fuses hydrogen in a shell outside the core), or it can even explode: massive and binary stars may explode in a violent phenomenon called supernova, while white dwarfs may explode in a less energetic phenomenon called nova. A supernova remnant can form new astronomical bodies including new stars.

Groups of stars and stellar remnants, gas and dust gravitationally bound and evolving together in the Universe are known as galaxies. Depending on their morphology, they can be classified as elliptical, spiral or irregular. Interactions between galaxies are relatively frequent. For example, they may collide, which happens when one passes through the other. This collision may produce changes in the morphology of the galaxies. The interaction of gas and dust between the two galaxies produces disruptions and compressions and favours the appearance of zones of star formation. Some examples of stars and galaxies are shown in Figure 1.3.

Figure 1.3: Some examples of astronomical objects. On the left, several isolated stars, in the middle, a cluster of stars, and on the right, an elliptical galaxy. All these images have been extracted from the Hubble website [69].

1.2.1 Source morphology

Sources may present different shapes depending on the type of astronomical object they actually are. When the angular size of an object is smaller than the angular resolution of the telescope used to perform the observation, the object appears in images as a point source (also called unresolved). The response of a telescope to a point source is called the point spread function (PSF, although sometimes it is also known as the beam) [10]. It describes the two-dimensional distribution of light in the telescope's focal plane, and therefore, the representation of a point source in an image is the convolution of the object with the PSF, as shown in Figure 1.4. Hence, the size of a point source is given by the PSF of the acquisition instrument, and is usually measured through its full width at half maximum (FWHM). Great efforts are taken in order to reduce the size of the PSF in telescopes so that the signal is not spread out over too many pixels.

Point sources typically have only a few pixels, and because of this, are sometimes confused with image noise. On the other hand, sources that exceed the size of the PSF are commonly known as extended or resolved. They might still have compact spherical shapes (e.g. some distant galaxies) or be more irregular (e.g. supernova remnants). An example of an astronomical image with sources of different morphology is shown in Figure 1.5. Notice that saturating the image by changing the contrast, the structure of some extended sources is lost, but many faint sources appear.

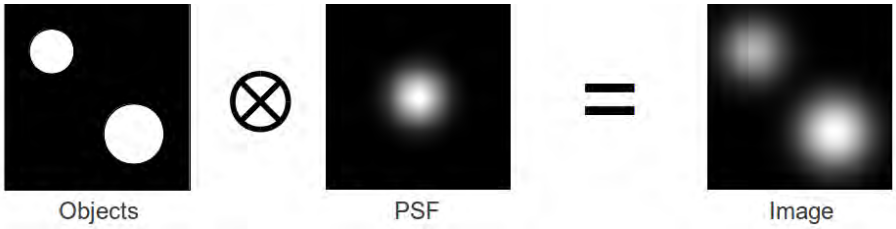

Figure 1.4: Graphical representation of the effect of the PSF in images.

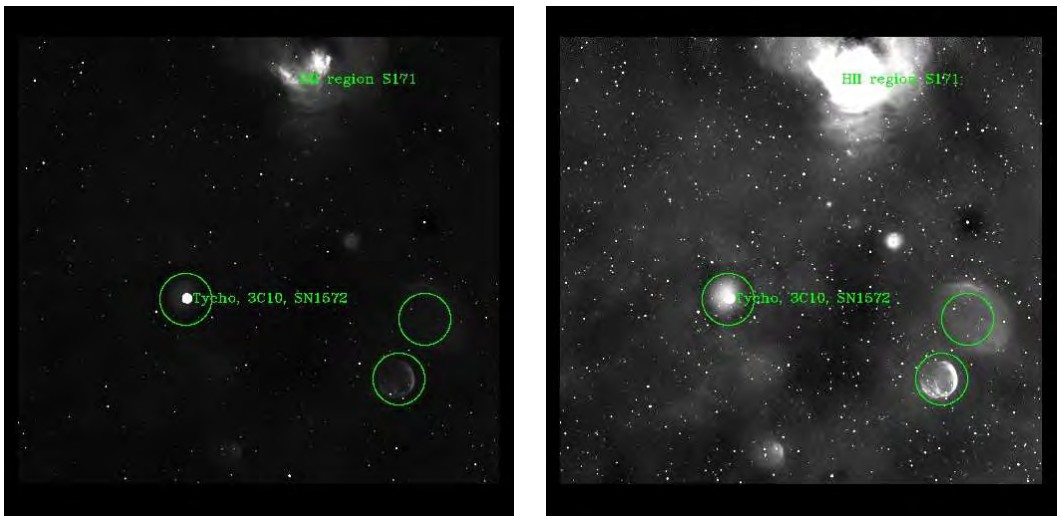

Figure 1.5: Radio image with different contrast stretching (0.1% of outliers eliminated on the left, and 2% on the right). These images contain extended sources encircled in green, irregular sources such as that at the top of the image, and multiple point sources.

1.3 Background and noise

In astronomical images, empty parts of the sky are known as the background. Hereafter, we talk about the background and the sky without distinction. Even if an object is not present in these regions of the sky, a low luminosity mostly due to the light emitted by nearby sources, is always present. Images taken through the atmosphere may be polluted by light from man-made sources such as cities. Some regions of the background may be considered as such by human eyes, however, they may hide sources visible in other frequency bands or those so faint that they are detectable only by computer tools. Furthermore, the background is diffuse, meaning that it is difficult to specify the exact line that indicates where the sources end and where the background begins. Moreover, the background is normally non-homogeneous due to the fact that some astronomical images need a long exposure time. Also, there are changes in the atmospheric conditions so sometimes they are mosaics made up of different images pointing at different coordinates at different moments, as can be seen in Figure 1.6.

Astronomical images are characterized by the presence of noise. It is one of the main disadvantages in astronomical detection, since it makes the detection process difficult. There are different types of noise according to their origin, such as shot, thermal and readout. Shot noise is due to the random variations in the number of light photons acquired by the instruments; thermal noise is due to the intrinsic thermal fluctuations in the acquisition devices that knock some electrons free; and the readout noise is due to the imperfect conversion from an analogue signal to a digital value in an electronic device [43]. Noise in images is usually taken as additive Gaussian and/or Poisson. For instance, in CCD (Charge-Coupled Device) images, the arrival of photons may generate Poisson noise while readout noise is commonly Gaussian. However, to simplify, in longer wavelength bands (basically optical, infrared and radio), the noise and the background are assumed to follow a Gaussian distribution. On the other hand, shorter wavelength bands present mainly Poisson noise since they are acquired by means of photon counters [91]. The amount of noise can be measured through the so-called signal-to-noise ratio (SNR), which is a measure used in many fields to quantify how much a signal has been corrupted by noise. It is calculated by dividing the amount of signal by the amount of noise (see the next chapter for more information), and therefore, the higher the ratio, the lesser the noise impact. Noise can sometimes be estimated through knowledge of the instrument's properties.

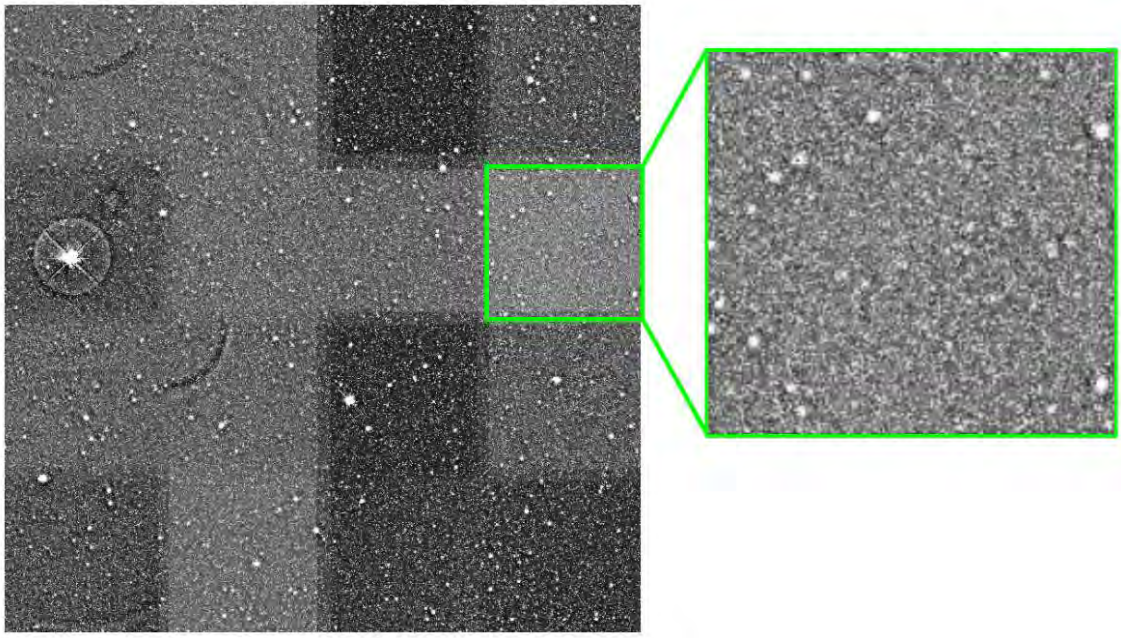

Figure 1.6: An infrared mosaic with background variations. This image, courtesy of Dr. J. Martí (private communication), is quite noisy and even presents some interferences (the darker curved regions at the top left of the image).

1.4 Astronomical imaging pipeline

In an astronomical imaging pipeline, also known as data reduction, several steps are carried out in order to generate the catalogues with features of the objects present in a region of the sky. An astronomical catalogue is a list of known astronomical objects that share a common type, morphology, origin or detection method. Astronomical catalogues are usually the outcome of a general map or image of a region of the sky (this is also known as an astronomical survey).

1.4.1 Acquisition process

Astronomical observations are made in observatories by means of large telescopes. The most widely-used telescopes are optical, able to observe the visible light emitted by stellar bodies and some wavelengths of ultraviolet and infrared bands. These telescopes are generally composed of two or three reflector mirrors or lenses to gather and focus light photons. Sometimes, some filters are used in the telescope to select specific zones of the electromagnetic spectrum (a set of these filters covering an important part of the spectrum is known as a photometric system). They are usually placed in large observatories in high places like mountaintops to take advantage of optimal climatic conditions such as clear skies or dry environments due to thermal inversion as dampness is below the observatories' location. As the atmosphere may distort the observations (the blurring and twinkling of objects caused by turbulences in the atmosphere is called seeing), sometimes these telescopes and some at other wavelengths, are placed at higher altitudes using aeroplanes and satellites. Following similar principles, there are other types of telescopes according to the band they observe. Most of them, such as infrared, ultraviolet, X-ray, and γ-ray telescopes, are found above the atmosphere.

In order to form a radiation image that reaches the telescope, a CCD camera is frequently used. They are used mainly due to their high sensitivity to most of the electromagnetic spectrum, especially the visible range, their linear response to the light, their reduced size, and their low cost. CCD cameras have an array of CCD sensors, each of which corresponds to a pixel in the image. These sensors are based on the photoelectric effect, which converts its received light into electric current to be translated to a pixel intensity in the digital image afterwards. CCD cameras are able to capture visible, ultraviolet, infrared (although in this band, infrared detector arrays are used as well) and even X-ray bands.

On the other hand, as we have already mentioned, radio frequencies are captured

through directional radio antennas. To have high resolution in radio, interferometry must be used, which reaches radio emissions with large arrays of antennas. Moreover, to preserve an angular resolution (antennas have a concave shape), a technique called aperture synthesis is used. This technique simulates the distribution of the set of antennas by mathematical corrections, taking into account the shape the huge simulated antenna should have (a parabola or a dish shape). In radio, the image is formed by the interpretation of the signal reached by the interferometer. In γ-rays (and sometimes also in X-rays), the image is generally created by photon counters.

1.4.2 Preprocessing

Several preprocessing steps are used to remove instrumental signatures from the data. For instance, a typical practice in CCD imaging is to calibrate the data by means of bias and dark current subtraction and flat fielding. Bias frames are images taken with no light (shutter closed) and with an exposure time of zero used to measure the signal of the CCD pixels; dark frames are images taken with no light in a given exposure time used to measure the dark current due to the thermal emission of the CCD pixels; and the flat fields are images taken when a homogeneous source of light is exposed and are used to measure the light sensitivity of the CCD pixels [43].

Some pixels in the image may be missing or corrupt (they are also known as bad or dead pixels) due to defects in the CCD or to cosmic rays (high energy particles). Some techniques used to deal with these outliers are, for instance, simple filtering, image reconstruction (such as replacements or interpolations) or inpainting. Additionally, to attenuate background variations such as noise or interferences, several instances of the same observation can be taken and pixel means or medians can be performed [114, 32, 115, 88].

In radio interferometric images, where strong fringe patters are usually present, image restoration through deconvolution is commonly used. The so-called CLEAN algorithm [39] is the most widely used algorithm in these images. It iteratively searches peaks (sources) in the image, subtracts the gain of the beam at these peaks and convolves them with an idealized beam (usually a Gaussian).

1.4.3 Source extraction

Source detection can be considered as the first step of source extraction and consists of extracting properties and characteristics of the objects present in an astronomical image.

Once the sources are located, a common practice is to measure their intensity radiation (also known as flux). This process is called photometry and can provide information about the structure of the object, its temperature, distance or age. Photometry techniques aim to measure the light emitted by the source and discard the light from the sky. Two different types of photometry are commonly used: aperture and differential. In aperture photometry, the level of the sky is measured by averaging the intensity pixels of an annulus around the source center that do not include the source, and afterwards, this value is subtracted from the addition of the intensity of the pixels within a circle surrounding the source (aperture). On the other hand, differential photometry measures the brightness of the sources relative to reference sources with constant brightness. It is typically used to determine the evolution of variable stars.

In astronomy, the brightness can be measured in different ways. The amount of energy transferred to CCD pixels or photon counters is mostly measured in terms of flux in Jansky (Jy) units. However, the logarithmic measure of the brightness of the objects relative to stars of known brightness is widely used as well. It is so-called magnitude and can be calculated as follows:

$$m = m_{ref} - 2.5 \log_{10}(\frac{flux}{flux_{ref}}), \tag{1.1}$$

where m_{ref} is the photometric zero point: the magnitude of a star with a brightness considered as reference (the star Vega has been classically assumed to have zero magnitude). $flux_{ref}$ corresponds to the flux of the reference star. Note that the smaller the magnitude, the brighter the source. Additionally, flux in radio astronomy is sometimes measured in terms of brightness temperature (the temperature of a black body in thermal equilibrium) in K units.

The determination of the position of objects in terms of celestial coordinates is then carried out. This process is called astrometry and commonly uses the coordinates of sources in the image well-located in other catalogues to determine the position of objects in the image with unknown coordinates. Additionally, as many observations are performed pointing to well-known coordinates, this prior information can also be used to determine the astrometry in images.

Some source extraction methods also incorporate a source classification step to figure out the type of astronomical bodies behind the sources. For instance, some software applies star/galaxy classification or galaxy morphology determination steps.

1.5 Research framework

This thesis is located within the framework of two research projects in which the Computer Vision and Robotics (VICOROB) group [103] of the University of Girona [100] has been recently involved: "Observational and theoretical studies of high energy galactic sources from the radio to the VHE γ-rays" (reference AYA2007-68034-C03-03) awarded by the Ministerio de Educación y Ciencia (2008-2010), for which Dr. Marta Peracaula was responsible; and "High-energy phenomena in stellar objects. Theory and multiwavelength observations" (reference AYA2010-21782-C03-02) awarded by Ministerio de Ciencia e Innovación (2011-2013), for which Dr. Jordi Freixenet was responsible.

Both projects were coordinated by the teams of the Department of Astronomy and Meteorology [97] and the Institute of Sciences of the Cosmos [98] of the University of Barcelona [99], led by Dr. Josep Maria Paredes. The third member involved in the projects was the team of the Department of Physics of the University of Jaén [101], led by Dr. Josep Martí.

The main role of VICOROB in these projects was closely related to that of this thesis. It specifically consists of performing research on astronomical source detection algorithms in images of different natures, paying special attention to the development of detection and segmentation algorithms for radio images.

1.6 Objectives

As part of the two projects just mentioned, the main goal of this thesis is

the analysis and development of automatic algorithms to detect sources in astronomical images.

This goal refers to the building of catalogues containing the coordinates, in terms of pixels, of the centroid of sources present in images. This general objective can be divided into three specific parts pertaining to the different stages of this thesis:

1. **An exhaustive analysis of the state of the art in astronomical source detection**. This includes a review of the main methods used over the last few years as well as the proposal of a new classification of methods according to their main steps. This second task arises from the lack of an updated review of astronomical

detection techniques at the beginning of this thesis.

2. **A quantitative analysis of some of the most promising methods** found in the state of the art. This evaluation includes some of the most widely used detection algorithms as well as other innovative methods that have recently emerged. Included is the selection of an appropriate common dataset to level the playing field consisting of optical, infrared and radio images. Accurate catalogues of sources are also needed in order to evaluate the detection performance of the methods.

3. **The development of several proposals to automatically detect sources in different types of astronomical images**. Our main aim is the implementation of different methods able to deal with different types of images at different bands. However, as the research projects linked to this thesis are mainly focused on radio frequency images, more importance is given to the use of radio images. The results obtained with these proposals in different datasets will also be compared to those obtained with widely-used state-of-the-art methods.

1.7 Document structure

This thesis is structured as follows:

- **Chapter 1. Introduction**. This current chapter has explained the main points this thesis deals with, such as what is and what the automatic detection of sources in astronomical images involves. The planning and goals of this thesis have been presented as well. The following chapters explain, in detail, the current techniques in this field and introduce new proposals.

- **Chapter 2. Review of source detection in astronomical images**. After Chapter 1, a wide variety of astronomical detection techniques that have appeared over the last few years is analyzed, pointing out their main advantages and drawbacks in a qualitative way. We introduce a new classification based on the image transformations and the detection criteria the methods use. Finally, the performance of the methods is discussed according to their reported results.

- **Chapter 3. Quantitative evaluation of source detection methods**. After reviewing the different techniques used to detect sources in Chapter 2, we present a quantitative evaluation of some of the most salient methods found in the literature. They are tested with a unified dataset consisting of optical, infrared, and

radio frequency images. Respective catalogues of the images are used to evaluate the performance of these methods in terms of reliability of the detections obtained and the number of true sources in the catalogue correctly identified. An extended discussion is presented regarding the methods, the strategies they use and the type of images.

- **Chapter 4. Faint source detection in aperture synthesis radio images**. After the exhaustive evaluation of strategies in Chapters 2 and 3, three new approaches to detect faint sources based on different techniques are presented. They come out of what we considered as being some of the most interesting techniques in the state of the art: the first combines multiscale decomposition and local thresholding; the second performs a radial contrast analysis of neighbourhoods of pixels; whereas the third classifies pixels by means of local features and a boosting classifier. After testing them on radio interferometric datasets, their results are compared to those achieved with algorithms widely-used by the astronomical community.

- **Chapter 5. Multiscale source detection for long wavelength images**. Another proposal to deal with the detection of sources in radio and infrared images is presented in this chapter. It is based on the combination of commonly used multiscale transforms and the promising Distilled Sensing method. The combination of these methods allows a better performance than using only Distilled Sensing. The new proposal has been applied to different long wavelength datasets and the results obtained have been compared to commonly-used detection software.

- **Chapter 6. Conclusions**. This final chapter sums up the main conclusions extracted from this work. Based on these, possible solutions and future work are set out.

Chapter 2

Review of source detection in astronomical images

Astronomical detection is usually the first step in the process of building astronomical catalogues. For this reason, after astronomical detection, two other processes are also performed: classification, which categorizes the objects into different types (e.g. stars, clusters, galaxies, extended objects, etc.), and photometry, to account for the flux, magnitude or intensity of the objects. The whole process of building a catalogue is also known as source extraction.

The development of automated algorithms to detect astronomical objects has become a research topic of interest for the astronomical community. Even thought these algorithms perform the same actions that an experienced astronomer can do with an appropriate display system, their importance relies on the fact that algorithms can do these things quickly, repeatedly, and always with maximum objectivity (properties a person can not guarantee). As stated by Goderya and Lolling [25], their importance becomes apparent in wide fields or large surveys with thousands of sources that can have intensities at detection levels. In these cases, a human search is inefficient, very slow, and inaccurate, if not almost impossible.

The first automated methods for astronomical object detection had already been developed in the seventies, and have evolved until today, although at a relatively slow pace because simple image processing techniques are already used to achieve better results than those performed manually by experts. Nevertheless, more accurate and reliable detection techniques are increasingly required by astronomers so more complex strategies have been implemented.

We are aware that astronomical imaging is a broad subject and images acquired at

different frequency bands present different features and behaviours. However, we want to give an overview of the most used techniques to find astronomical sources regardless of the origin of the images employed. This does not mean that we obviate the importance of the type of image. By doing this general review we can see whether a given technique performs well with different types of images or if it is more suitable for a specific frequency band.

In this chapter we review the current state of the art in astronomical source detection [61], including a detailed analysis of these works, their classification according to the methods used, the image type, and the evaluation of their results. We propose a new classification based on two main steps: image transformation and detection criterion. The first consists of applying changes to the astronomical images to prepare them for further processing, whereas the second consists of classifying pixels that belong to sources and separating them from background pixels, or in finding those pixels where the sources are centred. Moreover, we also analyze the parameters of the strategies reviewed such as the type of image, the reference catalogue, the evaluation measures used and their performance. To the best of our knowledge, this is the first attempt to provide a quantitative and qualitative comparison of detection approaches according to their reported results in the literature.

2.1 Image transformation

Image transformation is a basic step used to prepare data to achieve a better performance in later steps. Before putting into practice some of the image processing steps, some operations may be applied to suppress undesired distortions or enhance some features for further processing. Image transformation steps transform raw images in some way, creating new images with the same information content as the originals, but with better conditions. Thus, the images are adapted to facilitate later analysis, and to obtain better results. In astronomical imaging, the objectives of image transformation are, for instance, to filter noise, to estimate the background or to highlight the objects.

Within this image transformation group, we find techniques such as filtering, deconvolution, transforms, or morphological operations. We present a formal and more accurate classification by dividing the image transformation steps into multiscale strategies, basic image transformations, Bayesian approaches, and matched-filter-based strategies. More information is given in Table 2.1, which presents the different works reviewed according to

the image transformation method, the type of image and the specified detection aim. The methods are grouped by their image transformation strategy. Notice that the different strategy aims may not be exclusive, but are simply the way authors referred to them.

2.1.1 Basic image transformation

We begin this image transformation review with a range of techniques that, although simple, offer good performance, and hence are widely used throughout the computer vision field. They are basically used to filter noise and estimate background level.

Simple filtering techniques such as median or average are used by many authors. They consist of a sliding window centred on a pixel that computes one of the statistics mentioned for all the pixels in the window, and, finally, replaces the central pixel with the computed value. For instance, the median filter was used by Damiani et al. [17] and Makovoz & Marleau [57] to estimate the background level and minimize the effect of bright point source light, while Yang et al. [113], Perret et al. [76], and Lang et al. [50] used it to filter noise and smooth the image. With these two aims, Herzog & Illingworth [37], Mighell [64] and Freeman et al. [21] used the mean filter. Notice that in some cases, pixels in the window with high values are removed to avoid biased values.

Background estimation is a common step in astronomical object detection. A good way to carry it out is by using the one used in well-known extraction packages such as Daophot [92] and SExtractor [6]. Their local background estimation is performed by iteratively applying a thresholding based on the mean and standard deviation to eliminate outliers. Afterwards, a value of the true background is calculated as a function of these statistics (Stetson suggested 3×median - 2×mean, while Bertin suggested 2.5×median - 1.5×mean). Some authors refer to this background estimation as σ-clipping. Others, such as Vikhlinin et al. [105], Lazzati et al. [52], Perret et al. [76] and Men'shchikov et al. [63] (in multiscale planes) also used this method to deal with the background estimation.

Some authors (Irwin [44], Le Fèvre et al. [53] and Slezak et al. [84]) mentioned that they use a method that Bijaoui [7] presented more than thirty years ago. It was based on a Bayesian estimation of the intensity at each point using the histogram of the densities. A model of this histogram was then built, taking into account the granulation and the signal distribution, and obtaining the best threshold to separate the sky from the foreground. Although at first it was a widely used background estimation strategy, it became less common due to its high computational cost.

Table 2.1: Summary of the methods' image transformation. Detection aims stand for: extended source detection (ESD), faint source detection (FSD), point source detection (PSD), and source detection (SD). The term 'n/a' stands for not available.

Article	Image transformation	Image type	Aim
	Basic image transformations		
Herzog & Illingworth (1977) [37]	Mean	Optical	SD
Le Fèvre et al. (1986) [53]	Bijaoui	Multiband	SD
Stetson (1987) [92]	σ-clipping + Gaussian	n/a	SD
Slezak, Bijaoui & Mars (1988) [84]	Gaussian + Bijaoui	Optical	SD
Bertin & Arnouts (1996) [6]	σ-clipping	n/a	SD
Szalay, Connolly & Szokoly (1999) [93]	Gaussian	Multiband	FSD
Mighell (1999) [64]	Mean	n/a	SD
Hopkins et al. (2002) [42]	Gaussian	Radio	SD
Aptoula, Lefèvre & Collet (2006) [3]	Morphological	Multiband	SD
Yang, Li & Zhang (2008) [113]	Median + Morphological	Optical	SD
Perret, Lefèvre & Collet (2008) [76]	σ-clipping + Median + Morphological	Multiband	SD
Haupt, Castro & Nowak (2009)[35]	Distilled Sensing	Radio	SD
Lang et al. (2010) [50]	Median	Multiband	PSD
Hadjiyska et al (2013) [31]	Asterisk median filter	Optical	SD
	Bayesian approaches		
Hobson & McLachlan (2003) [38]	Markov-chain	n/a	SD
Savage & Oliver (2007) [81]	Markov-chain	Infrared	SD
Feroz & Hobson (2008) [20]	Nested sampling	n/a	SD
Carvalho, Rocha & Hobson (2009) [15]	Multiple posterior maximisation	Optical	SD
Guglielmetti, Fischer & Dose (2009) [30]	Mixture model	X-ray	SD
Trott et al. (2011) [96]	Likelihood-ratio test	Radio	PSD
Klepser et al. (2012) [48]	Likelihood-ratio test	γ-ray	SD
	Matched filter		
Irwin (1985) [44]	Bijaoui + Matched filter	Optical	SD
Vikhlinin et al. (1995) [105]	σ-clipping + Matched filter	X-ray	SD
Makovoz & Marleau (2006) [57]	Median + Matched filter	Multiband	PSD
Melin, Bartlett & Delabrouille (2006) [62]	Matched multifilters	Radio and multiband	PSD
Herranz et al. (2009) [36]	Matched matrix filters	Radio	PSD
Lanz et al. (2012) [51]	Matched multifilters	Radio	PSD
	Multiscale approaches		
Bijaoui & Rué (1995) [9]	Wavelet	Optical	SD
Kaiser, Squires & Broadhurst (1995) [47]	Mexican Hat	Multiband	SD
Damiani et al. (1997) [17]	Gaussian + Median + Mexican Hat	X-ray	SD
Starck et al. (1999) [87]	Wavelet	Mid-infrared	FSD
Lazzati et al. (1999) [52]	σ-clipping	X-ray	SD
Freeman et al. (2002) [21]	Mean + Mexican Hat	X-ray	SD
Starck (2002) [86]	Wavelet + Ridgelet	Infrared	SD
Starck, Donoho & Candès (2003) [89]	Wavelet + Curvelet	Infrared	SD
Vielva et al. (2003) [104]	Mexican Hat (spherical)	Radio	PSD
Belbachir & Goebel (2005) [5]	Contourlet + Wavelet	Infrared	FSD
Bijaoui et al. (2005) [8]	Wavelet + PSF smoothing	Multiband	SD
González-Nuevo et al. (2006) [26]	Mexican Hat (family)	Radio	PSD
Starck et al. (2009) [90]	Multiscale Variance Stabilisation	γ-ray	SD
Broos et al. (2010) [11]	Wavelet	X-ray	SD
Men'shchikov et al (2012) [63]	Successive Unsharp Masking + σ-clipping	Infrared	SD

A recent work proposed by Hadjiyska et al. [31] used an asterisk median filter to estimate the background. A profile with two radii was defined, and only the pixels in the asterisk branches between the inner and the outer radii are used to calculate the neighbour median at that pixel.

Sometimes, when the background presents large variations or the noise level is high, a background subtraction is applied (Le Fèvre et al. [53] and Slezak et al. [84]. After the subtraction, the source detection process becomes easier. The background subtraction is usually performed from the background estimation, removing those pixels considered as background. Haupt et al. [35] developed a different method called Distilled Sensing, which was based on the idea of ruling out the regions where the signal (sources) was not present, and then focusing on the rest of the regions. They performed iterative thresholding to discard regions where the signal was absent, and then the source detection was intensified in the regions not discarded.

Another common image transformation step is to convolve the image with a Gaussian profile. In optical imaging, this process can be understood as an approximation to model the point spread function (PSF - the response of the acquisition instrument to a point source of intensity 1 unit) to the image pixels, thereby obtaining a new map with the probability that each pixel has to be part of an object. Gaussian fitting can be computed by subtracting the mean of the sky and dividing it by the Gaussian deviation. As Stetson [92] mentioned, Gaussian fitting is equivalent to going through each pixel and considering the expected brightness each one should have when an object is centred on it. A numerical answer to this question is estimated by fitting a Gaussian profile: if a star is truly centred on that pixel, it becomes a positive value proportional to the brightness of the object. Otherwise, the pixel value becomes close to zero or negative. Szalay et al. [93] and Hopkins et al. [42] also applied this strategy to multiband and radio frequency images. Moreover, Damiani et al. [17] in their multiscale approach, applied a Gaussian filter to the image in order to smooth the spatial variations of the background. Slezak et al. [84], also applied this convolution to optical images in order to enhance very faint objects.

Furthermore, Gaussian models may also be used to filter noise. Modelling the intensity of the image pixels as a Gaussian, the bell-shaped zone may be considered as noise, while the rest of the distribution may represent background and objects. This noise filtering by Gaussian fitting of the histogram was used by Slezak et al. [84].

Morphological operations are another typical image transformation step used in computer vision. A generalisation to greyscale images allows the morphological image trans-

formation step to be applied to this type of image. The two main operations in morphology are dilation and erosion. In binary images, white pixels are considered foreground, and black pixels are considered background. As its name suggests, dilation expands white pixels, replacing the patch around the pixel with a given structural element (SE - a mask with a specific shape), while erosion compresses the foreground by replacing a patch that matches with the SE for a unique white pixel. In other words, dilation adds pixels to the foreground edges, while erosion removes pixels from the edges. The combination of dilation and erosion (in this order) is called "close" operation, whereas the inverse process is called "open" operation. In greyscale morphology, structural elements are defined as functions.

The works that have used the morphological greyscale image transformation step include Aptoula et al. [3] and Yang et al. [113], who filtered the noise and enhanced the image by computing open and close operations. Another work based on morphology is Perret et al. [76]. They proposed the use of the grey level hit-or-miss transform (a morphological operator dedicated to template matching that uses an erosion and a pair of disjoint structuring elements). In this transform, the image is convolved with two different SE types: while the first one is used to match the object shape (foreground), the second is used to match the spatial neighbourhood of this shape (background). In the approach by Perret et al. [76], the SE corresponding to foreground and background are patches of objects with variations in orientation and elongation convolved with a Gaussian filter to simulate the PSF. A different grey level according to the background estimation is given to these patches to get, on the one hand, the foreground SE, and, on the other, the background SE. After the background estimation and noise filtering, the two SE are convolved with the image and the output score image can easily be thresholded.

2.1.2 Bayesian approaches

The goal of these approaches is to prepare the data in order to establish the probability that it is either object or background. In other words, the objective is to provide a probability map with higher values in the zones where an astronomical object is more likely to be located, and lower values in the zones that are more likely to be sky. Bayesian approaches are based on the widely used Bayesian inference, where a set of evidences or observations is used to update the probability that a hypothesis is true. Bayesian inference tries to estimate the values of a set of parameters O in some reasonable model (or hypothesis) of the data (in our case, the image I). For any given model, an expression of

the probability of obtaining the data set given a particular set of values for the parameters (this is the so-called likelihood) must be considered. Moreover, a prior probability of the parameters based on some knowledge regarding their values before analyzing the data must be imposed. The Bayesian approach consists of constructing the conditional probability density relationship:

$$p(O|I) = \frac{p(I|O)p(O)}{p(I)}, \tag{2.1}$$

which gives the posterior distribution $p(O|I)$ in terms of the likelihood $p(I|O)$, the prior $p(O)$ and the evidence $p(I)$.

For the purpose of estimating parameters, the evidence is usually set to a constant value, so it is usual to talk about unnormalized posterior distribution. It is called maximum-a-posteriori (MAP) solution, and we can see it as a maximisation over O that involves a maximum likelihood and a prior:

$$MAP(O) = \max_{O} p(I|O)p(O). \tag{2.2}$$

If we are able to assess the likelihood, then, after applying a prior, we will have the posterior probability, which is the final resulting image. It expresses the probability of the data I given any particular set of parameters O. In practice, the likelihood is often based on an exponential function that involves the data (the different pixels), the signal contribution and the noise model (Gaussian, Poisson, etc.).

Referring to the prior knowledge, noise characteristics and the PSF can be used. Any other fit parameters can also be assumed. For example, source position and amplitude may have already been determined in another observation band. Further information about Bayesian methodology is available at [91] and [34].

Hobson & McLachlan [38] studied two alternative strategies to detect discrete objects: the simultaneous detection of all discrete objects in the image, and the iterative detection of objects one by one. In both cases, the parameter characterisation of the objects of interest was carried out by means of a Markov-chain Monte Carlo sampling (MCMC) (see [38], [81], and references therein to find out more about MCMC). By using MCMC, they could sample numerically from an unnormalized posterior distribution. They used as prior knowledge the mean estimation of the number of objects per image (an empirical value). For instance, in the iterative detection method proposed by Hobson & McLachlan, this value was set to 1, because it was the number of objects to be found at each itera-

tion. In a similar way, Savage & Oliver [81] developed a filter to source detection (and a simultaneous background estimation) in infrared images. Moreover, using MCMC, they tried to determine the related probability at each pixel of being described by two different models: empty sky and point source against a uniform background. When calculating the maximum posterior value for each model (using the PSF as prior knowledge), a map with the probability of where a point source was more likely to be located was generated.

On the other hand, Feroz & Hobson [20], followed the Hobson & McLachlan approach, but they replaced the MCMC with another Monte Carlo technique; nested sampling. They used it to calculate the posterior distribution as a by-product. In a similar way, and also following the Hobson & McLachlan approach, Carvalho et al. [15] proposed an object detection method called PowellSnakes, computationally faster than Bayesian methods based on MCMC. In their approach, sampling was skipped and the detection method was applied directly to the posterior. An estimation of position, amplitude, and spatial shape of sources was estimated in order to be used as prior knowledge. Guglielmetti et al. [30] applied their Bayesian source detection method to X-ray images. They used two different kinds of prior knowledge: exponential and inverse-Gamma functions as probability density functions of sources, and two-dimensional thin plate splines (see references in [30]) to represent the background.

Other approaches, such as those of Trott et al. [96] and Klepser [48], used the so-called likelihood-ratio test. In both cases, the likelihoods of the data being empty sky (null hypothesis) and sources and sky (alternative hypothesis) were computed. Then the ratio was calculated by dividing the likelihood of the null hypothesis by the likelihood of the alternative, and hence, obtaining a probability map.

2.1.3 Matched filtering

The purpose of applying a filtering step is to highlight objects and reduce the background fluctuations. The most commonly used filter to solve these two problems is the matched filter (MF). This filter convolves the image with the profile of the objects that are expected to be found (e.g. PSF for point source detection or other patterns for extended source detection). In addition, the MF may be used to subtract the background locally, and is also a filter to consider when the images present a considerable amount of noise.

Many authors have proposed filtering raw images with an MF before applying a method to detect objects. In the eighties, Irwin [44] suggested the use of the seeing function as an MF to detect faint sources in a noisy background. The seeing function can be obtained

either by directly averaging suitable stellar profiles or by an analytic model fit to these profiles. A background estimation (following the Bijaoui [7] method) was also computed previously to correct spurious values and to homogenize the sky. The MF allowed the SNR to be increased, so the sources and the background were easily separated by a thresholding.

Vikhlinin et al. [105] proposed a similar strategy focused on X-ray data that, first of all, generated a background map using a sliding box thresholding that detected the brightest sources for removal. Afterwards, an MF defined as a piecewise function was applied to the residual image. Depending on two thresholds, obtained with the background estimation, the current pixel was convolved with a different function branch in order to differentiate between sources and background. Pixels that were source candidates were convolved with the instrument PSF, whereas pixels that were background candidates were convolved so that their values were zero or negative. Thus, a detection method could be applied to the resulting image. This process is repeated iteratively until a stop criterion is reached.

Another approach based on MF was developed by Makovoz & Marleau [57]. It was included in the Mopex package for astronomical image processing. To detect point sources, first and foremost, the background was subtracted from the image by locally calculating the median and subtracting it from the current pixel. Then, an MF based on a point response function (PRF) was applied to the background-subtracted image. With the background subtraction step, some bright sources could be extracted, and using patches of these sources, the PRF could be estimated. The detection process was repeated iteratively, so the PRF could be refined with the new sources extracted.

In the literature, some authors have also used MF with multiband images, the so-called matched multifilter. For example, Melin et al. [62] used this extension of the MF to detect clusters. Each band was convolved with its corresponding filter (they used knowledge of the cluster signal, such as its spatial and spectral features at each band), and a single filtered image was produced by combining all filtered bands. More recently, it has also been used by Lanz et al. [51]. In a similar way, Herranz et al. [36], introduced what they called matrix filters or matched matrix filters. The main difference was that they convolved each band with its corresponding filter, but a filtered image per band was generated so a final choice of which filtered bands were better to perform the detection step was needed.

2.1.4 Multiscale approaches

In computer vision, the concept of multiscale or multiresolution is often used when the image to be segmented shows objects with very different sizes or patterns organized in

a hierarchical structure. In astronomical image processing, multiscale approaches have been extensively used over the last fifteen years, mainly because, in many cases, they outperform other strategies based on more basic techniques.

Astronomical data generally has a complex hierarchical structure, and for this reason a more suitable way to represent it is in multiscale space. Thus, images are decomposed into components at different scales or different spatial frequencies, and objects become highlighted in some scales. Depending on the nature of the objects, they may appear in more or fewer scales, and closer to the low or high frequency scales. Once the decomposition is complete, a basic detection algorithm can be applied to the different scales as if they were single-scale images.

In other words, multiscale strategies optimize the analysis and detection of astronomical objects however complex they may be. Among their applications, we find denoising, source deblending (an astronomy technique to isolate overlapping sources) and inpainting (the process of reconstructing missed or deteriorated parts of images), among others.

Several multiscale decompositions are used in the literature. For instance, Men'shchikov et al. [63] recently used the so-called successive unsharp masking to decompose an image in different scales. It consists of convolving the original image with circular Gaussians and subtracting them from one another. However, the wavelet transform is the multiscale technique most used by far. This transform and other multiscale approaches, which focus on the detection of astronomical objects, are commented on below. See [28] and [91] for a more detailed description of wavelets and other multiscale transforms.

The wavelet transform

When we talk about multiscale astronomical imaging, we cannot avoid mentioning the wavelet transform (WT). This is the common multiscale technique used in the multiscale vision model (MVM) (Bijaoui & Rué [9]) that we will look at later. The most used transform is the stationary wavelet transform (SWT), more commonly known as the "à trous" algorithm (the French translation of holey meaning that zeros are inserted in the filters), an extension of the discrete wavelet transform designed to overcome the lack of shift-invariance. Since astronomical sources are mostly isotropic, stars, for example, or quasi-isotropic, such as with galaxies or clusters, the SWT does not favour any direction in the image and maintains the sampling at each scale. The SWT of a signal produces several scales, as can be seen in Figure 2.1.

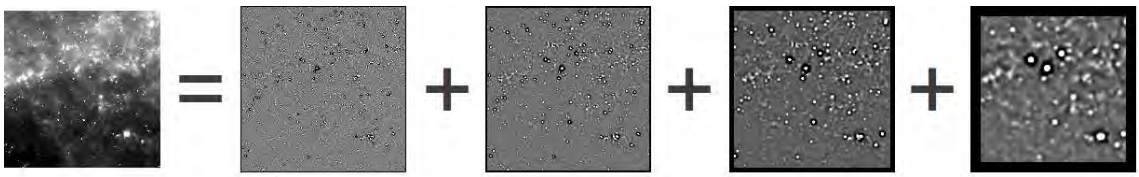

Figure 2.1: Wavelet decomposition of an image in several scales. From left to right four scales from high to lower frequencies

There are many extensions of the WT that are more suitable depending on the detection goal. For example, Damiani et al. [17] proposed a method based on the Mexican hat wavelet transform (MHWT), a special case of the family of continuous wavelets obtained by applying the Laplacian operator to a 2D Gaussian (for more information see [47, 15, 21] and references therein), to detect sources in X-ray images. Moreover, this kind of WT has been used by other authors, such as Vielva et al. [104], who used the spherical Mexican hat wavelet transform, an MHWT extension for spherical functions, to detect point sources in all-sky radio frequency maps. More recently, Starck et al. [90] proposed a source detection approach based on the multiscale variance stabilisation transform (MSVST), based on the differences between two consecutive WT scales, applied to gamma-ray images. Kaiser et al. [47] pioneered the use of WT for astronomical object detection. Specifically, they used the MHWT in multiband images to highlight faint objects.

As the image transformation and detection in multiscale approaches are closely linked, and sometimes one step overlaps the other, more information about these methods is available in Section 2.2.3.

Multiscale decomposition for anisotropic data

While wavelets give a good performance with isotropic features, they are far from optimal with anisotropic objects. Because of this, the astronomical community has had to find alternatives. Some multiscale methods that represent the anisotropic features well have been demonstrated.

To overcome the weakness of wavelets in anisotropic data, Candès & Donoho [13, 14] proposed two new methods of multiscale representation: curvelet and ridgelet transforms, which are very different from wavelet-like systems. Curvelets and ridgelets take the form of basic elements that exhibit high directional sensitivity and are highly anisotropic. For instance, in two dimensions, curvelets are localized along curves, in three dimensions,

along sheets, etc. The ridgelet transform can effectively deal with line-like phenomena in two dimensions, plane-like phenomena in three dimensions, and so on. More details on these two techniques are provided in [91].

In practice, the continuous ridgelet transform (CRT) is used. The idea is to apply the Radon transform (see [13] and references therein) and perform a wavelet analysis in the Radon domain. Thus, the image is represented as functions with simple elements that are in some way related to ridge functions. CRT is therefore optimal to detect lines and segments in images.

Curvelets are also an extension of the wavelet concept. The idea of the curvelet transform is to first decompose the image at different scales, and then analyze each scale by means of a local ridgelet transform. They have a strong directional character in those elements that are highly anisotropic at fine scales. Hence, for specific astronomical data containing edges as with planet surfaces, for example, curvelets are the best choice because they provide a mathematical representation that is ideally adapted to represent objects with curved shapes.

As sometimes both isotropic and anisotropic data are present in images, combined approaches may be the best solution. Hence, a perfect multiscale decomposition should benefit from both the wavelet advantages and the ridgelet or curvelet transforms and maybe others as well. In common practice, these combined approaches are used instead of curvelets or ridgelets alone. For instance, Starck et al. [86, 89] proposed, on the one hand, combinations of wavelets and ridgelets and, on the other hand, combinations of wavelets and curvelets to detect objects in infrared data. In another work, Belbachir & Goebel [5] suggested the combined use of WT and contourlet (see the [5] paper and references therein) for faint source detection also in infrared images. Contourlet is a filter bank transform that can deal with smooth images with smooth contours, so it is similar to the curvelet transform.

2.2 Detection criteria

Image transformation techniques provide a new image or map ready to be processed. At this point, a detection method is ready to be applied to the images. The goal of detection is to locate the astronomical objects and separate them from the background (the sky). Two detection strategies stand out among the rest: thresholding and the local peak search. Thresholding considers that connected pixel regions above a certain threshold belong to

an object, whereas the local peak search finds those pixels that are maximums in a pixel neighbourhood and, from this point, tries to find all the object pixels. Even though these two methods are the most common, we also analyze other strategies that try to solve the detection problem in different ways, most of which are relatively recent. More information is available in Table 2.2, which shows the various works analyzed according to the detection method, the type of image and the specified detection aim. The methods are grouped by the way they perform the detection. Notice that the different strategy aims may not be exclusive, but are simply the way authors referred to them.

2.2.1 Thresholding

In computer vision, thresholding is a simple method for image segmentation. Using this method, a greyscale image is converted into a binary one where the pixels have only two possible values: 0 or 1. These two values are assigned to pixels whose intensities are below (0) or above (1) a specified threshold. In astronomical images as well as in many other fields, thresholding is used to decide which regions (connected pixels) are considered as objects and which are considered as background. In a more formal way, the binarized image I_{th} is the result of applying the following function to all the pixels in an original image I:

$$I_{th}(i,j) = \begin{cases} 1 & \text{if } I(i,j) > th \\ 0 & \text{otherwise,} \end{cases} \tag{2.3}$$

where $I_{th}(i,j)$ and $I(i,j)$ are the intensity of the pixels in row i and column j of the binarized and original images, respectively, and th is the established threshold.

Defining an appropriate threshold is not easy due to several factors like noise, background variations, or the diffused edges of the objects. Any chosen threshold may result in some true objects being overlooked (false negatives) and some spurious objects being considered as real (false positives). Varying the threshold to the extremes minimizes one of these types of errors but maximizes the other. Hence, the best results rely on setting the threshold to make the two errors as small as possible.

In the papers reviewed, the authors have set the threshold following various strategies. For example, Irwin [44], Freeman et al. [21] and Hadjiyska et al. [31] set it depending on the sky estimation computed, while Starck et al. [87, 90] and Lang et al. [50] set it depending on the noise as a multiple of the noise estimation. Whiting [109] used a multiple of the estimated SNR. Szalay et al. [93] modelled the sky as a χ^2 distribution, and got

Table 2.2: Summary of the methods' detection criterion. Detection aims stand for: extended source detection (ESD), faint source detection (FSD), point source detection (PSD), and source detection (SD). The term 'n/a' stands for not available.

Article	Strategy	Image type	Aim
	Thresholding		
Jarvis & Tyson (1981) [46]	Local	Optical	FSD
Irwin (1985) [44]	Global	Optical	SD
Le Fèvre et al. (1986) [53]	Local	Multiband	SD
Slezak et al. (1988) [84]	Global	Optical	SD
Bijaoui & Rué (1995) [9]	Global	Optical	SD
Bertin & Arnouts (1996) [6]	Global	n/a	SD
Szalay et al. (1999) [93]	Global	Multiband	FSD
Starck et al. (1999) [87]	Global	Mid-infrared	FSD
Lazzati et al. (1999) [52]	Global	X-ray	SD
Hopkins et al. (2002) [42]	Global	X-ray	SD
Freeman et al. (2002) [21]	Global	X-ray	SD
Makovoz & Marleau (2006) [57]	Global	Multiband	PSD
Melin et al. (2006) [62]	Local	Radio and multiband	PSD
Yang et al. (2008) [113]	Local	Optical	SD
Herranz et al. (2009) [36]	Global	Radio	PSD
Starck et al. (2009) [90]	Global	Gamma-ray	SD
Haupt et al. (2009) [35]	Global	Radio	SD
Lang et al. (2010) [50]	Global	Multiband	PSD
Trott et al. (2011) [96]	Global	Radio	PSD
Lanz et al. (2012) [51]	Global	Radio	PSD
Whiting (2012) [109]	Global	Radio	SD
Hadjiyska et al. (2013) [31]	Global	Optical	SD
	Local peak search		
Herzog & Illingworth (1977) [37]	Detection threshold	Optical	SD
Newell & O'Neil (1977) [70]	Detection threshold	Optical	SD
Kron (1980) [49]	Profile fitting	Multiband	FSD
Buonanno et al. (1983) [12]	Detection threshold	Multiband	SD
Stetson (1987) [92]	Profile fitting	n/a	SD
Vikhlinin et al. (1995) [105]	Detection threshold	X-ray	SD
Kaiser et al. (1995) [47]	n/a	Multiband	SD
Damiani et al. (1997) [17]	Detection threshold	X-ray	SD
Mighell (1999) [64]	Profile fitting	n/a	SD
Vielva et al. (2003) [104]	n/a	Radio	PSD
Hobson & McLachlan (2003) [38]	Profile fitting	n/a	SD
López-Caniego et al. (2006) [55]	Profile fitting	n/a	PSD
González-Nuevo et al. (2006) [26]	n/a	Radio	PSD
Savage & Oliver (2007) [81]	Profile fitting	Infrared	SD
Feroz & Hobson (2008) [20]	Profile fitting	n/a	SD
Carvalho et al. (2009) [15]	Profile fitting	Optical	SD
Broos et al. (2010) [11]	n/a	X-ray	SD
	Other methods		
Andreon et al. (2000) [2]	Neural networks	Multiband	SD
Liu, Chiu & Xu (2003) [54]	Neural networks	Multiband	SD
Aptoula et al. (2006) [3]	Watershed transform	Multiband	SD
Perret, Lefèvre & Collet (2010) [77]	Connected Component trees	Multiband	SD
Molinari et al. (2011) [65]	Lagrangian differentiation	Infrared	PSD
Friedlander et al (2012) [22]	Latent Dirichlet Allocation	Radio	SD
Hollitt and Johnston-Hollitt (2012) [40]	Circular Hough Transform	Radio	ESD
Hancock et al. (2012) [33]	Mean curvature maps	Radio	SD
Göring et al. (2013) [27]	Minkowski functionals	γ-ray	ESD

the threshold value from the intersection point between the theoretical distribution and the real data distribution. In a different way, Slezak et al. [84] and Herranz et al. [36] determined the threshold by the distribution of the peaks previously found. They set the threshold at 3.8 and 5 times the deviation of the peak distribution, respectively. Hopkins et al. [42], Trott et al. [96], and Hancock et al. [33], moreover, used the false discovery rate (FDR) method to select a threshold that controls the fraction of false detections (see the Hopkins paper for more information). Haupt et al. [35] also used a threshold obtained through FDR after ruling out regions without sources with their Distilled Sensing method. In a similar way, Lazzati et al. [52] obtained the threshold as a function of the number of pixels, the background estimation, and the maximum number of spurious sources expected.

However, not all these methods are fully automated. Source extraction packages such as SExtractor [6] and Mopex [57] use user-specified thresholds. For example, SExtractor gives the possibility of setting the threshold to an absolute value or as a multiple of the background level. In these tools, when a source is considered too large, it may be assumed that it is a cluster of sources, and the threshold is raised to detect the sources independently.

Mainly due to background variations, a common practice in astronomical image detection is local or adaptive thresholding: a different threshold is used for different regions in the image. This can typically be computed using a sliding window. For example, Jarvis & Tyson [46] adapted the threshold as the window progressed. Starting with a specific threshold, if the pixels in the window were lower than the threshold, and so considered as sky, the threshold value was updated with the sky value of these pixels. Another way to fix the threshold locally was the way Le Fèvre et al. [53] did it. They computed the histogram of pixel intensities at each window, and set the threshold at 1.5 times the deviation distribution. Melin et al. [62] and Lanz et al. [51] used a multiple value of the SNR, whereas Yang et al. [113] used a method to automate the threshold calculation called the Otsu method [73], where the intra-class variance is minimized to get a good threshold.

2.2.2 Local peak search

The main principle of the local peak or maxima search method consists of searching for pixels that are considered peaks or, in other words, that are a local maximum in a neighbourhood. In most cases, to avoid the unnecessary analysis of all the pixels, only those peaks above a given threshold are considered. When this detection method is used, it is often accompanied by an image transformation step that enhances the peaks to be

found, and another step computed after the peak search that establishes or corrects the pixels around the peak that belong to the object. Many times, this last step is a fitting process, which is possible because the nature of the object is well known. So the local peak search as such provides a list of candidates that can be the central points of an object. For this reason, this method is typically used as a previous step to photometry calculation. The local peak search is more appropriate to detect stars and other point sources, and is not well suited to detecting complex objects like galaxies and other extended sources. A formal representation of this method is as follows:

$$I_{lps}(i,j) = \begin{cases} 1 & I(i,j) \geq I(k,l) \\ 0 & \text{otherwise,} \end{cases} \tag{2.4}$$

where $I(i,j)$ is the intensity of the pixels in row i and column j, and $I(k,l)$ is the intensity of a neighbour pixel of $I(i,j)$. For example, considering the 8-connectivity described below, k takes values from i-1 to i+1, and l takes values from j-1 to j+1.

This method was already being used in the late seventies by Herzog & Illingworth [37] and Newell & O'Neil [70]. They defined a peak as a pixel with an intensity greater than or equal to their eight adjacent pixels (8-connectivity) and above a threshold based on the sky level computed. Therefore, the objects were the connected regions centred on a peak. They computed some tests to deblend objects (connected regions with more than one peak), such as the data-over-gradient test (see [37, 70] and references therein for more information on this test). Moreover, Buonanno et al. [12] searched for peaks over the sky level in windows of N×N, and all the pixels connected to the peaks above a certain threshold were added to make the corresponding objects. Vikhlinin et al. [105], in X-ray images, considered a pixel as maximum if it was greater than its 25 neighbours and above a threshold based on the background.

In several approaches, once the peaks were found, a known distribution was fit around them. In this sense, Kron [49] opened windows of 50×50 around the maximums found, computed the histograms, and selected the distribution (between two different light distributions that model faint and bright sources) that best fit the histograms. In a similar way, Savage & Oliver [81] opened a window for each peak in infrared images and selected the distribution from among sky, point-shaped source or an extended source that best fit. López-Caniego [55] searched for local maximums and distinguished those caused by the presence of sources. This distinction was achieved by a constrained optimisation problem that considered peak densities leading to an optimal distribution that fits the source in

amplitude and curvature. Other works used sharpness and roundness statistics and PSF fitting (Stetson [92] in his Daophot software), or analyzed the annulus surrounding the peaks to determine what was background and what was source (Mighell [64]).

2.2.3 Multiscale vision model

The multiscale transform from the "à trous" algorithm, decomposes an image $I(i,j)$ in N scales or wavelet planes $W_n(i,j)$. Thus, a detection method can be independently applied to each of these images representing a scale. Each scale has the same number of pixels as the image. As we have already mentioned, the original image can be expressed as the sum of all the wavelet scales and the smoothed array F_N:

$$I(i,j) = F_N(i,j) + \sum_{n=1}^{N} W_n(i,j). \tag{2.5}$$

A further step is to consider a multiscale object representation that associates an object contained in the data with a volume in the multiscale transform. This representation requires the application of a segmentation method scale by scale. A general idea for object definition lies in the connectivity property. An object is located in a physical region, and the pixels of this region are connected to other significant adjacent pixels. This connectivity is present both in the same scale and in contiguous scales. This is exactly what the multiscale vision model (MVM) [9] does.

The following, are the MVM steps:

1. The WT with the "à trous" algorithm is applied to an image.

2. A scale-by-scale thresholding procedure is performed, obtaining the object segmentation at each scale.

3. In order to define the object's structure, an inter-scale connectivity graph is established.

4. An object identification procedure extracts each connected sub-graph and considers them as objects.

5. Finally, from each set of pixels, an image of the object can be reconstructed using some reconstruction algorithms.

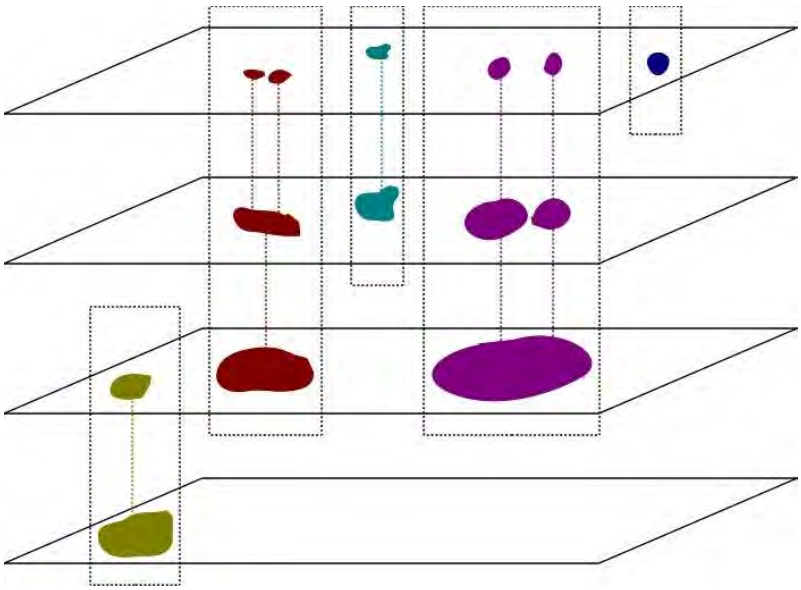

Figure 2.2: Example of the connectivity in the wavelet scales. Adjacent significant coefficients in a scale and between contiguous scales are considered part of the same object.

So, at each scale, the so-called significant wavelet coefficients, values in a wavelet scale above a given detection limit usually dependent on the noise model, are searched out. At each scale, we have a boolean image with a pixel intensity equal to 1 when a significant coefficient has been detected, and 0 otherwise. Afterwards, the segmentation is applied by labelling the boolean values with each group of connected significant coefficients getting a different label. An inter-scale relation between two labelled zones in two adjacent scales exists if the maximum significant coefficient of the first one lies in the region of the second in the next scale. Therefore, an object is defined as a set of inter-scale relations having a graph structure. A representation of this inter-scale connectivity graph is shown in Figure 2.2.

This pipeline and similar ones based on WT have been used as reference work in many subsequent multiscale approaches. For example, after applying a Gaussian fitting and a median filter, Damiani et al. [17] applied the MHWT to an image and local peaks over a significant threshold were considered as sources if their amplitude was significant with respect to the expected fluctuations of the local background. Very similar to this approach is the one by Freeman et al. [21]. It differs in the background estimation, since they carried this step out at each wavelet scale with an average filter and weighting the resulting values with the negative wings of the MHWT. In addition, they proposed a postprocessing step that analyzed some properties of the sources detected and rejected

those that were considered spurious.

Like Bijaoui and Rué, Starck et al. [87] used the MVM to decompose the signal into its main components. Moreover, Broos et al. [11] recently developed a wavelet-based strategy to find sources in X-ray images from the Chandra telescope. The image was deconvolved using the WT and reconstructed again to smooth the PSF effects using a reconstruction algorithm called Richardson-Lucy [80, 56] explained in detail in [11]. A candidate list of sources was created by locating peaks in the reconstructed image, and if those peaks fulfilled a number of properties, they were considered as sources; otherwise they were rejected.

Nevertheless, the whole MVM process is not required. Executing the detection process at only a few scales instead of in all may often be enough. In the work of Kaiser et al. [47], the source positions and sizes were simply identified by locating peaks at their scales of maximum significance. Vielva et al. [104] deconvolved all-sky surveys with the MHWT and proposed dividing the image into different regions, estimating the optimal scale in each region. González-Nuevo et al. [26] also decided to apply some extensions of the MHWT to radio maps. They proposed using the Mexican hat wavelet family (MHWF), with a range of MHWT obtained by applying another Laplacian operator to the MHWT, and repeating this process iteratively to detect point sources by selecting the optimal scales of different MHWT in the family. They tested the first four members of the family and finally applied a local peak detection. In a similar way, Starck et al. [90] used the MSVST and a thresholding was computed at those scales with significant wavelet coefficients to finally reconstruct the image. Lazzati et al. [52] used only a few predefined scales where a thresholding was applied, and afterwards, the detection at different scales was correlated to remove multiple detections of the same source and to determine which nearby sources were extended ones.

Men'shchikov et al. [63] decided to use a model made up of the different multiscale planes, obtained through successive unsharp masking, of different wavelength bands. Afterwards, the background, estimated through σ-clipping, is subtracted from each scale and the normalized resulting scales are added up, allowing the detection of sources in multiple wavelengths in an aggregate way.

2.2.4 Other detection criteria

Although most of the classical approaches are based on thresholding and a local peak search, other strategies have been used to detect astronomical objects. In many cases these

approaches have been developed over the last few years and focus more on techniques from computer vision and machine learning fields.

For example, Andreon et al. [2] turned the object detection problem into a classification one. They classified the pixels as if they belonged to the class object or to the class background. This task was achieved by using a kind of neural network, so they named this package NExt, from NEural Extractor. Specifically, they used principal component analysis neural networks (PCA-NN) to reduce the dimensionality of the input data by eigenanalysis and basically selecting the principal vectors. They trained a PCA-NN with patches of the representative zones in the image, and a vector with fewer features than the returned input. Afterwards, this output became the input of an unsupervised neural network responsible for classifying the pixels from the object and the background. Based on this detection approach, Liu et al. [54] proposed changing the PCA-NN used by Andreon et al. [2] to a local principal component analysis, a kind of PCA that clusters the input data and finds the principal vectors for each cluster. They used a local PCA to automatically extract features from the image. A clustering process was then computed, and the pixels were classified from these clusters.

Aptoula et al. [3], after the application of morphological operations, segmented the image with the watershed transform. Notice that in this case, the images contained only one object to segment, mainly galaxies. This unsupervised segmentation acts as a drop of water falling on a topographic relief corresponding to the image; every grey level may be considered as a height in the relief. By placing a water source in each regional minimum, the relief is flooded from the sources, and barriers are built when different sources are about to merge. To avoid over-segmentation, they only considered a few marked minimums as water sources. Specifically, two markers were used: one in the centre of the object and another in a minimum external region. These two markers were found by thresholding and morphological techniques. Hence, a good segmentation between object and background was computed.

In a different way, Perret et al. [77] recently used connected component trees (CC-trees) to detect sources in multiband images. CC-trees have become popular models for the analysis of greyscale images (the authors used an extension for multiband images), since they provide a hierarchical representation of images that can be used for segmentation and object detection, among others. The representation of a greyscale image is based on the thresholding between its minimum and maximum grey levels, thresholding the image at different levels starting from the minimum value and increasing it until the

maximum value is reached. There is a relationship of the inclusion between components at sequential grey levels in the image. The root is the whole image and, at every level of the tree, the various foreground regions are decomposed in some regions obtained with a higher threshold. Perret et al. equipped the nodes with some attributes like multispectral information of the thresholded region, and then pruned the ones considered irrelevant to finally reconstruct the image. Therefore, the remaining nodes at significant levels were considered as sources.

Molinari et al. [65] analyzed multidirectional second derivatives to build curvature models of the image. They aimed at detecting point and compact sources characterized by fairly spherical shapes. Specifically, he applied the Lagrangian differentiation (derivatives) in four directions: the horizontal and vertical axis and the two diagonals. This way they obtained four images with curvature values in these four directions. Those groups of connected pixels that exceeded a specified level in all the curvature images were considered as sources. In a similar way, Hancock et al. [33] used a discrete 2D Laplacian kernel to calculate the curvature along four directions, but they combined the four orientations to calculate the mean curvature map to identify blended sources.

Friedlander et al. [22] proposed the segmentation of sources in radio images by means of Latent Dirichlet Allocation. This strategy is based on the idea of a bag of words that considers an image as a collection of visual words. Given a vocabulary of words, the frequency distribution of these words in an image is known as a topic, and therefore, an image is a collection of topics as well. The authors considered that the image vocabulary was constructed by building the histogram of pixels of the whole image, where each bin corresponds to a word. Afterwards, the image was divided into subimages and histograms were built for each. Through Gibbs [22], a sampling of the most latent topics, subsets of some frequent words in subimages, are located. For instance, two topics that must commonly occur in images are those that include background and source pixels, and in this way, sources can be located.

Hollitt and Johnston-Hollitt [40] used the Circle Hough transform to detect circular extended sources. The Hough transform is used to find and characterize an object with a particular shape in images. It is based on the principle that convolving a circle profile with the image, the pixels most likely to be part of a circle are highlighted. If multiple profiles with circles with radii of different sizes are used as if it were a 3D representation of a cone, then circular regions of the images with different sizes are unveiled.

Recently, Göring et al. [27] proposed an approach to detect extended sources through

morphometric analysis. They used Minkowski functionals, which are 2D geometric quantities that can be extracted from the regions found in binarized images: the area, the perimeter and the Euler characteristic (number of components minus the number of holes). These features were locally extracted from the image and compared to the features extracted from a region of the sky with only background. If they differed considerably, it was more likely to be dealing with a source.

2.3 Results

Since many papers do not focus exclusively on astronomical object detection, such as those that only make catalogues of new sources found or focus more on computing the photometry of the sources found, in this section we present only the results of those papers that have source detection as their main objective. We describe the measures computed in these works and evaluate their performance, and compare and discuss the results presented, pointing out the most interesting aspects. Finally, we highlight the techniques that are more appropriate for each type of astronomical image.

2.3.1 Evaluation measures

In the various papers, results have been evaluated in several ways. Nevertheless, most are measured to know which of the objects detected are truly objects. This validation is usually done using published catalogues or data obtained from an astronomical package used as reference (e.g. SExtractor and SAD). In some cases, the validation of real objects is done with the assistance of an astronomical expert who considers the detections as either true or spurious. Moreover, simulated images are widely used since the simulated sources are placed in known positions, and therefore, it is easy to evaluate the goodness of the results by checking the detected sources that match the previously simulated ones.

Whether using a reference catalogue or simulated data as ground truth, the performance of the detection and segmentation methods is evaluated by computing true positives (TP), false positives (FP), false negatives (FN), and true negatives (TN). TP are detections that are true sources, FP are detections that are not true sources so they are spurious detections, FN are true sources that have not been detected because they were missed by the method, and therefore, considered as background, and TN are background zones correctly considered as such. Figure 2.3 shows a simple example of these different measures. Obviously, the objective is to obtain the maximum number of TP and TN, and at the same

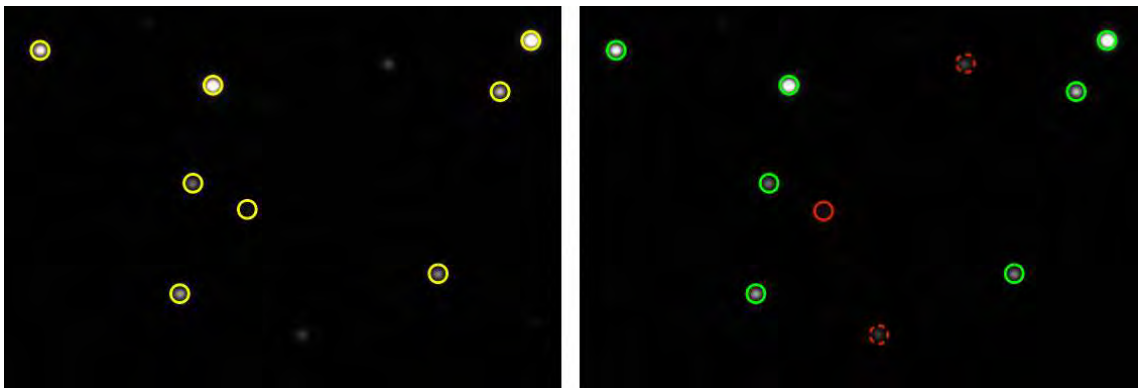

Figure 2.3: Simple graphical example to explain TP, FP, FN, and TN measures. On the left, some detections provided by a detection method. On the right, the evaluation measures: in green, TP; in solid red line, FP, and in dotted red line, the FN. Background regions considered as such are TN.

time, the minimum number of FP and FN. However, in practice, increasing the number of TP usually increases the number of FP, while reducing the number of FN also reduces the number of TN. Therefore, an effort must be made to set the parameters of the detection method to maximize TP and TN and to minimize FP and FN.

Reference catalogues may also be used to compare the performance of the methods directly. As the catalogues used as references tend to be published in international journals, they have a reliable list of sources and can therefore be used to extract some measures between the reference sources and the detected ones. The two catalogues can then be compared based on the sources that coincide in both or the sources that appear in only one. If in addition more reference catalogues are available, cross comparisons may be performed and the goodness of the method can be estimated by computing the number of missed sources, meaning those not part of one catalogue but appear in the rest).

2.3.2 Analysis of the results

We provide a qualitative comparison of the results obtained from the approaches analyzed. Table 2.3 summarizes the results presented in the articles analyzed. We show the source catalogues or the source detection packages used as reference (second column), the type images used and if they have real or simulated (sim) origin (third column), the number of detected objects (forth column), the measures used to evaluate the results (fifth column), and the performance (last column). Notice that the forth and sixth columns may have

more than one value according to the different experiments performed. A qualitative evaluation of these approaches is difficult to carry out because the work was done on different types of images and with different purposes.

Several works used TP and FP rates to evaluate the performance of their approaches. For instance, Slezak et al. [84] first estimated by eye the different sources present in a wide field from Schmidt plates, and applied the detection method with different detection thresholds expressed in terms of magnitude afterwards. As the magnitude threshold was decreased, the number of sources detected decreased, but the percentage of well-detected sources increased. The best results were obtained with a low threshold: from the 363 sources detected, 353 were TP and 10 FP. Starck et al. [87] developed an approach for ISOCAM, one of the four instruments on board the ISO (Infrared Space Observatory), mosaics that applied to a simulation of the ISOCAM-Hubble Deep Field North, detecting 45 sources from the 46 generated; in other words, TP = 45 and FN = 1. Andreon et al. [2] tested several types of neural networks on a field from the Canadian Astronomy Data Centre. This field has been widely studied, so as a reference they took a specific catalogue that contained 4819 objects with ∼2400 too faint to be visible. The best tests found 2742 and 3776 sources in the field, among which 2059 and 2310 were TP and 683 and 1466 were FP, respectively. Moreover, they applied the detection tool from the SExtractor package to the same field, obtaining a catalogue with 4254 sources, with 2388 TP and 1866 FP. Although SExtractor detected more sources, a number of sources similar to those found by the reference catalogue, the absolute number of TP computed by Andreon et al. was slightly lower than SExtractor's TP, and, in the FP case, they were substantially lower.

Guglielmetti et al. [30], performed experiments using simulated images with 100 sources and repeated them adding different levels of noise: 0.1%, 1% and 10% of the counts, respectively. The results obtained were 64, 41, and 25 TP, and 8, 9, and 0 FP respectively, showing that by increasing the level of noise, the number of detections became lower, although all the detections were TP, which illustrates the importance of defining whether the priority of the detection strategy is to find the maximum number of true sources regardless of the number of spurious detections, or to guarantee that most of the detections are true regardless of missing true sources. Therefore, in terms of TP, Guglielmetti et al. obtained better results than Wavdetect, but not with FP. Carvalho et al. [15] also used three simulated images, the first two with 16 objects and the last with 8. Their method was able to detect 67.41%, 56.41%, and 82.95% of the simulated sources (TP), and obtained 9.6%, 8.62%, and 8.19% of spurious detections (FP). They also estimated the performance of their method by an error computed by adding the number of FP and

Table 2.3: Summary of the results presented in the articles analyzed. Slashes (/) separate different experiments with different parameter settings or different test images, while values in parentheses refer to reference catalogues, in the same order as the second column. Value "n/a" means "not available".

Article	Reference	Image type	Detections	Measures	Performance
Slezak et al. (1988) [84]	Manually	Optical (real)	363	TP	353
				FP	10
Damiani et al. (1997) [17]	MPE and WGA catalogues	X-ray (real)	453	Missed	10 (75,47)
Starck et al. (1999) [87]	Simulated sources	Mid-infrared (sim)	46	TP	45
				FP	1
Andreon et al. (2000) [2]	SExtractor	Multiband (real)	2742/3776	TP	2059/2310 (2388)
				FP	683/1466 (1866)
Freeman et al. (2002) [21]	MPE and WGA catalogues	X-ray (real)	148	Coincidences	81 (12,27)
Perret et al. (2008) [76]	Manually	Multiband (real)	17	Recall (%)	82/87
Guglielmetti et al. (2009) [30]	Simulated sources	X-ray (sim)	100	TP	64/41/25 (56/37/23)
	Wavdetect			FP	8/9/0 (4/1/1)
Carvalho et al. (2009) [15]	Simulated sources	Optical (sim)	n/a	TP (%)	67.41/56.41/82.95
				FP (%)	9.6/8.62/8.19
Broos et al. (2010) [11]	Reference catalogue	X-ray (real)	100	TP	89
				FP	11
Molinari et al. (2011) [65]	Simulated sources	Far-infrared (sim)	1690	TP (%)	84.5
				FP (%)	15.5
Friedlander et al. (2012) [22]	Manually	Radio (real)	n/a	Precision	0.83/0.98/1.0/1.0
	Duchamp			Recall	0.93/0.99/0.99/0.89
Hancock et al. (2012) [33]	Simulated sources	Radio (sim)	n/a	Completeness (%)	93.87/99.91/99.87
	SAD, Selavy, SExtractor and Sfind			Reliability (%)	98.69/100.00/100.00

FN (42.19%, 52.2%, and 25.15%, respectively). Molinari et al. [65] used far-infrared and submillietre simulations with 2000 injected sources and achieved 1690 TP, i.e., 84.5% TP and 15.5% FP.

Other works have used different ways to estimate their results. For instance, Damiani et al. [17], in order to compare the performance of their method on 7 images from the ROSAT satellite, used two catalogues called MPE with 286 sources in total and WGA, 389 sources in total, as reference, and counted the number of sources detected by two catalogues and missed by the other one. Their method detected 453 sources; 244 coincidences with MPE, 272 coincidences with WGA, and 197 sources present in all three catalogues. They found that their method missed 10 sources, less than MPE and WGA, which missed 75 and 47 sources respectively. Freeman et al. [21] also used crossed comparisons between the sources found with their method in a ROSAT image and the ones found by MPE, 100 sources found, and WGA, 127 sources found. They found 148 sources, of which 81 appear in all three catalogues. The coincidences between their work and MPE were 97, while the coincidences with WGA were 108 and the coincidences between MPE and WGA were 84. Broos et al. [11] tested their local peak method in combination with Wavdetect to find 100 sources; 50 with Wavdetect and 50 with their source detection method, on a map from the Chandra X-ray Observatory. They compared these sources with a reference catalogue and found 89 coincidences.

Perret et al. [76] had a reference catalogue with nine galaxies detected. To validate the good performance of their galaxy-finding method, they first tested their method on two images, and found 17 objects; 6 galaxies from the reference catalogue and 8 new sources that an expert also considered to be galaxies. It means a recall, percentage of true detected galaxies, of 82%. When testing the method on 16 images, they found a recall of 87%. Friedlander et al. [22] also used the recall measure to quantify their method's performance in radio images from the Australia Telescope Compact Array (ATCA). They obtained values of 0.93, 0.99, 0.99 and 0.89 in different regions of the survey, similar than the reference method Duchamp. They also obtained precision results of 0.83, 0.98, 1.0 and 1.0 in the same regions. In a similar way, Hancock et al. (2012) evaluated their method's performance in terms of completeness (recall), fraction of sources in the catalogue correctly identified, and reliability (precision), fraction of the detections corresponding to true positives. They performed different experiments in radio interferometric simulations by changing the detection threshold and obtained completeness percentages of 93.87%, 99.91% and 99.87% and reliability percentages of 98.69%, 100.00% and 100.00%. These results are on a par with those of other detections packages such as SAD, Selavy, SExtractor

and Sfind.

In some works, the performance depends on the parameter setting selected. For instance, Vielva et al. [104] and González-Nuevo et al. [26] repeated several experiments with different thresholds until they got a rate of spurious sources lower than the 5% of the total number of sources detected. Moreover, these two approaches worked with images with several frequency channels, and therefore, a different threshold was needed at each channel. Vielva et al. used all-sky maps with 10 channels, and, for example, in the three lower channels, they obtained 27257, 5201, and 4195 sources, respectively. González-Nuevo et al. also performed this strategy in an image with 3 frequency channels, and for each channel they applied the first four transforms of the MHWF. For example, for the channel with the lowest frequency, the sources detected were 543, 639, 583 and 418, respectively.

2.4 Discussion

As we have seen, several strategies are used to deal with the astronomical source detection problem. Most of them coincide in focusing the detection criteria on the intensity of the image pixels, whether in the image transformation steps in order to enhance the sources with respect to the background, or in the detection process, choosing those pixels with an intensity value suggesting they are likely to be part of an object. We have seen that all the different image transformation and detection steps are used indistinctly in all types (all frequency bands) of astronomical images, although there are techniques that are more commonly used in some particular bands. An overview of the different techniques reviewed with their strengths and weaknesses is presented in Table 2.4.

Regarding astronomical images, two main drawbacks caused by the acquisition process hinder detection: the variable background and noise. Hence, image transformation steps have taken a fundamental role in astronomical image processing. Therefore, some image transformation steps must be applied depending on whether the images have background variations, noise or both. Background inhomogeneity can be corrected by applying a smoothing with filters or by removing the background. In many cases, background subtraction is preferable to filtering because it is already detecting sources implicitly by discarding those regions that are most probably not sources. Furthermore, although filtering decreases the impact of background variations and noise, it may blur the sources. In the case of noise, filtering seems to be the most widely used technique [64, 57, 113, 76].

Multiscale approaches are also gaining in popularity because they allow the background

Table 2.4: Overview of the different techniques reviewed with their advantages and drawbacks.

Step	Description	Strengths	Weaknesses
Image transformation			
Basic image transformations	Basic transformation steps such as filtering, profile fitting or morphological operators	Intuitive, fast and easy Slightly emphasize sources Correct background variations Filter noise	Limited May blur and twinkle the image Often need more transformation steps
Bayesian approaches	Methodologies based on Bayesian inference	Emphasize sources Good results with source variability Reduce background variability and filter noise	Computational cost Need prior knowledge
Matched filtering	Methods based on filters with the profile of the objects to find	Rather emphasize sources Reduce background variability and filter noise	Need prior knowledge Different filters required for different sources
Multiscale approaches	Approaches that decompose the image in several scales	Filter noise and delete background (same time) Good results with source variability Allow working with different scales Implicitly performs source detection Can deblend sources	Quite slow Often need combinations of transforms
Detection criterion			
Thresholding	Pixels above a certain threshold are considered as part of the object	Good results with all sources Good results with inhomogeneous background Good results with significant contrast and high SNR	Difficult to select the optimal threshold Not suitable for faint sources
Local peak search	Search pixels that are maximums in a neighbourhood	Good results with point sources Good results with noisy images	Need an additional detection process Not suitable for extended sources
Other methods	Other innovative detection methods	Similar results than the other two methods	Still not have enough acceptance

to be removed and noise to be filtered at the same time. Further advantages are shown in Table 2.4. Since they extract the signal at different scales, they are suitable when the images have sources with different sizes and complex shapes. Furthermore, being able to work with multiple scales and therefore multiple images, this technique offers the possibility of extracting the best from each one, or selecting the best suited scales to perform the detection. Most multiscale analyses are based on the wavelet transform or its variants [17, 87, 21, 104, 26].

Analyzing more particularly the use of image transformation methods at different frequency bands, we observe that basic image transformation is commonly applied to optical and multiband images, which means that this kind of method has a good performance in the visible band and its close frequencies, although we also find basic techniques combined with other frequency bands, though to a lesser extent. On the contrary, approaches that work with optical and multiband images are not based on a multiscale decomposition. The multiscale strategies are widely applied to radio, infrared and X-ray images. We have also noticed that matched filtering is used especially in the radio band, while Bayesian approaches are equally applied to different bands.

Regarding detection criteria, the vast majority of works reviewed used a thresholding and a local peak search, both of which seem to have similar performances. We have seen that after any kind of image transformation, both methods can be used interchangeably and equally for all types of images. However, the choice may depend on some characteristics as can be seen in Table 2.4. A local peak search is not suitable for detecting extended sources, and is preferable when images are noisy and have point sources since it is a neighbourhood-based algorithm and easily discards noise pixels, thus avoiding confusion with source pixels. When an image has an non-homogeneous background, the best choice is to tackle the detection with local thresholding, whereas global thresholding is preferable when an image has significant contrast between objects and background or a high SNR. The rest of the approaches that do not use either thresholding or local peak searches have in common that are relatively recent, most of which having been developed over the last few years, they are all innovative, and perform object detections on a par with the two typical methods.

Analyzing the results, we noticed that the best performances in terms of TP were obtained by Slezak et al. [84] and Starck et al. [87]. Moreover, Damiani et al. [17] and Freeman et al. [21] also obtained satisfactory results in terms of coincidences with published catalogues. Some other works obtained good results, but we consider that the

selected ones are the most significant because they deal with considerable numbers of sources, in most cases hundreds, and did not use additional resources as astronomical detection packages. We want to stress, on the one hand, that most of the approaches that apply any kind of image transformation used multiscale strategies, specifically the wavelet transform [17, 87, 21]. On the other hand, the detection step used is mostly thresholding [84, 87, 21].

2.5 Conclusions

This chapter has reviewed automated approaches to source detection in astronomical images, classifying them according to the type of image transformation and the detection criterion used. In addition, the results obtained by these approaches have been summarized and compared, and the most frequently used evaluation measures in this field have been reviewed. We observed that the automated detection of objects in astronomical images is a challenging task due to the huge amount of objects in the sky and the limitations of the acquisition devices.

As illustrated in Table 2.4, the different methods reviewed have advantages and disadvantages and using either one or another will depend on the features in the images and the aim. There are several factors to take into account such as noise, dynamic range, interferences, variable background, source shapes, etc. Moreover, we have seen that the different methods have to be properly tuned to provide optimum results.

Chapter 3

Quantitative evaluation of astronomical source detection methods

In the previous chapter, an overview of the reported results of the most commonly used source detection methods was presented. This qualitative evaluation aimed at to highlighting the strengths and weaknesses of these detection strategies and finding out which of them is more appropriate under certain circumstances, such as the image type, the source type to detect, or the noise level. This analysis studied the performance of the methods based on the original results presented in the papers reviewed. Thus, the analysis was performed using different sets of images, evaluation measures and detection aims. The current chapter focuses on an extensive quantitative evaluation of some of the most representative detection strategies, unifying the evaluation framework. We aim to carry out a significant comparison of the results of different well-known detection techniques applied to a common set of images, in order to highlight the best strategies for a defined purpose with data with clearly specified characteristics (optical, infrared, and radio astronomical images). These types of images have been selected in order to focus our analysis on different methods specially designed to work on images with Gaussian noise distributions. Therefore, the performance of these methods may be harmed if images with instrumental artefacts that cannot be described as Gaussian noise are used. Moreover, we focus on the detection of compact sources, including faint sources close to the detection limits and discarding sources that are too extended or too saturated to yield meaningful results with automatic detection tools.

Concerning the different elements involved in this quantitative evaluation, we first selected a set of images from different bands and frequencies from public surveys. These

images include several properties such as noise level, variable background, or source sizes and shapes. Second, we selected the most promising and effective methods in the literature. In this selection, we include some of the most common source extraction software as well as innovative approaches developed by research groups over the last few years. Finally, we have proposed a way of quantitatively evaluating the methods based on reference catalogues used to check the validity of the detections obtained. Statistical analysis allows us to reach conclusions about the methods' performances, pointing out their advantages and drawbacks.

The image sets selected cover only a small portion of the whole wavelength range of existing wide-field images. Moreover, within a particular range of wavelengths, images can have very different characteristics like e.g. noise pattern, depth or point-response function, according to several factors such as the acquisition instruments, the survey strategy or the field of view. Nevertheless, this study should be seen as a general guide exploring the performance of different methods in images of a different nature.

3.1 Methods

In this section, we introduce the methods selected for the quantitative comparison. What led us to choose these methods is the fact that most of them are from relatively recent work, or software that is well known in the community, which means they are very much in focus. On the other hand, the aim is to cover the different techniques of source detection as much as possible. Table 3.1 sums up the type of image transformation and detection criterion used in each approach. Columns one and two show their names and bibliographic reference. Columns three and four show the techniques they use according to the image transformation and detection criterion, whereas column five shows the type of data the methods were initially developed for. Note that some of the approaches do not use any type of image transformation. All the methods specify that they can work on images where the noise is Gaussian. Obviously, there are other source detection methods meant specially for other noise distributions. For instance, Wavdetect (Freeman et al. [21]) and Guglielmetti et al. [30], both used in high-frequency images (basically X-ray bands) were designed to work on images that present a Poisson noise distribution. The first one is based on a wavelet decomposition and a global thresholding, whereas the second uses a Bayesian approach combined with global thresholding. The final selection of methods grouped by image transformation is presented below.

Table 3.1: Methods grouped by image transformation. Super-indices c, f, p, m, and i at the end of the methods' name stand for the programming language in which they are implemented (C, Fortran, Perl, Matlab, and Idl respectively). Asterisks (*) next to the methods' name indicate that it is free software available online. Multiband includes ultraviolet, optical and near-infrared bands.

Name	Reference	Image transformation	Detection criterion	Aim
		Basic		
SExtractor^{c*}	Bertin & Arnouts (1996) [6]	σ-clipping	Global thresholding	Multiband
SAD (AIPS)^{f*}	Greisen (2003) [29]	-	Global thresholding	Radio
Distilled Sensing^{m}	Haupt et al. (2009) [35]	Distilled Sensing	Global thresholding	Multiband
Astrometry.net^{c*}	Lang et al. (2010)[50]	Median filter	Global thresholding	Multiband
Perret$^{N/A}$	Perret et al. (2010) [77]	-	Connected components trees	Multiband
		Matched filtering		
Mopex^{p*}	Makovoz & Marleau (2005) [57]	Median filter + Matched filter	Global thresholding	Infrared
		Bayesian		
SourceMiner^{i}	Savage & Oliver (2007) [81]	Bayesian filter	Local peak search	Infrared
		Multi-scale		
González-Nuevo^{m}	González-Nuevo et al. (2006) [26]	Mexican hat wavelet family	Local peak search	Cosmic microwave background

3.1.1 SExtractor

One of the most commonly used astronomical source detection software is SExtractor (Bertin & Arnouts (1996) [6]). The steps it follows are background estimation, thresholding, deblending to separate two overlapping sources, and detection filtering.

To estimate the background, the image is divided into several subimages the number of which can be specified by the user, the default subimage size being 64×64. Each image histogram is iteratively clipped until a 3σ, known as σ-clipping, around the median is reached. If the mean of the new histogram has significantly changed, the local background estimator is set to 2.5×median − 1.5×mean. Otherwise, it is just set to the mean. A background map is obtained by applying a median filter and interpolating between the subimages. Using this type of background estimation, the faintest sources can be easily detected.

A thresholding step is then performed by fixing the threshold to a specified number of times (1.5 by default) the standard deviation of the raw image above the background map at each pixel. This threshold can also be selected interactively by the user. Additionally, in regions considered too large, a source deblending step can also be performed by means of multiple thresholdings. In other words, a set of connected pixels is thresholded again at different levels (32 by default) between the original threshold and the peak value. A tree structure is built from the new regions found and, if a minimum intensity contrast between branches (0.005 by default) is reached, the object is then deblended.

Finally, the resulting list of sources is filtered to discard possible spurious detections. This is done via the analysis of the mean brightness with regard to the brightness of the detection pixels.

SExtractor is meant to be used with wide field images and works well with crowded populations of sources, being applied to all types of astronomical images.

3.1.2 SAD

AIPS (Astronomical Image Processing System - Greisen 2003 [29]) is a widely used software with many astronomical data analysis features. Among them, a source recognition and fitting procedure called SAD (Search and Destroy). This astronomical software can work with different types of astronomical images, although it was initially intended for radio data.

SAD locates regions of pixels above a certain specified intensity level. For each region,

several initial estimators, such as the strength, size, or number of pixels, are computed. Afterwards, a Gaussian function based on least-squares is fit to each region. Finally, regions that fulfil a set of constraints based on the initial estimators computed or according to specifications set by the user are reported as sources.

3.1.3 Mopex

Another popular astronomical detection package is Mopex from Makovoz & Marleau (2005) [57]. First, a background estimation is performed with a method consisting of a sliding window that computes the pixels' median. Additionally, the median values can be corrected by excluding a user-specified number of too-bright pixels. Thus, biased intensities in pixels close to bright sources are avoided. Using these median values, the background is subtracted.

Second, a matched filter is applied to the image to reduce background variations and to enhance the sources. The pattern used is a patch containing the shape of the expected sources to search for. According to the authors, to achieve a high performance, the pattern should come from the data itself. As a matter of fact, the source profile is not applied to the image directly, but combined with a Bayesian probability which involves prior knowledge: the probability of finding a source pixel and the fact that both point sources and background follow a Gaussian distribution.

Finally, a global thresholding with the threshold selected interactively is carried out. Furthermore, other parameters such as the minimum number of connected pixels required to be a source can be set. Regions that are too large are deblended by raising the threshold iteratively.

Mopex was initially intended to be used for source detection with a variety of infrared images, i.e., data with very high or very low intensity backgrounds or data with very noisy backgrounds. However, it was also satisfactorily validated on other types of images such as optical [57]. Furthermore, apart from detecting sources, Mopex also builds mosaics from a set of input frames.

3.1.4 González-Nuevo method

The González-Nuevo et al. (2006) [26] approach, hereafter referred to as GN, is based on an extension of the wavelet transform (WT) called the Mexican hat wavelet transform (MHWT) obtained by applying a Laplacian operator to the two-dimensional Gaussian

function, and more specifically, a family of MHWT (MHWF), generated by applying consecutive Laplacian operators to the MHWT. Depending on the type of image, the different scales in the MHWF amplify the signal (the sources) to some degree. The optimal scale of the various members of the MHWF is the scale in which the signal-to-noise ratio (SNR) has been increased, and therefore, where the sources are most easily found.

In the optimal scale, a local peak search is applied to all the pixels that exceed a threshold that depends on the standard deviation of the image data (a one-step σ-clipping). Note that in [26], the detection criterion used was different, since they used thresholding instead of a local peak search. However, the authors have recently suggested the use of a local peak search. This method was tested on images with a homogeneous white and Gaussian noise background, specifically cosmic microwave background images, providing satisfactory results [26].

3.1.5 SourceMiner

Savage & Oliver (2007) [81] developed a method based on Bayesian methodology called SourceMiner. For each pixel in the image, their Bayesian filter tries to determine the relative probability of it being either an empty sky pixel or a source pixel.

Hence, they consider two different models: empty sky, described by a single parameter corresponding to the background level; and the point source, a two-dimensional Gaussian model, with a known FWHM, with two parameters corresponding to the background level and the flux of the source. Therefore, the parameters to be estimated are the background level and the flux. In other words, these are the two likelihoods to be calculated. This is achieved through several equations involving the intensity of the pixels in a local region and the values of the modelled Gaussian that lead to a source flux map and a background map.

By means of these likelihoods and using Bayesian evidence, the maximum a posteriori values are computed for each of the two models, which leads to a probability map that indicates where the sources are most likely to be located. Finally, a local peak search is performed for the pixels above a threshold specified by the user. The authors stated that this threshold can be seen as the number of times a pixel is more likely to be source than background.

SourceMiner is meant to be used on infrared images, although the authors stated that it can be used with all types of images with Gaussian noise distributions [81].

3.1.6 DS

Haupt et al. (2009) [35] proposed a signal recovery method with applications in astronomical source detection. The strength of their method, called Distilled Sensing hereafter refered to as DS, lies in the idea of discarding those regions where the signal or sources in astronomy is unlikely to be present, and instead focuses its detection resources on the remaining regions.

DS is an iterative process that refines data by using information from earlier iterations. A certain amount of energy sensing, a predefined value also called budget, is distributed throughout the steps of the iteration. At the same time, this part of the energy is equally distributed over the various regions of interest in the image, all the pixels in the first iteration. A larger value of energy sensing is devoted to the first iterations and is exponentially decreased in later iterations, when there are fewer regions of interest remaining. The data is refined iteratively by allowing some uncertainty, a value drawn from a normal distribution, and dividing by the energy sensing value corresponding to that pixel. This leads to negative values considered noise and are discarded. Afterwards, the regions of interest are limited to regions with positive values, and the process is repeated. Finally, a global thresholding step determines the location of the sources. This approach considers that both the signal and the noise follow a Gaussian distribution, while the signal is sparse compared to the noise level, which is perfectly met in astronomical images.

3.1.7 Astrometry.net

Within the framework of the Astrometry.net project, Lang et al. (2010) [50] developed a method to detect compact objects in various types of astronomical images. First, a median filter is applied to the image to smooth it and reduce the impact of background variations and noise. Afterwards, the noise level is estimated by randomly selecting a few thousand pairs of pixels separated by five rows and columns, and calculating the standard deviation of the differences of intensities for each pair. Next, a thresholding is performed on the filtered image with a threshold set to eight times the deviation previously calculated. The maximum peak of each region is located, and the peaks that do not fulfil certain conditions, considered as probably being noise, are rejected. Finally, a 3×3 window is opened at each remaining peak, and a Gaussian function is fit to it.

3.1.8 Perret method

Perret et al. (2010) [77] proposed a method, hereafter referred to as Perret method, based on connected component trees (CC-trees) to deal with the detection of sources in multiband images. CC-trees are increasingly used in image analysis since they build a hierarchical representation of the level sets, sets of pixels above a given threshold, in an image.

The tree is built by thresholding the image at different thresholds, from the minimum to the maximum pixel intensity. Each region of connected pixels is considered as a node, the root standing for the whole image, and the regions obtained at a certain threshold that are included in another region at the previous threshold generate the children nodes of a father node. Furthermore, each node has attributes with features from its associated region, such as its size. These attributes are used to discern whether the nodes are irrelevant or not by checking which of their values are under a threshold function. The branches with irrelevant nodes are pruned, and finally, the leaf nodes indicate the sources the algorithm has found.

In the context of this quantitative analysis, the method's authors used a different way to establish pixel connection based on hyper-connection, and therefore, hyper-component trees, to improve the robustness to noise. Hyper-connections basically allow to decomposing images into intersecting components, i.e., a pixel may belong to different regions at the same time. For a more detailed description see [78].

3.2 Quantitative evaluation

3.2.1 Test datasets

Using a single dataset allows a significant comparison of the various approaches since they are tested on a level playing field. Moreover, we have chosen different types of images at different bands and wavelengths in order to evaluate how the methods behave with images of a different nature. We are aware that each method was developed with a specific aim, and meant to be used with a particular set of images. However, all the authors have specified that their method was intended either for general use with different types of astronomical images, or to be validated with images with Gaussian noise distributions. It is commonly assumed that lower frequency images, such as radio frequency and submillimetre images, have a Gaussian noise distribution [91]. For this reason, our final dataset consists of optical, infrared, and radio images, as can be seen in Table 3.2. Column one shows

Table 3.2: List of images in the test datasets.

Name	Band	Wavelength	Size (pixels)	Pixel scale (″)	FWHM (″)
$SDSS_u$		u′ (355 nm)			1.75
$SDSS_g$		g′ (469 nm)			1.62
$SDSS_r$	Optical	r′ (617 nm)	2048×1489	0.396	1.41
$SDSS_i$		i′ (748 nm)			1.23
$SDSS_z$		z′ (893 nm)			1.41
$WISE_{3.4}$		3.4 μm			6.08
$WISE_{4.6}$	Infrared	4.6 μm	1000×1000	1.375	6.84
$WISE_{12}$		12 μm			7.36
$CGPS_{21}$	Radio	21 cm	1024×1024	18	60
$CGPS_{74}$		74 cm			204

their assigned name, column two their band, column three their respective wavelengths, column four their size, column five their pixel scale, and column six the FWHM of the point-response function.

Optical dataset

We have selected a set of optical images from the Third Sloan Digital Sky Survey (SDSS-III, [1]). This set consists of five images acquired with the widely used photometric system u′g′r′i′z′ [85], where each of these letters corresponds to a specific filter. Table 3.2 shows the wavelengths of these filters. All the images center on the equatorial coordinate $\alpha = 01^h40^m57.85^s$ and $\delta = +61°16'52.46''$ (J2000.0), have a size of 2048×1489 pixels, and a pixel scale of 0.3887″.

Figure 3.1 (left, with 98% contrast stretching for visualisation purposes) shows the five optical images. These images are very crowded, especially in longer wavelengths. Their background is homogeneous, and has a characteristic pattern of noise most easily seen in the shorter wavelengths, and especially in the $SDSS_u$ image. Furthermore, a diffraction halo is clearly visible around some of the largest sources.

Infrared dataset

Concerning the infrared band, we have chosen images from the Wide-field Infrared Survey Explorer (WISE, [19]) at three different wavelengths: 3.4, 4.6 and 12 μm. Even though WISE surveyed the sky in 22 μm as well, we have decided to discard the image in this wavelength because it shows very few point and compact sources and a great

component of extended emission. These images are centred on the equatorial coordinate $\alpha = 01^h28^m43.74^s$ and $\delta = +59°58'52.34''$ (J2000.0), have a size of 1000×1000 pixels, and a pixel scale of $1.3750''$.

As can be seen in Figure 3.1 (top-right, with 98% contrast stretching for visualisation purposes), a great number of the point sources disappear in the longer wavelength image ($WISE_{12}$), which has a more variable noisy background in which both point and extended sources are located, thus making this particular image a challenging example.

Radio frequency dataset

In the case of the radio band, we have selected two radio continuum images from the Canadian Galactic Plane Survey (CGPS, [94]). The CGPS surveyed a large portion of the Galactic Plane at different infrared, millimetre and radio (both continuum and spectral) frequencies. The radio continuum frequencies used were 1420 MHz (21 cm) and 408 MHz (74 cm). The radio images we have chosen correspond to the field centred at the equatorial coordinate $\alpha = 01^h40^m12.36^s$ and $\delta = +61°19'10.37''$ (J2000.0), with size 5×5 degrees approximately (1024×1024 pixels).

These radio images show mainly point sources, although a large extended emission is present in the top-right corner, as can be seen in Figure 3.1 (bottom-right, with 98% contrast stretching for visualisation purposes). Except for this extended source, the rest have a relatively small range of size. The $CGPS_{74}$ image shows fewer sources than the $CGPS_{21}$ image. The background is variable, and has a high component of noise. Moreover, there are some regions in the lower part of the images that contain missing values because the images are mosaics formed from circle-shaped images. In order to avoid possible problems because of these missing values, we have discarded the lower rows of the images' pixels.

3.2.2 Reference catalogues

A method to check whether the detections are true or not is needed in a quantitative evaluation. In order to do this, we have used public catalogues that cover the part of the sky shown in the dataset images.

In the particular cases of SDSS and WISE, specific public source catalogues are available together with the images [1, 19]. Specifically, we have used the SDSS-III primary imaging catalogue and the WISE All-Sky Source Catalog. They provide the coordinates as well as

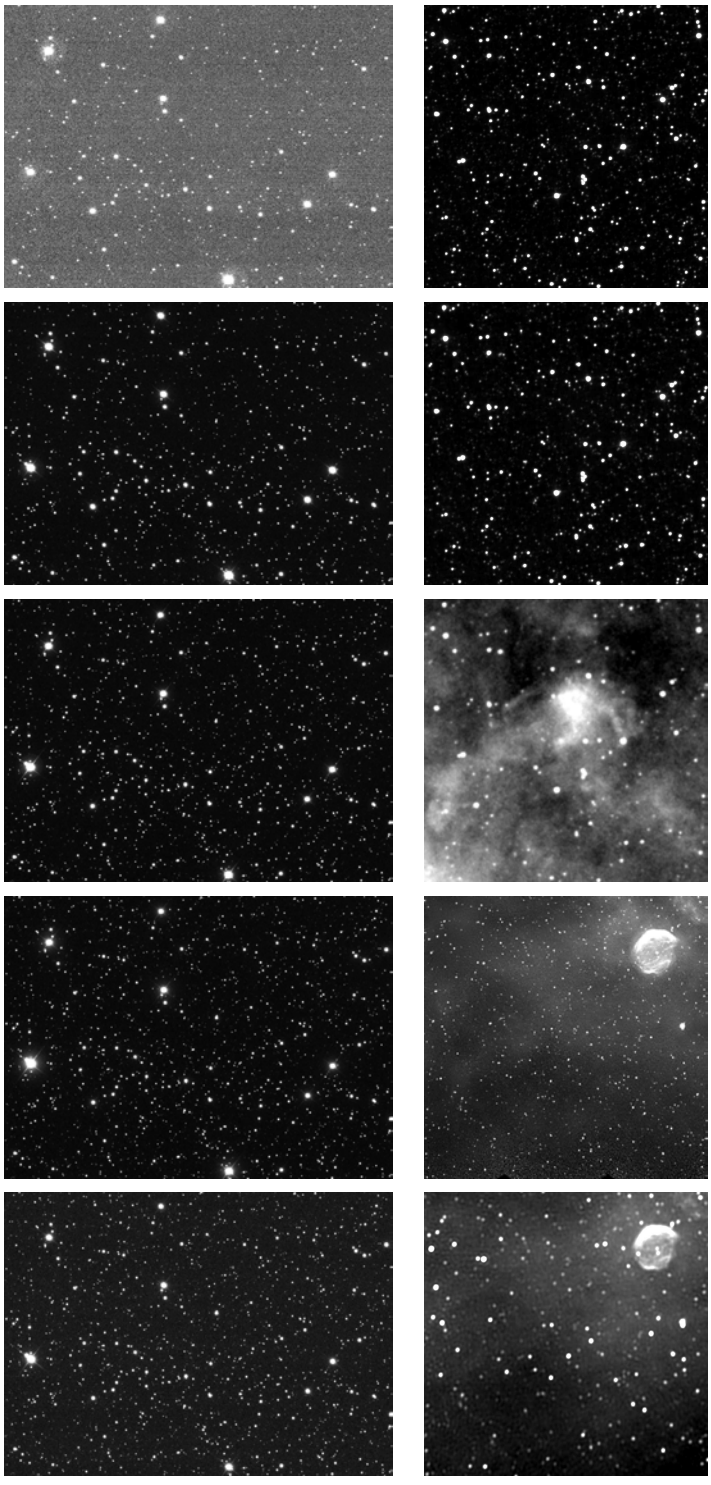

Figure 3.1: The three datasets. On the left, the u, g, r, i, and z optical images (from top to bottom). On the right, the 3.4, 4.6 and 12 μm infrared images, and the 21 and 74 cm radio images (from top to bottom).

photometric information on the sources at the different optical and infrared bands. On the other hand, a specific catalogue of the CGPS does not exist so we have used alternative catalogues of similar angular resolution just as [94] did. They cross-correlated the $CGPS_{21}$ and NVSS (NRAO VLA Sky Survey, [16]) catalogues at the same wavelength. As no prior calibrated survey was available at 74 cm, the photometric information on the sources in $CGPS_{74}$ was registered or matched to the logarithmic interpolation of the photometry of the previously mentioned NVSS catalogue and the Cambridge 7C(G) [102] catalogue at approximately 199 cm.

Hence, we have three datasets from well-known astronomical surveys that have also been featured in well-esteemed publications, which guarantees them as reliable references. However, the catalogues are usually computed with some detection software, such as that analyzed in this evaluation, and we cannot be certain that a semi-supervised procedure was not used to refine the source list. For this reasons, we have analyzed the accuracy of the catalogues individually with every image, and refined them. For each image, we have selected only the sources in its respective catalogue that are visible using the appropriate display system and have discarded others that are clearly imperceptible. In order to do this for each image, the sources of its respective catalogue were first limited to a photometric sensitivity of 3σ. Afterwards, each source was manually checked by experts in order to discard the sources that are imperceptible and add those that may have been missed by the catalogues. Finally, extended sources, specially the complex structures in $WISE_{12}$ and $CGPS_{74}$, objects with sizes that exceed a determined value and sources in contaminated areas, those affected by diffraction patterns and bright stars, have been excluded, as can be seen in Figure 3.2 (with 98% contrast stretching for visualisation purposes). Notice that no exclusion is applied to WISE3.4 and WISE4.6 images. Furthermore, the sources of each catalogue have been divided into three groups according to their brightnesses (faint, mid-intensity and bright). Therefore, the results of the different methods can also be analyzed in terms of the source intensity. Table 3.3 shows the main properties of the resulting refined catalogues for each image. Column one indicates the image's name, columns two and three the number of sources and the photometric range at a significance level of 3σ. Column four indicates the cut-off from which sources have been considered too big (in terms of arseconds of their major axis length) to be in the catalogue. Columns five, six and seven depict the brightness ranges of the three groups into which the catalogues have been broken down according to the brightness of the sources (faint, mid-intensity and bright). Columns eight and nine show the number of sources manually removed and inserted in the refinement of the catalogues. Note that the names in column one (assigned

by us) show the survey where the specific images and their bands come from, with the purpose of differentiating the images used in this evaluation. The brightness ranges are in the same units used in the catalogue (magnitude in SDSS and WISE and mJy in CGPS)

3.2.3 Evaluation measures

Using the reference catalogues presented in the previous section as ground truth, it is possible to obtain an estimation of the performance of the methods. As mentioned in Section 2.3.1, in the astronomical source detection literature, most of the results are evaluated in order to discern which detections are truly objects. In this regard, we have decided to follow this widely used practice and base the evaluation of the results on measures such as true positives (TP), false positives (FP) or false negatives (FN).

Another interesting measure related to those mentioned above is the number of true sources correctly detected (TSD), clearly a representative measure of the goodness of the detections. It is obtained by dividing the number of TP by the number of sources expected to be found, i.e., the number of sources in the reference catalogue. Therefore, we take into account the number of TP, FP and FN, but mainly the rate of TP (reliability) and TSD (completeness). The rate of FP and FN are in fact their complementary percentages, and thus, TP rate + FP rate = 100% and TSD rate + FN rate = 100%. The TP rate is achieved by dividing the number of TP by the number of detections obtained, whereas the TSD rate is achieved by dividing the number of TP by the number of sources in the catalogue. In the astronomical domain these measures are referred to as reliability and completeness, although some authors use different nomenclature. For instance in the pattern recognition field, reliability is referred to as precision while completeness is referred to as recall or sensitivity. To sum up, reliability = $\frac{TP}{TP+FP}$ and completeness = $\frac{TP}{TP+FN}$.

The strategy used to match the detections with the sources in the reference catalogue is the following: first, the closest detection for each source in the catalogue is found. Second, associations between sources and detections that are further away than a pre-established maximum distance are deleted. We assume that the centre of two different sources cannot be closer than the FWHM of the image, so this is the maximum distance selected. Next, where detections associated with more than one source from the catalogue are found, only the closest association is kept, deleting the others. In the same way, if a true source is associated with more than one detection, only the correspondence with the shortest distance is saved. Finally, the evaluation measures are computed: TP are the detections associated with a source, FP are detections without any associated source, while FN are

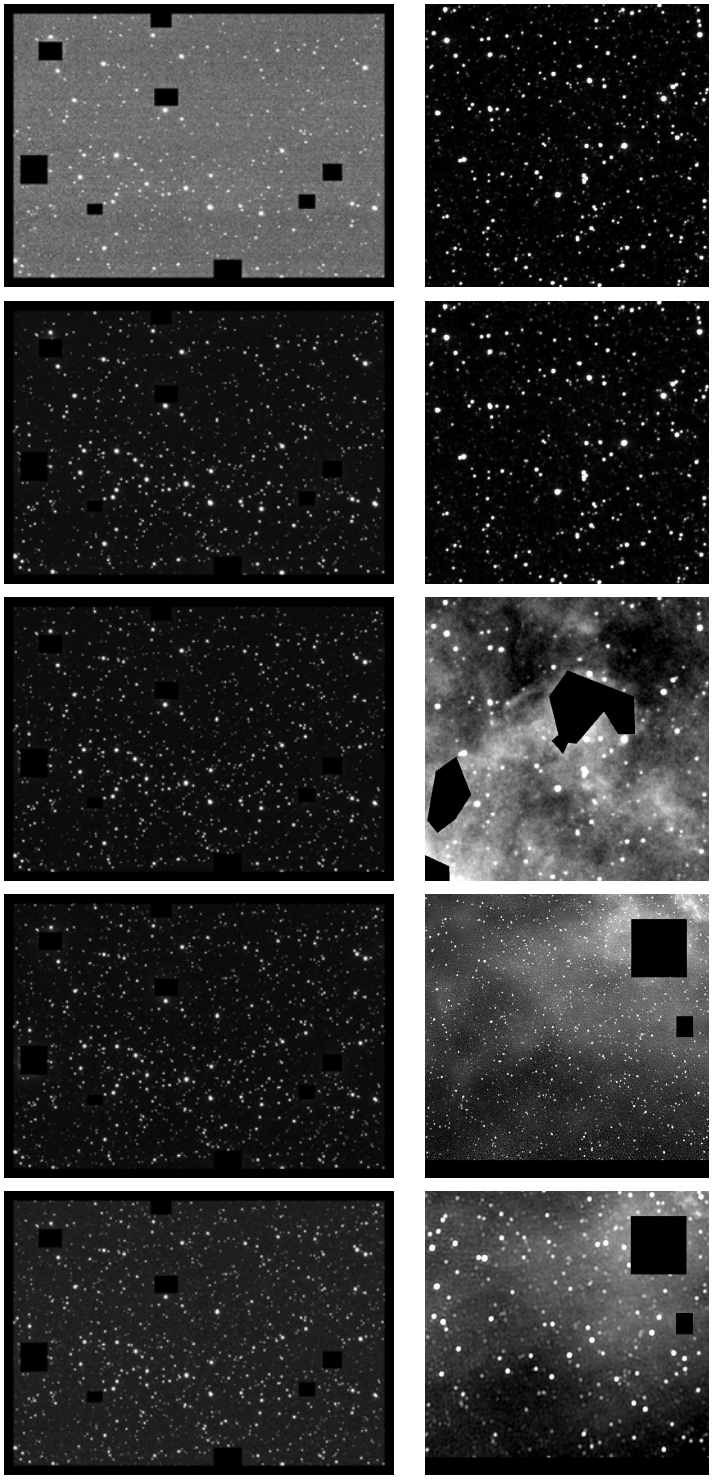

Figure 3.2: The three datasets with some problematic regions excluded. On the left, the u, g, r, i, and z optical images (from top to bottom). On the right, the 3.4, 4.6 and 12 μm infrared images, and the 21 and 74 cm radio images (from top to bottom).

Table 3.3: List of the catalogues used for each image.

Image	Number of sources	Photometric range (3σ)	Size cut-off ($''$)	Faint sources range	Mid-intensity sources range	Bright sources range	Sources removed	Sources inserted
$SDSS_u$	651	[22.00, 14.57]	13	[22.00, 19.52]	[19.52, 17.01]	[17.01, 14.57]	71	12
$SDSS_g$	1631	[22.20, 13.60]	13	[22.20, 19.33]	[19.33, 16.47]	[16.47, 13.60]	105	13
$SDSS_r$	2683	[22.20, 13.42]	10	[22.20, 19.28]	[19.28, 16.35]	[16.35, 13.42]	216	16
$SDSS_i$	2854	[21.30, 12.69]	9	[21.30, 18.43]	[18.43, 15.55]	[15.55, 12.69]	226	10
$SDSS_z$	2748	[20.50, 12.36]	9	[20.50, 17.79]	[17.79, 15.08]	[15.08, 12.36]	197	19
$WISE_{3.4}$	1701	[14.90, 7.21]	35	[14.90, 12.34]	[12.34, 9.78]	[9.78, 7.21]	-	30
$WISE_{4.6}$	1426	[14.90, 7.29]	35	[14.90, 12.37]	[12.37, 9.81]	[9.81, 7.29]	-	20
$WISE_{12}$	249	[12.30, 7.20]	40	[12.30, 10.60]	[10.60, 8.87]	[8.87, 7.20]	209	116
$CGPS_{21}$	1235	[2.18, 673.54]	378	[2.18, 14.66]	[14.66, 99.44]	[14.66, 673.54]	189	30
$CGPS_{74}$	561	[2.00, 1885]	472	[2.00, 19.83]	[19.83, 184.89]	[19.83, 1885]	60	164

sources with no associations with a detection.

Another factor to bear in mind when evaluating various software is the computational cost. The different codes have been executed using an Intel Core 2 Quad Q9550 processor (2.83 GHz) with 8 GB of RAM memory.

3.2.4 Experimental results

Each method has been executed with its proper parameter tuning, described in Section A.1 of Appendix A, and as a result, we have obtained a list of coordinates corresponding to the detections, (the candidates to be true sources). Using the reference catalogues and the evaluation measures, we have achieved a set of quantitative results that can be interpreted and compared. Tables 3.4, 3.5, and 3.6 correspond to the optical, infrared, and radio datasets respectively, and show the results obtained by each method in terms of number of detections, TP, FP, FN, TSD, and computational time. The columns indicate the method, the number and percentage of true positives, the number of false positives and false negatives, the percentage of true sources detected, and the time consumed. The measures that best indicate a good or bad performance by the methods are the percentages of TP and TSD (FP and FN are complementary), as well as the mean of these values for all the images in each dataset. The TP rate can be seen as the reliability of the detections whereas the TSD rate can be seen as the detection capacity of the method. Obviously, the higher these rates, the better the methods' performances. Notice that from this point on we only analyze the results in terms of percentages, specially that of TP (reliability) and TSD (completeness).

Furthermore, the detections have also been analyzed in terms of the brightness of the sources detected. In order to do this we grouped the sources in the catalogues according to the photometric values they present. Specifically, we divided the dynamic range of the sources into three bins corresponding to faint, mid-intensity and bright sources. Thus, we can discuss the methods' performance as depending on their ability to identify faint or bright sources.

Regarding the results of the optical dataset, we noticed that in more than half the cases, the rate of TSD obtained in SDSS_u is substantially smaller than the values of the other images, probably because in this image the noise pattern is more marked. In general, all the methods present a relatively high percentage of TP with values close to or even higher than 90%, such as Astrometry.net with 97.13%, Mopex with 96.13%, GN with

95.81%, or Perret with 94.38%. On the other hand, the method that presents a low level of TP is SAD, with 67.74%, although this low percentage is compensated by giving a good performance in terms of TSD (83.30%). Other methods with similar TSD rates are SExtractor with 85.84% (the best in terms of TSD) and SourceMiner with 80.38%. The rest of the methods are able to find more than half the true sources in the images (the Astrometry.net method presents the lowest TSD rate with 51.94%). The faster methods are SExtractor and Astrometry.net which take less than a second to obtain detections. SourceMiner is clearly the slowest method since it obtained detections in approximately eighteen minutes for the optical images.

Concerning the infrared dataset, there is a greater variability among the results, and there is not a band that stands out for its high or low rates. Depending on the method, its TP and TSD percentages are better in some wavelengths than in others. That instability is due to the fact that more than half the methods detect fewer true sources in $WISE_{12}$ than in the other bands. Moreover, five methods detected less than a third of the true sources in this image. This is due to the fact that it presents a structured background that complicates the separation between sources and background. As a whole, the TP rates are also inhomogeneous. GN is the method that offers the best mean rate with 96.84%, although it is closely followed by Perret, SourceMiner and DS all with rates above 90%. On the other hand, SExtractor has slightly more than 60%. The dominant note in TSD is to have values between 50% and 70%. SourceMiner and SExtractor perform best in terms of TSD (69.57% and 68.82%, respectively). Astrometry.net also presents acceptable results (63.84%). The methods that needed less time to perform the detections were SExtractor, DS, and Astrometry.net, all three with less than a second. On the other hand, the method that required the most time was Mopex, which took up to two or three minutes to perform its executions.

In the radio dataset, five of the eight methods achieved lower TP rates in $CGPS_{21}$ than in $CGPS_{74}$, whereas in the case of the TSD, rate the reverse is true since, with all the methods except for Mopex, values are higher in $CGPS_{21}$ than in $CGPS_{74}$. SExtractor is the method with the worst TP rate and the best TDS rate (47.70% and 82.33%). In contrast, DS is the method with best TP rate and the worst TDS rate (91.20% and 36.15%). These two percentages are more balanced in the rest of the methods. Another method that stands out positively is Perret with a 93.27% TP rate, and Perret (65.22%), SourceMiner (65.21%) and GN (61.18%) in terms of TSD. As with the other datasets, Astrometry.net, SExtractor, and DS take less than a second per execution, while Mopex can take more than one and a half minutes in the worst case.

Table 3.4: Results obtained by the various methods with the optical dataset (SDSS). For each method, each row represents the bands u, g, r, i, and z (in this order), and the last row is the mean and the standard deviation of the five bands.

Method	Detections	TP	TP (%)	FP	FN	TSD (%)	Time (s)
SExtractor[c]	529	509	96.22	20	142	78.19	0.35
	1826	1436	78.64	390	195	88.04	0.43
	2565	2387	93.06	178	296	88.97	0.44
	3055	2590	84.78	465	264	90.75	0.56
	2377	2288	96.26	89	460	83.26	0.35
			89.79 ± 7.80			**85.84 ± 5.10**	
SAD[f]	1131	512	45.27	619	139	78.65	14.90
	2411	1366	56.66	1045	265	83.75	6.30
	3293	2278	69.18	1015	405	84.90	15.20
	3038	2474	81.44	564	380	86.69	13.10
	2633	2268	86.14	365	480	82.53	6.40
			67.74 ± 17.00			**83.30 ± 3.02**	
Mopex[p]	604	504	83.44	100	147	77.42	359.80
	1227	1186	96.66	41	445	72.72	271.50
	1692	1624	95.98	68	1059	60.53	251.00
	2178	2102	96.51	76	752	73.65	258.50
	2296	2190	95.38	106	558	79.69	317.50
			96.13 ± 0.58			**72.80 ± 7.42**	
GN[m]	487	454	93.22	33	197	69.74	132.64
	824	801	97.21	23	830	49.11	128.36
	1143	1113	97.38	30	1570	41.48	128.60
	1838	1735	94.40	103	1119	60.79	131.53
	1487	1440	96.84	47	1308	52.40	132.83
			95.81 ± 1.88			**54.71 ± 10.89**	
SourceMiner[i]	561	536	95.54	25	115	82.33	1066.00
	1259	1220	96.90	39	411	74.80	1064.00
	1868	1798	96.25	70	885	67.01	1049.00
	2944	2569	87.26	375	285	90.01	1067.00
	2604	2411	92.59	193	337	87.74	1055.00
			93.71 ± 3.96			**80.38 ± 9.49**	
Astrometry.net[c]	303	289	95.38	14	362	44.39	0.57
	1038	1005	96.82	33	626	61.62	0.83
	1442	1413	97.99	29	1270	52.66	0.64
	1717	1672	97.38	45	1182	58.58	0.77
	1189	1166	98.07	23	1582	42.43	0.60
			97.13 ± 1.10			**51.94 ± 8.45**	
DS[m]	269	242	89.96	27	409	37.17	1.16
	998	875	87.68	123	756	53.65	1.30
	1642	1496	91.11	146	1187	55.76	1.34
	2180	1988	91.19	192	866	69.66	1.54
	2062	1879	91.13	183	869	68.38	1.37
			90.21 ± 1.51			**56.92 ± 13.19**	
Perret[N/A]	397	370	93.20	27	281	56.84	-
	1573	1424	90.53	149	207	87.31	-
	2278	2174	95.43	104	509	81.03	-
	1851	1772	95.73	79	1082	62.09	-
	1803	1749	97.00	54	999	63.65	-
			94.38 ± 2.55			**70.18 ± 13.20**	

Table 3.5: Results obtained by the various methods with the infrared dataset (WISE). For each method, each row represents the bands of 3.4, 4.6, and 12 μm (in this order), and the last row is the mean and the standard deviation of the four bands.

Method	Detections	TP	TP (%)	FP	FN	TSD (%)	Time (s)
SExtractor^c	1739	1169	67.22	570	532	68.72	0.41
	1448	979	67.61	469	447	68.65	0.37
	368	172	46.74	196	77	69.08	0.21
			60.52 ± 11.94			**68.82 ± 0.23**	
SAD^f	1625	1435	88.31	190	266	84.36	4.80
	1326	1072	80.84	254	354	75.18	4.40
	49	49	100.00	0	200	19.68	0.50
			89.72 ± 9.66			**59.74 ± 35.00**	
Mopex^p	526	520	98.86	6	1181	30.57	89.10
	314	304	96.82	10	1122	21.32	87.00
	384	98	25.52	352	151	39.36	92.60
			73.73 ± 41.76			**30.42 ± 9.02**	
GN^m	1420	1349	95.00	71	352	79.31	42.18
	1117	1067	95.52	50	359	74.82	42.69
	60	60	100.00	0	189	24.10	42.55
			96.84 ± 2.75			**59.41 ± 30.66**	
SourceMiner^i	1663	1494	89.84	169	207	87.83	18.00
	1485	1260	84.85	225	166	88.36	17.00
	81	81	100.00	0	168	32.53	17.00
			91.56 ± 7.72			**69.57 ± 32.08**	
Astrometry.net^c	1329	1172	88.19	157	529	68.90	0.64
	1133	964	85.08	169	462	67.60	0.60
	262	137	52.29	125	112	55.02	0.77
			75.19 ± 19.89			**63.84 ± 7.67**	
DS^m	1160	1022	88.10	138	679	60.08	0.50
	742	665	89.62	77	761	46.63	0.57
	79	75	94.94	4	174	30.12	0.40
			90.89 ± 3.59			**45.61 ± 15.01**	
Perret$^{N/A}$	448	445	99.33	3	1256	26.16	-
	392	389	99.23	3	1037	27.28	-
	227	175	77.09	52	74	70.28	-
			91.89 ± 12.81			**41.24 ± 25.16**	

Table 3.6: Results obtained by the various methods with the radio dataset (CGPS). For each method, each row represents the bands of 21 and 74 cm (in this order), and the last row is the mean and the standard deviation of the two bands.

Method	Detections	TP	TP (%)	FP	FN	TSD (%)	Time (s)
	2907	1076	37.01	1831	159	87.13	0.33
SExtractor[c]	745	435	58.40	310	126	77.54	0.37
			47.70 ± 15.11			**82.33 ± 6.78**	
	956	825	86.30	131	410	66.80	4.90
SAD[f]	254	227	89.37	27	334	40.46	12.10
			87.83 ± 2.17			**53.63 ± 18.62**	
	1058	496	46.88	562	739	40.16	88.90
Mopex[p]	307	260	84.69	47	301	46.35	89.80
			65.79 ± 26.74			**43.25 ± 4.37**	
	1558	1051	67.46	507	184	85.10	76.68
GN[m]	219	209	95.43	10	352	37.25	76.34
			81.45 ± 19.78			**61.18 ± 33.83**	
	1015	882	86.90	133	353	71.42	21.00
SourceMiner[i]	408	331	81.13	77	230	59.00	22.00
			84.01 ± 4.08			**65.21 ± 8.78**	
	1126	810	71.94	316	425	65.59	0.33
Astrometry.net[c]	372	286	76.88	86	275	50.98	0.19
			74.41 ± 3.50			**58.28 ± 10.33**	
	619	567	91.60	52	668	45.91	0.45
DS[m]	163	148	90.80	15	413	26.38	0.37
			91.20 ± 0.57			**36.15 ± 13.81**	
	930	869	93.44	61	366	70.36	-
Perret[N/A]	362	337	93.09	25	224	60.07	-
			93.27 ± 0.25			**65.22 ± 7.28**	

3.3 Discussion

As we have seen, different approaches present different results. Nevertheless, a clear pattern emerges: the TP and TSD rates appear anti-correlated. In other words, the apparent certainty that the detections performed by one particular method are true sources implies that it misses a lot of other true sources, and in turn, the detection of a great many of true sources implies that many spurious detections are considered as true sources. For instance, in optical images, Astrometry.net achieves 97.13% TP and 51.94% TSD, while SAD achieves 67.74% TP and 83.30% TSD. The same happens in infrared images, with Perret (91.89% TP and 41.24% TSD) and SExtractor (60.52% TP and 68.82% TSD), and in radio images, with DS (91.20% TP and 36.15% TSD) and SExtractor (47.70% TP and 82.33% TSD). A point that can also be made in light of these results is that there are methods that can achieve more than 90% and even almost 100% TP, whereas in the case of TSD this is not possible as it achieves only around 80% for optical and radio images, and almost 70% for infrared images as its best results. Thus, pointing out the difficulty of detecting an important number of true astronomical sources. According to the results, we consider that, in all types of images, good TP rates are those that are close to or above 90%. On the other hand, good TSD rates are those above 70% in optical images and close to or above 60% in infrared and radio images.

3.3.1 Performance of the detection methods

Figures 3.3, 3.4, 3.5 and 3.6 summarize the results obtained by the different methods in the three datasets. In the first figure, a global overview of the results is depicted while in the second the TSD percentages are broken down into three groups according to the source brightness (faint, mid-intensity and bright). We can see that SExtractor is accurate when detecting in optical images (88.79% TP), and imprecise when detecting at infrared and radio wavelengths (60.52% and 47.70% TP, respectively). On the other hand, it is able to detect more than two-thirds of the infrared sources (68.82% TSD) and remarkably 85.84% and 82.33% of the optical and radio sources, respectively. In fact, this is the method with the best TSD percentages in the optical and radio bands, and one of the best in the infrared band. Therefore, SExtractor is a method that guarantees a high level of completeness of detections. It is also able to detect a very good number of faint and mid-intensity radio sources. Furthermore, it does not need any parameters to perform detections. For the images selected, it is also able to provide a list of detections almost instantaneously, factors that make it very useful to the astronomical community.

SAD detects quite accurately in infrared and radio images (with 89.72% and 87.83% TP, respectively) but fails in the optical band (67.74% TP). The TP rate in the optical band can be increased by choosing different thresholds, although at the expense of achieving lower TSD rates. In turn, it is a very good method to detect true optical sources, reaching 83.30%. Additionally, acceptable TSD rates close to 60% are obtained in the infrared and radio datasets, demonstrating the validity of Gaussian fitting when detecting compact sources at the specific frequencies of the three datasets. It is a satisfactory method to detect faint optical and infrared sources, except for WISE_{12} due to the background variability. SAD executes its detection strategy in a few seconds, but apart from the optical dataset, requires appropriate tuning to get acceptable results. It is likely that additional, more complex parameters that have not been tested in this work could improve the results slightly.

Mopex is a method that provides very reliable detections with the optical dataset (96.13% TP rate) but much lower in the other two datasets (73.73% and 65.79% TP rate). In addition, it is not particularly good at detecting true sources, with 72.80% TSD in optical images, 30.42% TSD in infrared images, and 43.25% TSD in radio images. These low rates can be ascribed to the low number of faint infrared and radio sources identified. This is most probably due to the fact that among its parameters it requires a sample of the sources to be found in the image, and the images selected present sources with divergent characteristics such as shape, size, brightness, or the surrounding background. For this reason, we consider that this method is more appropriate when images present a low dynamic range. As happens with SAD, there are other parameters that may vary the results slightly. Furthermore, it takes between half a minute and over six minutes to finish its execution, which is significantly slower than other methods.

González-Nuevo (GN) presents reliable detections, especially in optical and infrared bands with 95.81% and 96.84% TP respectively, and to a lesser degree in radio images (81.45% TP). Furthermore, it is able to detect a satisfactory number of true sources in radio (61.18%) and infrared images (59.41%). On the other hand, 54.71% of true optical sources detected is representatively lower than the best methods in these bands. A substantial number of sources close to the detection limits is missed due to the fact that multiscale techniques are suitable when images present complex sources and backgrounds such as the ones that can be present in infrared and radio images. In the case of the optical dataset, the signal gain is probably not as important as in the other two datasets. A point in favour of GN is that it only needs one empirical parameter to obtain detections. On the contrary, its computational cost is proportional to the size of the image, and it takes up

to more than two minutes.

SourceMiner is one of the most accurate methods when detecting optical (93.71% TP) and infrared (91.56% TP) sources, but its reliability decreases slightly with radio images (84.01% TP). In turn, it is particularly good at identifying true sources at all the wavelengths analyzed, with remarkable values of 80.38% in the optical bands, 69.57% in the infrared bands and 65.21% in the radio bands. This happens because of the fact that, unlike most of the other methods, it performs specially well with fainter sources. All these results show that SourceMiner is able to generate accurate models for both sky and sources. Although several spurious detections have been found, is able to identify a good number of true sources. As with GN, it only needs an empirical parameter to obtain detections. Its main drawback is the computational cost, which is a function of the size of the image, and in the case of the optical dataset can even take more than eighteen minutes.

Astrometry.net offers high accuracy in detecting optical (a TP rate of 97.13%), but not such good rates with infrared and radio sources (approximately two-thirds of TP). However, it is a good method to find a large number of true infrared and radio sources (63.84% and 58.28% TSD). As a matter of fact, it is one of the few methods that is able to detect faint sources in $WISE_{12}$ and $CGPS_{74}$. However, it provides a weaker performance when detecting optical sources (51.94% TSD), mainly because it misses several bright and mid-intensity sources. The very short time needed to provide the detections and the fact that it can work without any parameter tuning are two advantages that make Astrometry.net a really handy method.

In terms of TP, Distilled Sensing (DS) offers a very good performance with all the datasets with percentages above 90%, proving that it is a method that guarantees high reliability on its detections. However, in terms of TSD, lower rates than the best methods are obtained, specially in the radio images. In general, it provides similar FN rates in sources of different brightness. As it depends on one parameter that has to be set empirically, DS needs to be carefully tuned to achieve the best results. On the other hand, one of its main advantages is its great execution speed.

Perret is another very precise method since its TP rates clearly exceed 90%. In addition, it also presents good rates of TSD in two of the three datasets. In this case, in optical and radio bands 70.18% and 65.22% TSD are obtained, having lower results in the infrared dataset with 41.24%. In general, this method is able to identify correctly very good percentages of brighter sources. Furthermore, it is the method that best deals with faint

sources in $WISE_{12}$, identifying more than half. As the Perret code was executed directly by its authors, we do not have information about its parameter setting or computational cost.

In this particular quantitative evaluation, the different methods provide individual detection lists for each single image. However, other existing tools are able to work with a set of images at different wavelengths simultaneously, thus providing multiwavelength catalogues. In this way, source deblending, for example, can be solved by checking source counterparts in higher-frequency images. A recent multiscale method that follows this procedure is Getsources (Men'shchikov et al. (2012) [63]) designed primarily for use in far-infrared images but can also be applied to other types of astronomical images. In short, each wavelength is first decomposed into several scales by means of filtering with circular Gaussian profiles and subtracting them from one another. Afterwards, noise and background contributions are subtracted at each scale by means of a σ-clipping thresholding. Finally, detections are identified by shape and position, tracking from small to large scales. When testing Getsources with our three datasets, it provided values of 91.80% TP and 86.44% TSD rates, 98.91% TP and 68.33% TSD rates, and 99.29% TP and 56.52% TSD rates for optical, infrared, and radio datasets, respectively. As can be seen with these results, this method is able to obtain very high percentages of TP as well as remarkable rates of TSD, proving that this different way of obtaining detection lists in aggregate form is a perfectly valid alternative to the tested methods.

3.3.2 Image datasets

The difficulty of having good results in both TP and TSD becomes evident. Consequently, the importance of giving more priority to one of the two measures arises, and selecting a detection method according to that priority. Generally, the methods that provide better TP rates are the DS and Perret approaches, whereas the methods with higher rates of TSD are SourceMiner and especially SExtractor. As seen in the previous section, all the tools present a poor performance when dealing with faint sources, specially in images with higher wavelengths in each dataset. The methods with a nice balance between the two measures are SExtractor, SAD, and SourceMiner, which makes them the best methods when dealing with different types of images. An overview of the various methods' performances is presented in Table 3.7. It should be born in mind that the resultant conclusions have been drawn from particular types of images with specific characteristics, and cannot entirely represent the performance of the methods in the whole range of optical, infrared and radio

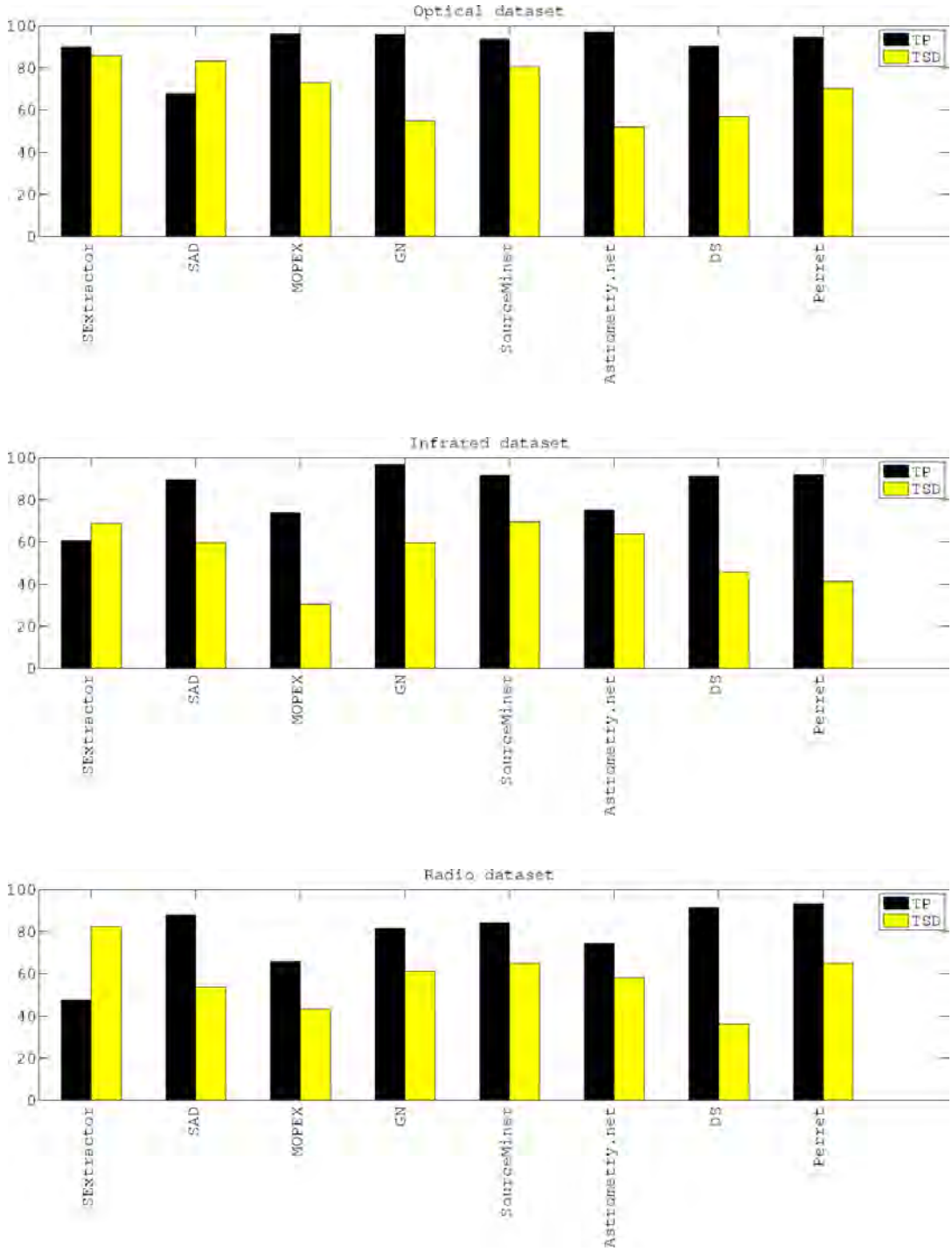

Figure 3.3: Graphical representation of the TP and TSD of the different methods in the three different datasets.

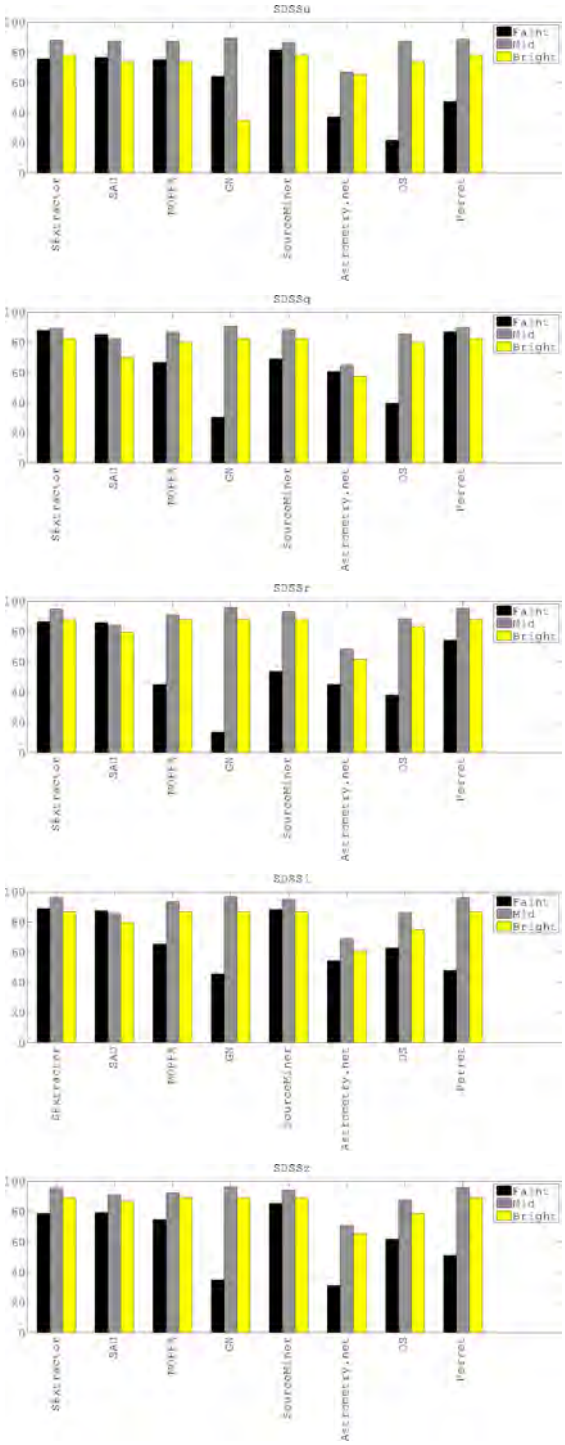

Figure 3.4: Graphical representation of the percentages of TSD in the optical dataset according to the brightness of the sources. From top to bottom, the results obtained with the different methods with the images SDSS_u, SDSS_g, SDSS_r, SDSS_i and SDSS_z.

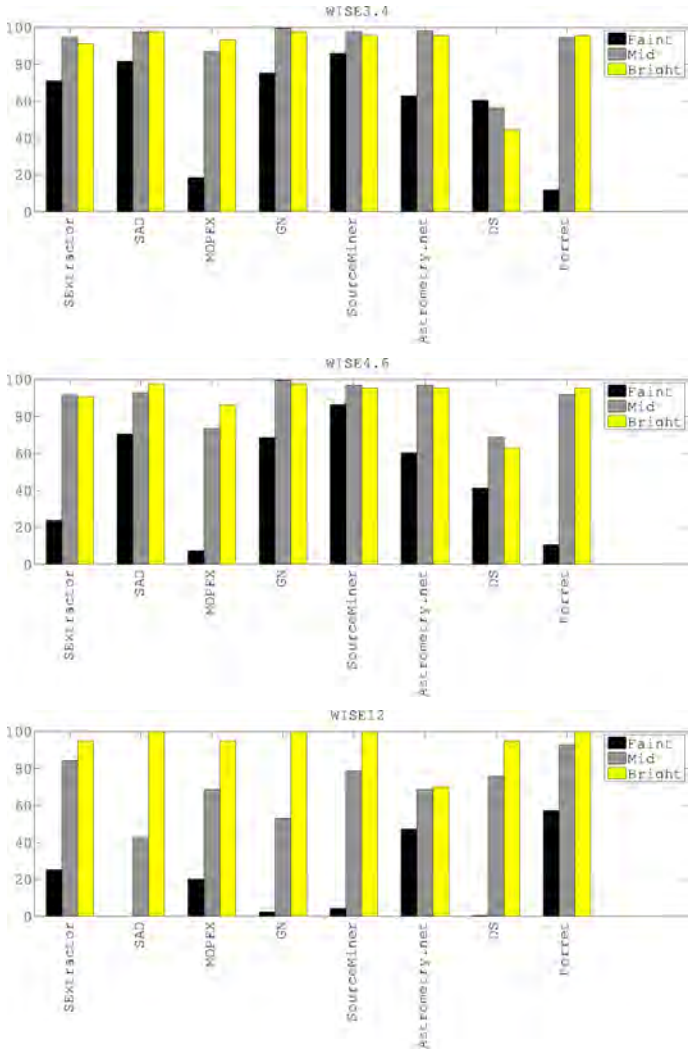

Figure 3.5: Graphical representation of the percentages of TSD in the infrared dataset according to the brightness of the sources. From top to bottom, the results obtained with the different methods with the images $\text{WISE}_{3.4}$, $\text{WISE}_{4.6}$ and WISE_{12}.

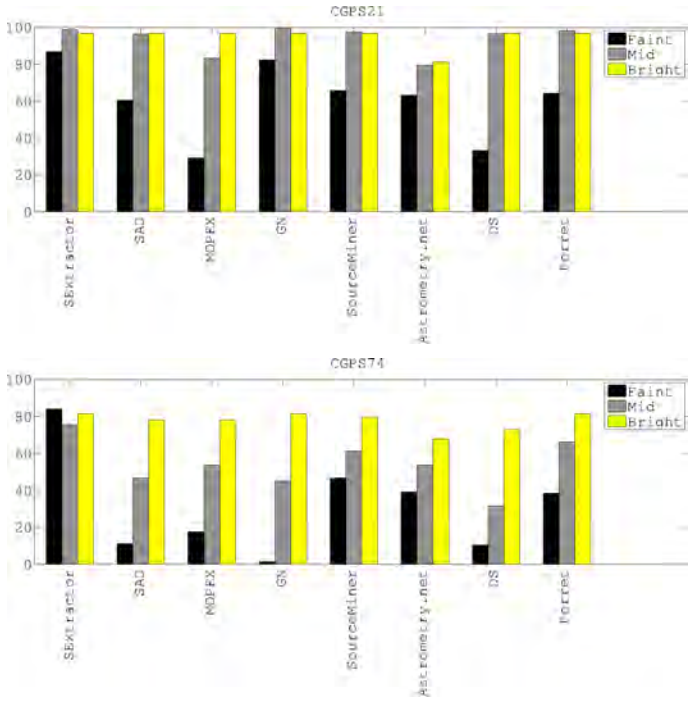

Figure 3.6: Graphical representation of the percentages of TSD in the radio dataset according to the brightness of the sources. From top to bottom, the results obtained with the different methods with the images $CGPS_{21}$ and $CGPS_{74}$.

astronomical images.

In optical images, all the methods except for SAD provide a good percentage of TP, but in terms of TSD, SExtractor is the best, closely followed by SAD and SourceMiner. The methods with more balanced results and therefore recommended for use in optical images are SExtractor and SourceMiner.

In the case of infrared images, very high values in TP rates are difficult to obtain except with GN. The same happens with the TSD rate, where only SourceMiner, SExtractor and Astrometry.net achieve high percentages. In general, the methods with the most interesting results in infrared images are SExtractor and Astrometry.net. Most of the methods are able to find almost all of the brighter sources, however, they make a lot of mistakes with faint sources, specially in $WISE_{12}$ where the complexity of the background complicates their detection. The best method to identify faint infrared sources is SourceMiner.

Only two methods achieve high rates of TP in the radio dataset; DS and Perret. However, only Perret is able to detect a great number of the sources in the reference catalogues. SourceMiner, GN, and specially SExtractor are the other methods with the best TSD rates. The most interesting methods with radio images are GN, SourceMiner and Perret. Generally, most of the methods detect good percentages of sources of different brightness in $CGPS_{21}$. However, in $CGPS_{74}$, an important number of FN is achieved by most of the methods when detecting fainter sources. Hence, the methods that best deal with fainter optical sources are Astrometry.net, SourceMiner and Perret.

3.3.3 Detection strategy

We have also taken into account the assumption that the various approaches should operate differently with the three different datasets. For instance, SExtractor, DS and Astrometry.net are methods based on simple image transformations. This group covers a wide range of techniques, and therefore, presents divergent results with all types of images. This inhomogeneity is due to the fact that they are based on simple procedures and therefore, are not the most significant step in the detection process. Other complementary image transformation steps or even the detection criterion may be more representative of the detection performance. These techniques have provided high TP rates in the optical and significantly lower percentages in the infrared and radio datasets. They also offer admissible TSD rates with infrared and radio images. Hence, we claim that simple image transformation is a good option when dealing with optical images, and are useful in some situations when the aim is to detect sources in infrared and radio images because they can

Table 3.7: Overview of the different methods reviewed with their main advantages and drawbacks in each dataset.

Method	Optical dataset		Infrared dataset		Radio dataset	
	Strengths	Weaknesses	Strengths	Weaknesses	Strengths	Weaknesses
SExtractor	Acceptable TP rate High TSD rate Fully automatic Very low computational cost	-	High TSD rate Fully automatic Very low computational cost	Low TP rate	High TSD rate Fully automatic Very low computational cost	Low TP rate
SAD	High TSD rate Fully automatic Low computational cost	Low TP rate	Acceptable TP rate Acceptable TSD rate Simple tuning Low computational cost	-	Acceptable TP rate Acceptable TSD rate Simple tuning Low computational cost	-
Mopex	Very high TP rate Acceptable TSD rate Simple tuning	High computational cost	Acceptable TP rate Simple tuning	Low TSD High computational cost	Simple tuning	Low TP rate Low TSD rate High computational cost
GN	Very high TP rate Simple tuning	Low TSD rate High computational cost	Very high TP rate Acceptable TSD rate Simple tuning	High computational cost	Acceptable TP rate High TSD rate Simple tuning	High computational cost
SourceMiner	High TP rate High TSD rate Simple tuning	High computational cost	High TP rate High TSD rate Simple tuning	High computational cost	Acceptable TP rate High TSD rate Simple tuning	High computational cost
Astrometry.net	Very high TP rate Fully automatic Very low computational cost	Low TSD rate	Acceptable TP rate High TSD rate Fully automatic Very low computational cost	-	Acceptable TP rate Acceptable TSD rate Fully automatic Very low computational cost	-
DS	High TP rate Very low computational cost	Low TSD rate Difficult tuning	High TP rate Very low computational cost	Low TSD rate Difficult tuning	High TP rate Very low computational cost	Low TSD rate Difficult tuning
Perret	High TP rate Acceptable TSD rate	-	High TP rate	Low TSD rate	High TP rate High TSD rate	-

deal with noisy inhomogeneous backgrounds.

Bayesian approaches are represented by SourceMiner. This is a balanced method in all types of images, which makes it a good choice under any circumstances. Therefore, Bayesian approaches are useful when there is not a clear priority to maximize the TP or the TSD, and it ensures acceptable percentages in both rates.

In the case of matched filtering (MF), represented by Mopex, this technique offers acceptable detection reliability. However, from the point of view of the true sources identified, its performance decreases noticeably in all types of images. For this reason, we consider that while MF provides few detections in general, most of them have been correctly detected as true sources. Furthermore, this technique is more appropriate when the sources are similar in size and shape and have a low dynamic range. Contrary to what was stated in Section 2.4, MF does not provide better results in the radio dataset than in the other two.

Finally, GN is a multiscale method based on the wavelet transform . From the results of this method , we can conclude that multiscale strategies perform very well in terms of TP. Furthermore, it provides an acceptable TSD rate in all datasets. In general, the results are good enough to take multiscale approaches into account in any type of astronomical image, even in optical wavelengths, in spite of the fact that in Section 2.4 this strategy was not usually employed in this band.

Concerning the detection criterion, thresholding and the local peak search are the two methods most used by far, and they are usually interchangeable, specially with point sources. For these reasons, this step in the whole source detection process is sometimes less meaningful than the image transformation. Nevertheless, from the results we conclude that the methods based on a local peak search (GN and SourceMiner) are suitable for infrared and radio bands since their TP and TSD rates are high enough, while in optical images they present low values in one or the other of the two.

Finally, representing thresholding, we find SExtractor, SAD, Mopex, Astrometry.net, and DS. In this case, the influence of the image transformation becomes apparent since the results of these techniques are different even though they share a generally good performance in optical images. This is due to the high contrast between most of the sources and the background, and a poor rate of TSD in infrared images.

3.4 Conclusions

In this chapter, we have presented a quantitative evaluation of eight of the most promising astronomical source detection methods developed in recent years. Unlike Chapter 2, where the comparison of the approaches was based mainly on a qualitative evaluation, this chapter outlines a new comparison based on quantitative measures obtained from the application of the different methods to a single dataset consisting of optical, infrared, and radio frequency images.

The quantitative comparisons have allowed us to identify the best methods for each image type. In most of the cases evaluated, the various methods have behaved according to their reported results in the literature. In addition, advantages and drawbacks of the different methods and techniques have been discussed (see Table 3.7 for a summary).

In both this quantitative evaluation and in the state-of-the-art review presented in the previous chapter, we have noticed that multiscale techniques, mostly based on the wavelet transform, are the most commonly-used to transform images. This is due to their ability to remove the background, filter the noise and highlight the sources. Furthermore, they have proven to be very reliable in the detections they provide in all bands and fairly complete, specially in lower frequencies such as infrared and radio. Hence, they will definitely be taken into account in our further detection proposals.

Other types of image transformation steps have also provided good results in some cases. Matched filtering and Bayesian approaches are able to achieve good percentages of TSD and specially TP in most images. By means of some prior knowledge, they are able to better characterize both sources and background but at the expense of having a high computational cost. On the contrary, basic image transformation steps present a very low computational cost and a fairly good performance. In the case of the widely-used algorithms SExtractor and SAD, apart from these useful techniques, they use optimized implementations in C programming language which makes them really fast and the best choice to be used as reference in the comparison of our new proposals. Moreover, is of special interest the DS method because, even when implemented in a inefficient platform like Matlab, it presents a very low computational cost. This, together with the fact that it is a reliable method, makes it very interesting to exploit.

Finally, referring to the detection criterion, we have already mentioned that thresholding and a local peak search can be used interchangeably. However, as can be seen in Table 3.1, more than half of the methods use threshnolding. To be coherent with this fact, we

will use this technique as well in our proposals, both with global and local thresholds.

Chapter 4

Faint source detection in aperture synthesis radio images

In the qualitative and quantitative evaluations presented in the previous chapters a myriad of techniques were presented, each with its respective strengths and weaknesses. From these conclusions, we have decided to develop different strategies that take advantage of some of the most outstanding and innovative techniques of the state of the art. In this chapter we explore the performance of three novel approaches based on very different strategies that are able to detect sources with intensities similar to noise levels. The first two algorithms are based on unsupervised strategies: the first uses a multiscale transform, while the second a pixel structural behaviour. The last algorithm is based on a supervised strategy that includes local feature extraction and a classification process.

In order to evaluate the performance of these three methods, we have used synthetic and real radio interferometric images. They often contain a large population of faint compact sources with intensity values close to the detection limit that are easily missed by detection methods. The real dataset consists of deep radio maps obtained with the Giant Metrewave Radio Telescope (GMRT) and the Australia Telescope Compact Array (ATCA). These types of images serve as an excellent benchmark for automated detection methods because they show a significant amount of detail due to their high spatial dynamic range, have a large population of compact sources and extended diffuse emission, and present unwanted interferometric patterns, caused mainly by deconvolution artefacts and grating rings from strong sources and possibly some correlator calibration problems. Furthermore, we include in our study a comparison with the well-known state of the art methods SExtractor and SAD (within AIPS).

4.1 Multiresolution analysis on thresholded images

The first method incorporates the concept of multiscale analysis, which is generally applied when the image to segment shows objects with very different sizes or patterns organized in a hierarchical structure [58, 59]. In these cases, there is not an optimal resolution for analyzing the image, and algorithms to process it at different resolutions are needed. Especially suited for this purpose are algorithms that decompose the image through a wavelet representation, using discrete versions of the wavelet transform [83, 91, 88].

Radio interferometric images often display hierarchically organized structures of objects with irregular patterns that can be represented at different spatial frequencies. Therefore, the analysis of such images with the purpose of detecting and classifying emitting sources is a clear example where multiscale methods can be conveniently applied [9].

Within this approach, wavelet decomposition is used as a tool to detect and separate objects of astronomical interest that can be represented at different spatial frequencies. We avoid ringing artefacts created around singularities, strong sources in the case of our radio images, by previously using thresholding techniques to remove brighter objects that are then replaced by local noise.

Multiscale vision models [9] decompose an image in several scales or wavelet planes and independently segment each of the images representing a scale. Low index scales highlight high spatial frequencies, whereas high index scales highlight low spatial frequencies. The mathematical decomposition of an image in a set of wavelet planes requires that, at each scale, the wavelet coefficient mean must be zero. Due to this fact, to compensate the highlighting of the bright sources in a given scale, negative values appear in their surroundings [91]. These negative values create artifacts that complicate the analysis.

Since astronomical sources are mostly isotropic, e.g. stars, clusters or galaxies, astronomers generally choose to use a wavelet transform that does not privilege any orientation in the image and also maintains the sampling at each scale [91]. For this reason, one of the widely used transforms in this field is the stationary wavelet transform (SWT) also called "à trous" algorithm. The SWT decomposes an image in several scales or wavelet planes and a smoothed array using a smoothing filter, associated with the wavelet scaling function, in the following way:

$$I(i,j) = F_N(i,j) + \sum_{n=1}^{N} W_n(i,j), \tag{4.1}$$

where $F_N(i,j)$ and $W_n(i,j)$ are calculated through the following iterative process:

$$\begin{aligned} F_0(i,j) &= I(i,j) \\ F_n(i,j) &= \langle H_n, F_{n-1} \rangle (i,j) \\ W_n(i,j) &= F_{n-1}(i,j) - F_n(i,j) \end{aligned} \tag{4.2}$$

with $n = 1, ..., N$ and

$$\langle H_n, F_{n-1} \rangle (i,j) \equiv \sum_{k,l} h(k,l) F_{n-1}(i + 2^{n-1}k, j + 2^{n-1}l), \tag{4.3}$$

where the set $W_1, W_2, ..., W_N, F_N$ represents the wavelet transform of the data. Following Starck et al. [91] and references therein, we will use the B_3-spline function as the scaling function, which is very similar to a Gaussian one. In this way, the mask associated with the filter h takes the following form:

$$h \equiv \frac{1}{256} \begin{pmatrix} 1 & 4 & 6 & 4 & 1 \\ 4 & 16 & 24 & 16 & 4 \\ 6 & 24 & 36 & 24 & 6 \\ 4 & 16 & 24 & 16 & 4 \\ 1 & 4 & 6 & 4 & 1 \end{pmatrix}. \tag{4.4}$$

Figure 4.1 shows the image wavelet decomposition in 6 scales plus the smoothed array using the "à trous" algorithm and the filter h.

4.1.1 Algorithm steps

Methods based on thresholding are suitable for the detection of bright sources but easily miss the fainter ones. In contrast, methods based on wavelet decomposition are not suitable when bright sources (singularities) are present due to the polluting artefacts they create in the decomposition, but are able to highlight faint sources. Hence, we propose a hybrid method where both techniques are used at different stages: in a first step, bright sources are detected using a traditional local thresholding and a residual image that does not contain them is produced. In this way we prevent the further creation of polluting artifacts. In a second step, a wavelet decomposition is applied to the residual image in order to detect faint compact objects. Since our aim is the detection of point and compact sources discarding the diffuse emission, we can select objects coming from the segmentation of the first three scales. Since the method is mainly based on wavelets and

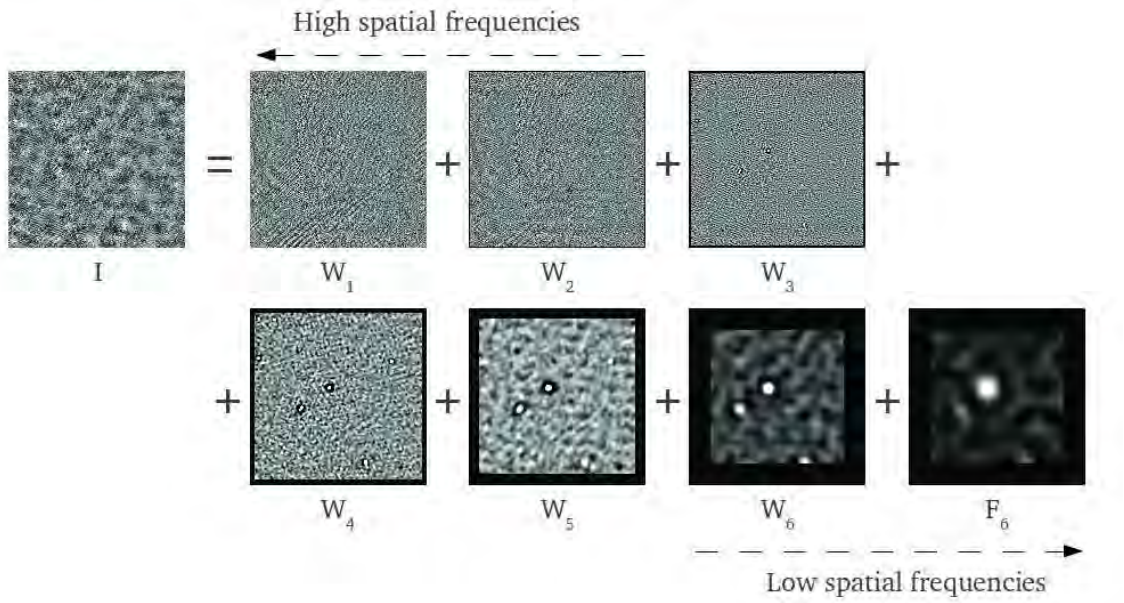

Figure 4.1: Decomposition of an image in 6 scales using the "à trous" algorithm and the filter h with contrast stretching applied for visualization purposes.

local thresholding, we call it the WALT algorithm. The steps for the WALT algorithm (shown schematically in Figure 4.2) are the following:

1. We use Gaussian fitting of the pixel intensity distribution in subsamples of the original image to calculate local noise and extract bright sources from the local threshold derived.

2. Two images are created: a "residual image" where bright sources have been substituted with local noise, and a binarized image with the bright sources, with pixels labelled with ones where the bright sources are located.

3. A wavelet decomposition is applied to the "residual image" using the "à trous" algorithm and a B_3-spline filtering function.

4. A local thresholding is applied to the first three scales.

5. A binary image from the addition of the binarized first three scales and the bright sources is created.

6. Finally, from this last image, connected zones and their centroids are calculated to produce the source positions catalogue.

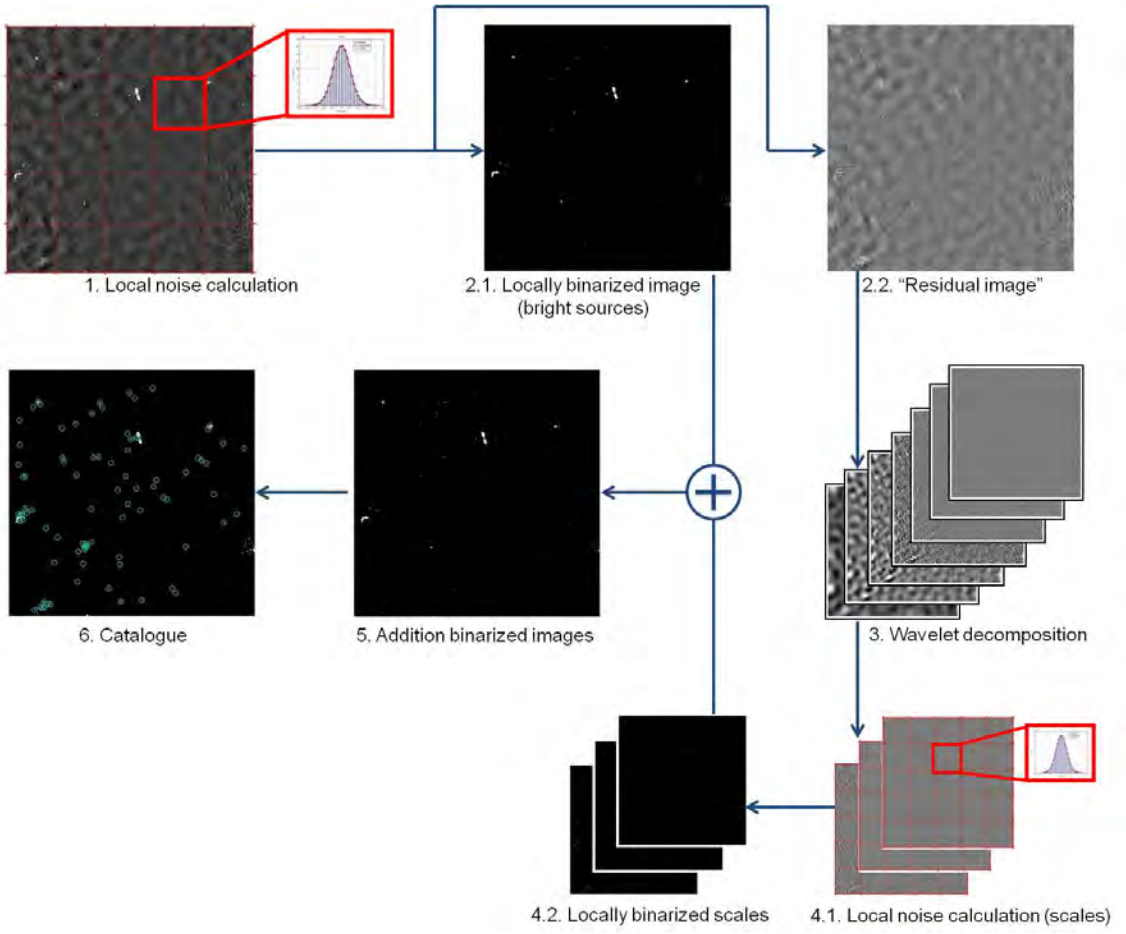

Figure 4.2: Graphical representation of the first algorithm (WALT): local thresholding based on a noise estimation is used to detect bright sources in the raw image and faint sources in the first three wavelet scales.

Notice that only the first three wavelet scales are used because these scales are where the point sources become most easily detected. In other cases, such as when there is interest in highlighting extended structures, the lower wavelet scales are more suitable.

In this algorithm a Gaussian fit to the histogram of intensities of the different subimages is carried out. The threshold of each subimage is set by selecting the intensity value where the Gaussian function has a specified height, actually, a fraction of the Gaussian peak height, and multiplying it by a confidence level. Therefore, three parameters need to be tuned: the number of subimages into which the raw image is divided, and the two parameters that model the Gaussian fitting corresponding to the fraction of the height of the Gaussian (hereafter g), and the arbitrary factor which determines the noise confidence level (hereafter k). Details on how to fix these parameters can be found in Section A.2 of Appendix A.

4.2 Slope stability of a radial contrast function

The fact that many sources have intensities very similar to the noise level complicates their detection and forces the use of very low thresholds. For this reason, our second proposed method includes the innovative idea of using the structural behaviour of the neighbourhood around each pixel studied. This structural analysis is performed by defining an intensity radial contrast function and analyzing the behaviour of its slope. Thus, all the sources can be better modelled, and lower thresholdings can be used, which leads to an increase in the rate of faint detections.

The defined radial contrast function relates the intensity of a pixel to the mean intensity of all its neighbours within a given radius. Through several different radial distances, it is possible to make a structural analysis of the pixel neighbourhoods, those with the most coherent patterns being the most likely to be sources. In other words, using the radial contrast function, we are able to locate sets of connected pixels with a central pixel that is brighter than their adjoining neighbours and, at the same time, these neighbours are brighter than their corresponding neighbours and so on until the last radius is analyzed.

4.2.1 Definition of the radial contrast function

For every pixel (i, j) in a studied region, we define a radial contrast function as:

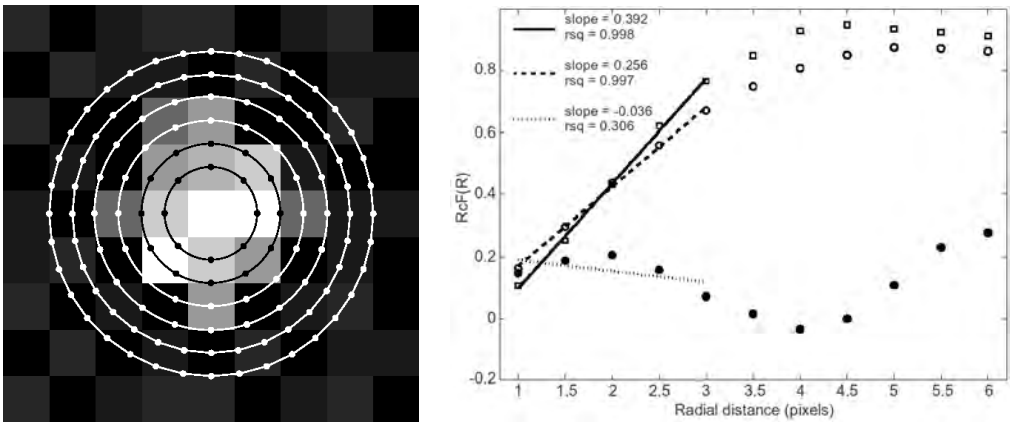

Figure 4.3: Graphical representation of the second algorithm (RCF). On the left, synthetic image of a source with 6 circles connecting neighbours at equal radial distances. On the right, behaviour of R_cF versus radial distance for two pixels belonging to real sources (open circles and squares) and a pixel belonging to a noise region (black circles).

$$R_cF(R) = \left(I(i,j) - \frac{\sum I(k,l)(R)}{N_{neigh}(R)} \right) / I(i,j), \tag{4.5}$$

where R denotes the radial distance from the neighbours (in pixels), (k,l) are the neighbour pixels within a radius R, and therefore k takes values from i - R to i + R and l takes values from j - R to j + R, and $N_{neigh}(R)$ is the number of neighbours within distance R.

As illustrated in the synthetic image shown in Figure 4.3 (left), if (i,j) corresponds to a pixel near the intensity peak of the source, then $R_cF(R_1) < R_cF(R_2) < R_cF(R_3) < ... < R_cF(R_n) \sim R_cF(R_n + 1) \sim R_cF(R_n + 2)$, otherwise $R_cF(R)$ will behave differently.

The behaviour of R_cF at each pixel can be characterized by its slope at low radius. In the case of the intensity in a Gaussian distribution, this slope is nearly constant. Therefore, we fit a first degree polynomial to R_cF versus radius, and we use its slope together with the goodness of the fit to detect compact sources. See the example in Figure 4.3 (right) where the different behaviours of the R_cF curves representing source pixels and background pixels are shown. Notice that source pixels present a monotonic increase before reaching a plateau, where pixels that are not near a local peak show either an initial decline or a fairly constant value.

4.2.2 Algorithm steps

To apply this approach based on a radial contrast function (hereafter RCF algorithm) to real images we use the following steps:

1. With the original image, local noise is calculated and a low local threshold is derived to select candidate areas (those with an area greater than the FWHM of the beam).
2. $R_cF(R)$ is calculated for all pixels in the original image up to N_r radius. A data cube of size (N_x, N_y, N_r) is created.
3. For every pixel (i, j) selected in step 1, a first degree polynomial is fit to $R_cF(R)$ and a slope and goodness of fit, given by the coefficient of determination rsq, which determines how accurately the regression line fits the data, is assigned to each pixel.
4. Groups of at least 4 connected pixels with associated R_cF fit slopes and rsq larger than certain threshold values are candidates to belong to a compact source.
5. Finally, connected zones and their centroids are computed to produce the source position catalogue.

This algorithm depends on a set of values that represents the range of radius used to create the radial contrast function, the slope (hereafter m) and the rsq. These parameters are further discussed in Section A.2 of Appendix A.

4.3 Boosting classification system

The previously presented approaches are unsupervised, which means that they do not need additional images to generate models of the sources to find. However, in most cases, supervised methods perform better since they are trained with meaningful information about their aim. Hence, our last algorithm is a supervised method based on the use of local features extracted from a bank of filters. These features provide descriptions of the different types of faint source structures. Our approach performs an initial training step in order to automatically learn and select the most salient features, which are then used in a boosting classifier [67] to perform the detection. This approach is based on the idea that a set of features, also known as words, can intuitively describe the sources to find, and building a model through the most characteristic features, known as dictionary, the sources will be more easily identified.

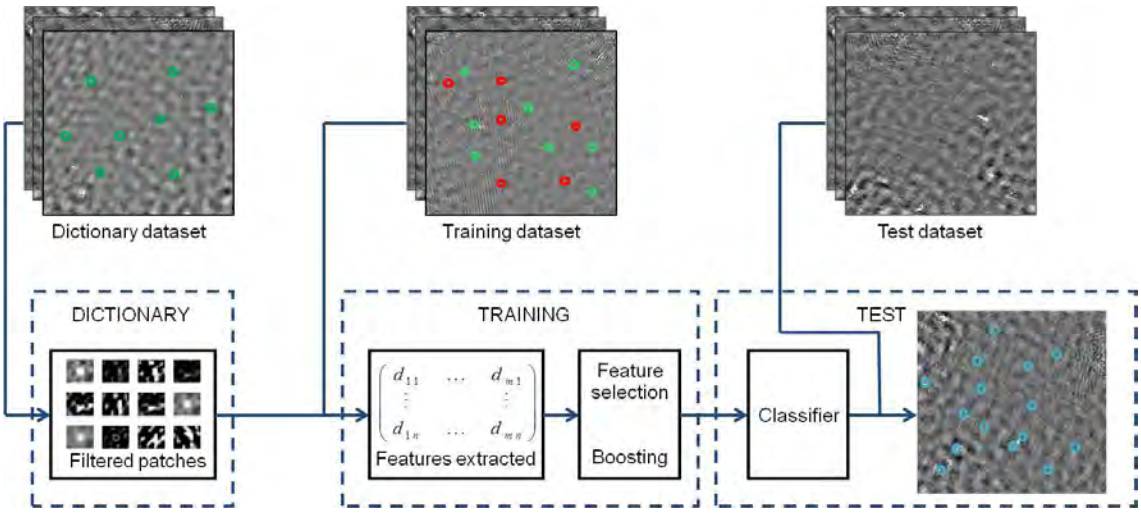

Figure 4.4: Graphical representation of the third algorithm (the boosting classifier): building the dictionary, training process and testing process with new images.

The proposed method is divided into three parts as shown in Figure 4.4. First, we build a feature dictionary composed of patches (a square subsample of the images with an arbitrary size) of faint sources. Afterwards, dictionary words are used to extract features and the system is trained using a boosting classifier algorithm.

4.3.1 Dictionary building process

A feature dictionary contains the visual words, in our case we use patches of pixels, that will be then used to extract features for training and testing. First of all, a random set of images is selected to be used to create the dictionary. Afterwards, these images are convolved with a bank of filters (see [67] for more details). All the filtered images are then used to extract different patches centred on the objects of interest (in our case, sources). Figure 4.5 shows the building vocabulary process. These patches become the words of our dictionary. Notice that, as well as the patch, the filter used is also needed to extract the image features, since each patch is convolved with the corresponding filtered image.

Once the dictionary has been built, the pixels of an image can be characterized by the following equation:

$$v(i,j) = (I(i,j) * f) \otimes p, \tag{4.6}$$

where v is the image with characterized pixels, I the original image, f the filter, and p

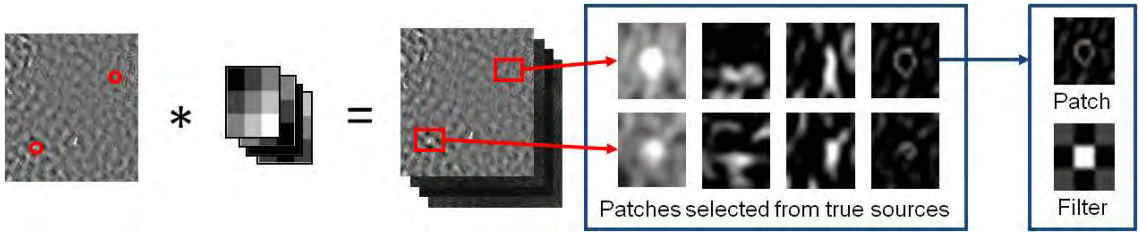

Figure 4.5: Dictionary building process.

the filtered patch. Therefore, the image is convolved ($*$) with the filter and then a cross correlation ($\otimes$) with the patch is performed. As a result, a probability image with high values in the regions similar to the patch is obtained.

4.3.2 Training and testing processes

The goal of the training process is to learn which features are the best to detect compact sources. The classifier has to be trained through the pixels of a set of images devoted to training, the class of these pixels (source or background in our case) being perfectly known. In our case, instead of using all the pixels in the training images, which will be computationally expensive, only a portion from each training image is selected. In particular, these points are the center of the sources (positive training samples) and some random locations of the background (negative training samples). Afterwards, a boosting classifier algorithm is applied. This type of algorithm is based on the simple idea that the sum of weak classifiers can produce a strong classifier [23]. In our case, the weak classifiers (c_w) are simple regression stumps, a tree-like structure with a single level, with a single feature, the most likely, the one with the least error, being selected in each round. The weak classifier function used is:

$$c_w(I(i,j)) = a(I(i,j) > th) + b, \tag{4.7}$$

where th is a threshold that determines if a pixel belongs to the object class or not, and a and b are parameters selected to minimize the classifier's error. After applying a weak classifier, those samples that are misclassified are given a higher weight while those correctly classified are given a lower weight. This process is repeated until convergence, all the samples correctly classified, or after a certain number of rounds. The final source classifier $C(x)$ is the sign of the result of the sum of weak classifiers.

Once the classifier is built it is applied to new images in the testing process in order to

perform the detection of compact sources. Note that a pixel-based classifier is also built and therefore, a probability image where high values mean a greater confidence of being a source is provided as a result. The images used to train the classifier are not used in the testing step.

4.3.3 Algorithm steps

Supervised approaches like this one need different sets of images including training and testing images. The boosting classifier algorithm steps are as follows:

1. Images of the dictionary dataset are filtered with the bank of filters, and patches are extracted where a given number of sources are located to build the dictionary.
2. Images of the training dataset are filtered with the bank of filters, and patches are extracted at the location of the sources (positive examples) and at randomly selected background regions (negative examples).
3. A boosting classifier is trained from positive and negative examples.
4. Pixels in the test dataset images are classified obtaining a probability image where a thesholding can be applied.
5. Finally, connected zones and their centroids are computed to produce the source position catalogue.

Two parameters are required in this algorithm. The first consists of a set of values corresponding to the sizes of the sides of the square patches to be extracted. The second, a threshold (hereafter th) applied to the final probability image. The parameters used in all the experiments are described in Section A.2 of Appendix A.

4.4 Test datasets

In order to analyze the performance of these three algorithms, both simulated and real data is used. The different datasets and catalogues are described below and the main features of each are summarized in Table 4.1. Column four indicates the FWHM of the point response function and columns seven, eight and nine depict the brightness ranges of the three groups into which the catalogues have been broken down according to the brightness of the sources (faint, mid-intensity and bright).

Table 4.1: Summary of the main features of the datasets and catalogues.

Image	Area (deg^2)	rms (mJy/beam)	FWHM ($''$)	Number of sources	Flux range (mJy/beam)	Faint sources (mJy/beam)	Mid-intensity sources (mJy/beam)	Bright sources (mJy/beam)
Simulations	0.56	0.01	5	500	[0.01, 200]	[0.01, 0.27]	[0.027, 6.78]	[7.79, 200]
		0.02			[0.02, 200]	[0.02, 0.42]	[0.44, 8.71]	[9.51, 200]
		0.04			[0.04, 200]	[0.04, 0.68]	[0.69, 9.59]	[12.04, 200]
GMRT	6.7	0.2	5	279	[1.65, 224.70]	[1.65, 8.46]	[8.61, 43.45]	[43.73, 224.70]
ATCA	1.2	0.012	6	1207	[0.06, 28.85]	[0.06, 0.44]	[0.45, 3.51]	[3.58, 28.85]

4.4.1 Simulated data

In order to perform controlled experiments, the astronomical community usually tests algorithms on simulated (synthetic) but realistic images. The position of the objects contained in real data is a priori unknown, and catalogues are built through manual inspection or automatic algorithms. Hence, although these catalogues are quite reliable, they are not ideal and may be biased and incomplete. The comparison of the results from applying the new methods to the simulated source catalogues can quantify the performance and possible biases in a systematic and objective way. It is possible to generate realistic simulations, including noise, of a radio aperture synthesis image for any sky model and observational setup, because the visibility data can usually be regarded as having independent Gaussian noise of a known variance. Sources with a wide range of flux intensities above and below the noise can be injected. The steps used to generate the simulations are the following:

1. A noise image based on Gaussian-randomized values is generated.
2. The noise image is convolved with a PSF consisting of a Gaussian profile of specified standard deviation.
3. The convolved noise image is normalized linearly to have a specified rms noise, a standard deviation of the noise.
4. A catalogue of a certain number of sources is randomly generated.
   - 4.1 The coordinates of the sources in the image are randomly generated avoiding blending (overlapping).
   - 4.2 The peak fluxes of the sources are randomly generated in a range comprised between the rms noise (lower limit) and a specified upper limit.
   - 4.3 The sizes of the sources are generated according to their flux.
5. Gaussian-shaped sources with corresponding coordinates, fluxes and sizes are created in an image.
6. The image with the sources is convolved with the PSF.
7. Sources are added to the noise image.

As stated by Offringa et al. [71], it is common knowledge that radio source fluxes behave like power-law (negative exponential) distributions with exponents around -2. Thus, the source peak fluxes are distributed as follows:

$$N(S) \propto S^{-2}, \tag{4.8}$$

where N is the number of sources and S is the flux. Using these flux densities, we have assumed a source size distribution as observed by Windhorst et al. [110]. They concluded that the median size of radio sources can be calculated as follows:

$$\theta_{med} = 2S^{0.3}. \tag{4.9}$$

Following this procedure, we have been able to create simulations with specific characteristics. In particular, we have simulated radio images of 2000×2000 pixels, with a pixel size of 1", a simulated PSF of the instrument (beam) of 5" with 500 sources ranging from the rms noise to 200 mJy. Three different images have been created with rms noise levels of 0.01, 0.02 and 0.04 mJy to be able to test images with different degrees of confusion between signal and noise. As can be seen in Figure 4.6, it is noticeable that, to the naked eye, more sources can be found in the image with 0.01 rms noise than with 0.04 rms noise.

4.4.2 GMRT observations

A deep radio image obtained by Paredes et al. [74] with the Giant Metrewave Radio Telescope (GMRT) is also used to analyze the performance of the three approaches presented. This image, which covers the TeV J2032+4130 field and is centred on an unidentified extended source called MGRO J2019+37 (a peak of gamma emission at the Cygnus region), is a mosaic made up of 19 circular multi-epoch observations (fields) at a frequency of 610 MHz. The whole mosaic covers more than 6 square degrees and has a size of 14000×14000 pixels.

As can be seen in Figure 4.7, we are dealing with a typical radio image with very bright sources, a large number of faint objects with intensities near to detection levels, as well as imaging artifacts. Regarding this image, despite its high noise level and interferences, some sources can be detected by the naked eye. However, some noisy regions, such as the edges of the external fields of the mosaic, may cause the methods to obtain unreliable detections. For this reason, we exclude some problematic regions (basically the outer regions of the mosaic and some other inner regions with a high component of noise and interferences) as can be seen in Figure 4.8.

We have taken the catalogue of Paredes et al. [74] as reference and used it to evaluate the completeness and reliability of the three methods previously discussed. It was created

Figure 4.6: Simulations of radio astronomical images with contrast stretching (98%) for visualisation purposes. From top to bottom rms noise levels of 0.01, 0.02 and 0.04 mJy.

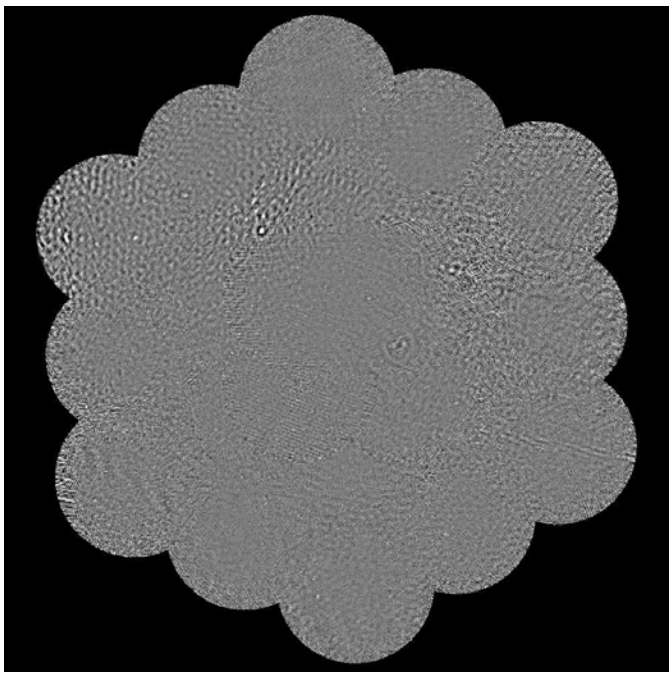

Figure 4.7: The GMRT mosaic with contrast stretching (98%) for visualisation purposes..

through a preliminary list of sources obtained with SExtractor and an extensive manual inspection. It covers all the radio sources present in the GMRT mosaic and contains the location of 362 sources as well as their photometric information. After discarding the sources in the exclusion regions, the final set of true sources in the catalogue consists of 279 sources.

4.4.3 ATCA observations of the Phoenix Deep field

In order to see the behaviour of the methods with other radio aperture synthesis images, we have also used data obtained by Hopkins et al. [41] with the Australia Telescope Compact Array (ATCA). Specifically, we have selected the 1.4 GHz mosaic from the Phoenix Deep Survey (PDS). It consists of a multiwavelength survey centred on the southern constellation Phoenix that covers 4.56 square degrees.

As shown in Figure 4.9, the ATCA image also shows a marked noisy interferometric background in which a crowded population of sources (over 2000) is present. Most of these sources are close to detection levels (faint), and therefore, this image is a challenging test for the methods. As the central part of the mosaic is the most sensitive and, therefore, presents a more homogeneous background, we have decided to use a reduced subimage

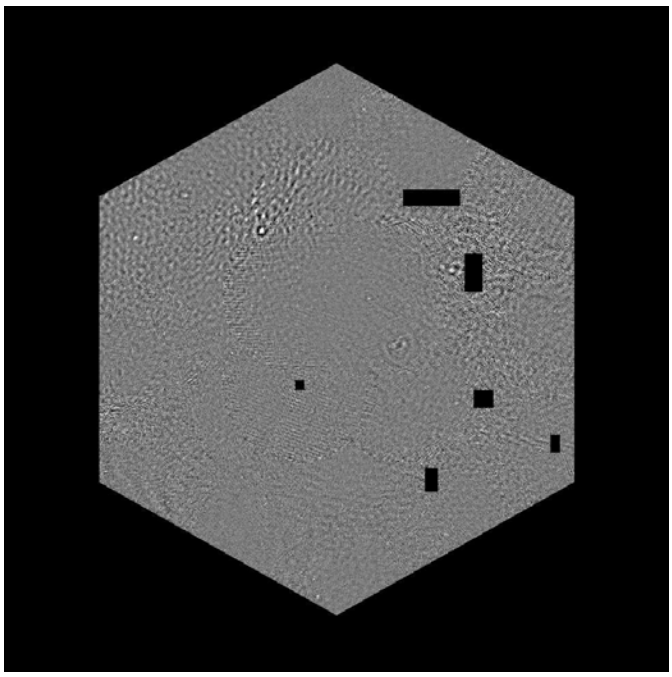

Figure 4.8: The GMRT mosaic with some problematic regions excluded with contrast stretching (98%) for visualisation purposes.

with a size of 2000×2000 pixels (see Figure 4.10).

To evaluate the quality of the detections in terms of reliability and completeness, we have used the catalogue produced in the PDS as reference. The original catalogue created with the Sfind algorithm [42] contains 2090 sources with their respective locations and photometric information. The final catalogue of the subimage selected consists of 1207 sources.

4.5 Experimental results

Each one of the three methods described earlier was applied to the test images obtaining respective lists of coordinates corresponding to the centroid of the detections found. Reference catalogues were used as the ground truth to compare the outcome of the detection methods to the true sources in the catalogues. In order to do this, we followed the procedure already mentioned in Section 3.2.3 which considers those detections and sources of the catalogue with a distance smaller than the FWHM of the synthesized beam to be correct matches.

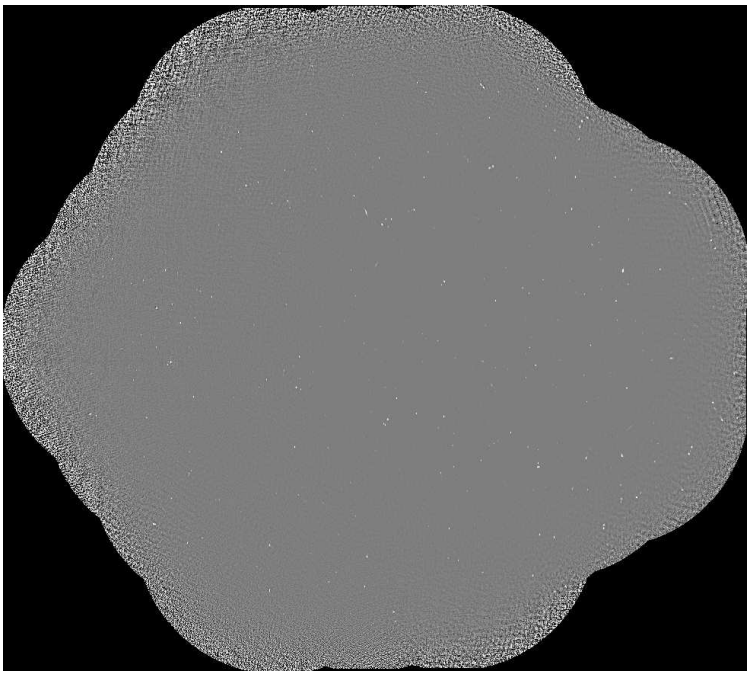

Figure 4.9: The ATCA mosaic with contrast stretching (98%) for visualisation purposes.

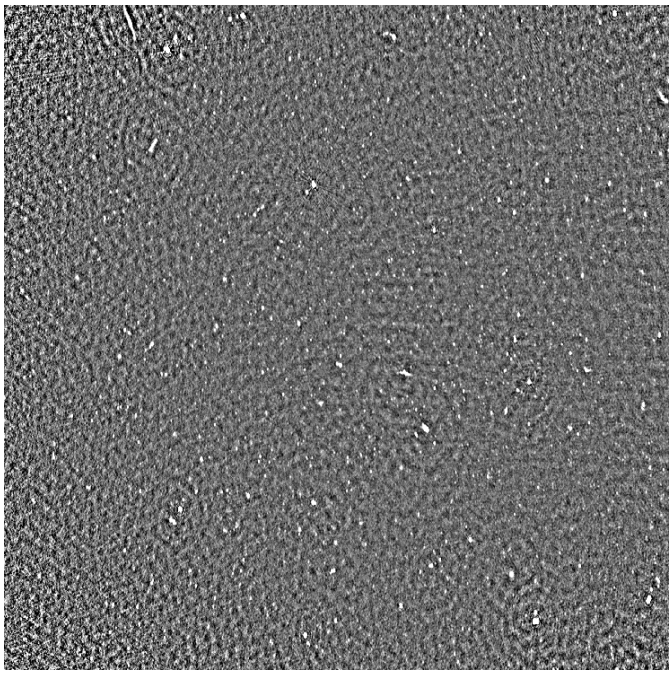

Figure 4.10: The ATCA subimage used with contrast stretching (98%) for visualisation purposes.

The methods' performances have also been analyzed in terms of their ability to detect sources of different intensities. In order to do this, we have grouped the sources in the catalogues according to their flux. Specifically, we have divided the sources' flux range into three bins corresponding to faint, mid-intensity and bright. Thus, we can discuss the methods' performance according to the number of faint or bright sources correctly identified. We include the SExtractor [6] and SAD (AIPS) [29] algorithms in the comparison because they are widely used in radio astronomy.

In order to ensure an optimal performance, a specific and precise parameter tuning for each method was necessary. For details on the values used, we refer to Section A.2 of Appendix A. We selected the appropriate values that provided certain levels of reliability (the fraction of detections corresponding to TP) and completeness (the fraction of sources in the catalogue correctly identified). In particular, we conducted two experiments in order to achieve a minimum of 90% and 95% of both percentages of TP (reliability) and true sources detected (TSD - completeness). This way, by fixing the percentage of TP, we can analyze the performance in terms of completeness, whereas by fixing the percentage of TSD, we can analyze the performance in terms of reliability as done in [42, 35].

The outcome of the application of the different methods to the synthetic dataset is shown in Tables 4.2 and 4.3. As expected, the lower the rms noise, the better the results. In general, in the three levels of noise, the new proposals presented similar percentages of TSD at high levels of reliability to the two reference algorithms. For instance, in the 0.02 rms image, WALT, RCF and the boosting classifier provided 85.00%, 85.40% and 82.80% TSD having fixed the TP rate to 95%, whereas SExtractor and SAD provided 85.00% and 85.40%. Furthermore, in terms of TP at high levels of completeness, the new methods tended to outperform the reference ones. WALT was the most reliable method with 0.02 and 0.04 rms levels while in the 0.01 rms image it shared this condition with the boosting classifier. For example, in the 0.02 rms image, with 95% completeness, WALT, RCF and the boosting classifier achieved 23.15%, 18.55% and 19.15% TP while SExtractor and SAD achieved 7.88% and 10.63%. WALT was the most reliable method closely followed by the boosting classifier. RCF was slightly less reliable than the other two proposals, but still fairly better than the reference methods. In the different levels of noise, all five methods were able to detect all the bright and mid-intensity sources, and missed similar percentages of faint sources. To extract more consistent conclusions, we also tested the methods on real data. A priori, their behaviour should be similar to the simulations.

A quantitative comparison of the results achieved with the three algorithms and the two

Table 4.2: Summary of the results obtained by the various methods with synthetic images, demanding a minimum of 90% TP (left) and TSD (right). In each row, from top to bottom, the results obtained in images with 0.01, 0.02 and 0.04 mJy rms noise.

Method	90% minimum reliability				90% minimum completeness			
	Detections	TP	TP (%)	TSD (%)	Detections	TP	TP (%)	TSD (%)
WALT	490	445	90.82	89.00	525	450	85.71	90.00
	478	433	90.59	86.60	824	450	54.61	90.00
	444	400	90.09	80.00	1591	452	28.41	90.40
RCF	495	446	90.10	89.20	558	450	80.65	90.00
	478	431	90.17	86.20	966	450	46.58	90.00
	406	390	90.34	78.60	2650	451	17.02	90.20
Boosting classifier	497	448	90.14	89.60	515	450	87.38	90.00
	465	419	90.10	83.80	890	450	50.56	90.00
	568	397	90.10	74.60	2466	450	18.25	90.00
SExtractor	490	442	90.20	88.40	598	451	76.57	90.20
	476	430	90.34	86.00	1000	450	45.00	90.00
	431	390	90.49	78.00	5367	450	8.38	90.00
SAD	496	447	90.12	89.40	582	452	77.66	90.40
	478	433	90.59	86.60	820	450	54.88	90.00
	441	390	90.48	79.80	5168	453	8.76	90.60

Table 4.3: Summary of the results obtained by the different methods with synthetic images, demanding a minimum of 95% TP (left) and TSD (right). In each row, from top to bottom, the results obtained in images with 0.01, 0.02 and 0.04 mJy rms noise.

Method	95% minimum reliability				95% minimum completeness			
	Detections	TP	TP (%)	TSD (%)	Detections	TP	TP (%)	TSD (%)
WALT	460	438	95.22	87.60	1041	475	45.63	95.00
	446	425	95.29	85.00	2056	476	23.15	95.20
	408	389	95.34	77.80	3051	476	15.60	95.20
RCF	467	444	95.07	88.80	2019	475	23.53	95.00
	449	427	95.10	85.40	2561	475	18.55	95.00
	399	386	95.35	78.00	4995	475	9.51	95.00
Boosting classifier	464	441	95.02	87.80	1165	476	40.86	95.20
	435	414	95.17	82.80	2481	475	19.15	95.00
	459	382	95.51	73.40	3637	475	13.06	95.00
SExtractor	461	438	95.01	87.60	5717	475	8.31	95.00
	446	425	95.29	85.00	6030	475	7.88	95.00
	403	383	95.04	76.60	12431	476	3.83	95.20
SAD	463	443	95.68	88.60	7597	476	6.27	95.20
	448	427	95.31	85.40	4469	475	10.63	95.00
	409	390	95.35	78.00	13229	475	3.59	95.00

Table 4.4: Summary of the results obtained by the different methods with the GMRT image, demanding a minimum of 90% TP (left) and TSD (right).

Method	90% minimum reliability				90% minimum completeness			
	Detections	TP	TP (%)	TSD (%)	Detections	TP	TP (%)	TSD (%)
WALT	264	239	90.53	85.66	292	252	86.30	90.32
RCF	262	236	90.08	84.59	319	252	79.00	90.32
Boosting classifier	252	228	90.12	81.72	310	252	81.29	90.32
SExtractor	252	227	90.08	81.36	333	252	75.68	90.32
SAD	240	216	90.00	77.42	405	252	62.22	90.32

Table 4.5: Summary of the results obtained by the different methods with the GMRT image, demanding a minimum of 95% TP (left) and TSD (right).

Method	95% minimum reliability				95% minimum completeness			
	Detections	TP	TP (%)	TSD (%)	Detections	TP	TP (%)	TSD (%)
WALT	214	202	95.28	72.40	368	266	72.28	95.34
RCF	237	226	95.36	81.00	448	266	59.38	95.34
Boosting classifier	201	192	95.52	68.82	357	266	74.51	95.34
SExtractor	229	219	95.63	78.49	459	266	57.95	95.34
SAD	214	204	95.33	73.12	489	266	54.40	95.34

reference ones (SExtractor and SAD) on the real datasets is shown in Tables 4.4, 4.5, 4.6 and 4.7. Figure 4.11 depicts the TSD percentages of the different methods broken down into three groups according to the source brightness, faint, mid-intensity and bright.

Regarding the results obtained in the GMRT dataset, we can see that the five methods provided a similar number of detections and good percentages of completeness in both levels with 90% and 95% reliability. Specifically, demanding 90% reliability, more than three quarters of the true sources were correctly identified in all cases. The most complete method was WALT with 85.66% TSD, closely followed by RCF with 84.59% TSD. The boosting classifier and SExtractor presented a similar completeness with both over 81% TSD. SAD was the least complete method in this level of reliability with 77.42% TSD. The method that detected the most faint sources was WALT, with 77.46%. The other methods, except for SExtractor, detected more than two thirds of the faint sources, although SExtractor compensated for that low percentage by being the only method to detect 100% of the mid-intensity and bright sources. On the other hand, demanding 95% reliability,

Table 4.6: Summary of the results obtained by the different methods with the ATCA image, demanding a minimum of 90% TP (left) and TSD (right).

Method	90% minimum reliability				90% minimum completeness			
	Detections	TP	TP (%)	TSD (%)	Detections	TP	TP (%)	TSD (%)
WALT	1080	975	90.28	80.78	1324	1089	82.25	90.22
RCF	1027	925	90.07	76.64	1406	1088	77.38	90.14
Boosting classifier	1100	990	90.00	82.02	1386	1087	78.43	90.06
SExtractor	628	568	90.45	47.06	2126	1088	51.18	90.14
SAD	457	412	90.15	34.13	2920	1090	37.33	90.31

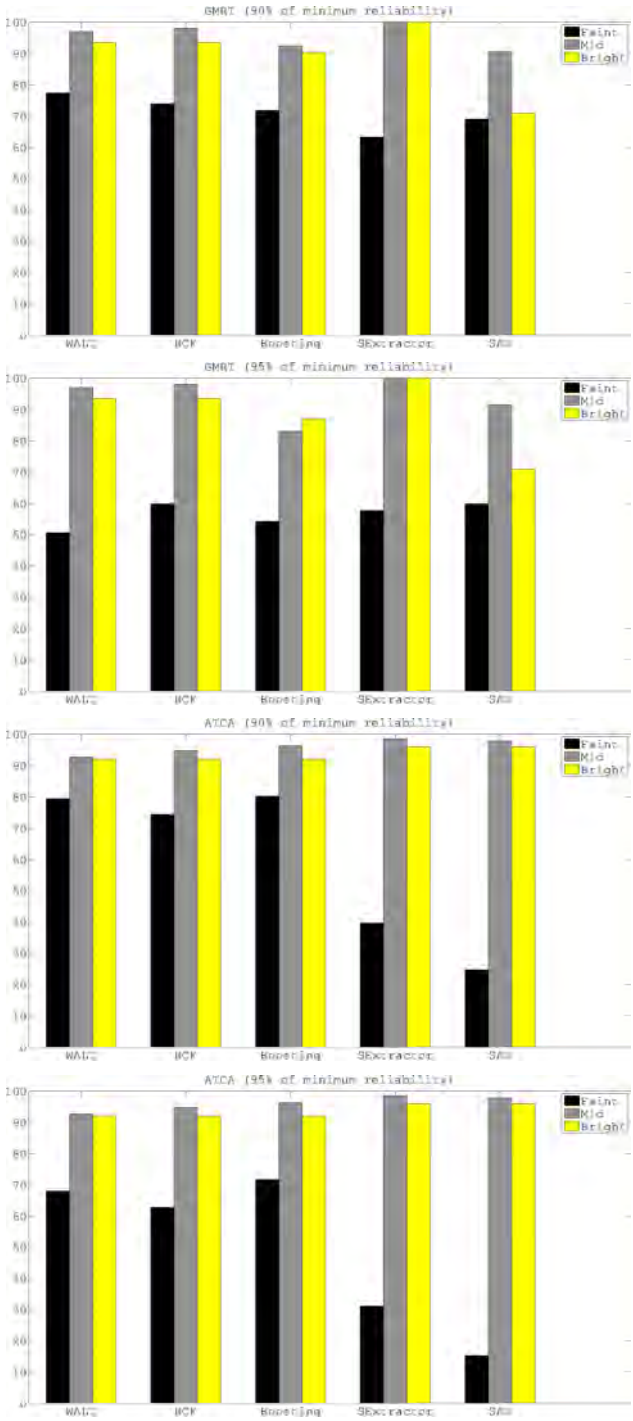

Figure 4.11: Graphical representation of the percentages of TSD obtained with the GMRT and ATCA datasets according to the brightness of the sources.

Table 4.7: Summary of the results obtained by the different methods with the ATCA image, demanding a minimum of 95% TP (left) and TSD (right).

Method	95% minimum reliability				95% minimum completeness			
	Detections	TP	TP (%)	TSD (%)	Detections	TP	TP (%)	TSD (%)
WALT	898	855	95.21	70.84	1989	1147	57.67	95.03
RCF	846	805	95.15	66.69	1654	1147	69.35	95.03
Boosting classifier	948	901	95.04	74.65	1684	1147	68.11	95.03
SExtractor	502	477	95.02	39.52	2699	1149	42.57	95.19
SAD	352	335	95.17	27.75	3492	1151	32.96	95.36

more than two thirds of the catalogue sources were correctly detected by all the methods. In this case, RCF was the best method by far with 81.00% TSD. SExtractor also kept a good completeness level with 78.49% TSD rate. The other three methods detected a lower number of true sources, the boosting classifier being the least complete with less than 70% TSD. That is due to that, in addition to the expected number of faint sources missed by all the methods, the boosting classifier also missed some mid-intensity and bright sources. All the methods detected between 50% and 60% of the faint sources, RCF and SExtractor being the best methods in that sense with 59.86% of the faint sources detected.

In a different way, the five methods presented a different number of detections with differences greater than 100 objects when demanding certain levels of completeness. With a completeness level of 90%, all the methods achieved more than 75% TP except for SAD (62.22%). The most reliable method was WALT (86.30% TP). With a completeness of 95%, the most reliable methods were the boosting classifier and WALT (74.51% and 72.28%). The rest of the methods obtained less than 60% TP. SAD was the least reliable in both levels of completeness probably due to the fact that, unlike the other methods, it was not able to find a high percentage of bright sources.

Concerning the results achieved with the ATCA image, we quickly noticed that, in general, both TP and TSD percentages were lower than those achieved with the GMRT image. As mentioned, the ATCA image is very crowded and presents a great number of faint sources difficult to find by the detection methods. The number of detections provided by the methods may be very different, to the point that some methods detected more than double the number of objects as others. In terms of completeness, the boosting classifier stood out in both 90% and 95% levels of reliability; 82.01% in the first case and 74.65% in the second case. WALT was the second most complete method with 80.78% and 70.84% for 90% and 95% reliability, and we found RCF's 76.64% and 66.69% for 90% and 95% reliability good percentages. On the other hand, SExtractor and specially SAD offered percentages of TSD substantially lower than the new algorithms. SExtractor achieved 47.06% and 39.52% TSD (90% and 95% reliability), while SAD achieved 34.13%

and 27.75% (90% and 95% reliability). This is due to the poor percentages of faint sources detected by these two methods. While the three new algorithms were able to detect more than 70% of the faint sources with a reliability of 90% and more than 60% with a reliability of 95%, the two reference methods detected less than 40% (SExtractor) and less than 25% (SAD) of the true sources with a 90% reliability. With a 95% reliability the results were even lower. The best methods for detecting faint sources were the boosting classifier and WALT with percentages around 80% with 90% reliability and 70% with 95% reliability. It should be pointed out that all the methods presented percentages of mid-intensity and bright sources detected above 90%.

Similarly, with respect to the reliability of the methods with the ATCA dataset, the three new algorithms gave a better performance than the reference ones in terms of reliability. With a completeness level of 90%, WALT was the most reliable method with 82.25% TP, followed by the boosting classifier and RCF with 78.43% and 77.38%. SExtractor and SAD obtained 51.18% and 37.33% TP. Similar behaviours were found with a completeness level of 95%. In this case, the most outstanding methods were RCF and the boosting classifier with more than two thirds of the detections corresponding to true sources (69.35% and 68.11% TP). WALT provided 57.67% TP, whereas SExtractor and SAD provided a great number of spurious detections with 42.57% and 32.96% TP.

Figures 4.12, 4.13, 4.14, 4.15, 4.16 and 4.17 show some qualitative results at 95% reliability and completeness. In the 0.02 rms simulated image we can see that in a high reliability regime the number of TP and FP was similar for all five methods. In a high completeness regime all the methods presented a significant number of FP. However, this number was much greater with SExtractor and SAD than with the new proposals. With the GMRT image, demanding 95% reliability, we can see that the reference algorithms presented a greater number of FP around a very noisy and inhomogeneous region on the right of the image although this region was partially excluded. The new methods presented their FP more spread throughout the whole image and dealt better with this noisy region. That fact was asserted in the 95% completeness results where reference methods had a cluster of FP around this region. Even though RCF and, to a lesser degree, the boosting classifier also clustered FP around this region, they were substantially fewer. In contrast, WALT was not affected at all by this problem. In the case of the ATCA image, more TP were provided by the new methods than the reference ones in the 95% reliability regime. Furthermore, in the SExtractor results, a greater number of FP appeared in the top- and bottom-left regions characterized by having more noise and background variations. That fact is dramatically emphasized in the 95% completeness results, where both SExtractor

and SAD presented a huge number of FP in the left hand region of the image. In contrast, the new algorithms did not present this problem or at least they did it in a smaller way. The low number of FP provided by RCF is very noticeable.

4.6 Discussion

We conclude from the analysis of the results that the three new algorithms perform well with both synthetic and real datasets. They obtain similar and even better percentages of true positives than SExtractor and SAD, a much smaller number of FP, and were able to correctly identify more sources. Furthermore, they deal with the most noisy regions in a better way. The main point illustrated by the simulations is that the new methods are more reliable than the state-of-the art methods, and more specific conclusions have been drawn from real datasets.

The boosting classifier is the most complete method when dealing with the crowded ATCA image. This fact clearly demonstrates the good performance of this method with images with a high density of sources. Its completeness with the GMRT dataset is also acceptable as it is close to the outstanding percentages. Concerning reliability, the boosting classifier presents remarkable TP percentages demanding 90% completeness and acceptable TP percentages demanding 95% completeness. For all these reasons, we consider the boosting classifier to be the method that, in general, performs better. It must be borne in mind, however, that it is a supervised method that needs a set of training images to work. In fact, this is, at the same time, its main strength and weakness because, on the one hand, the general performance of this method is high, but on the other, the need of an initial ground truth for training requires a more demanding tuning and more computational time. Hence, we believe that this algorithm is very useful when dealing with a great amount of data of the same nature because by simply devoting a little time to manually identifying some positive (sources) and negative (background) examples in a small sample of the dataset the rest of the detections can be carried out automatically with great accuracy. With the ATCA dataset, the boosting classifier has been the method with more faint sources detected with 80.21% and 71.70% with reliability levels of 90% and 95%. This proves that the number and selection of positive and negative samples for the dictionary building and training steps were appropriate.

Nevertheless, a portion of the dataset to be used for training is not always available, and in these cases, WALT and RCF may be good choices. They present an important

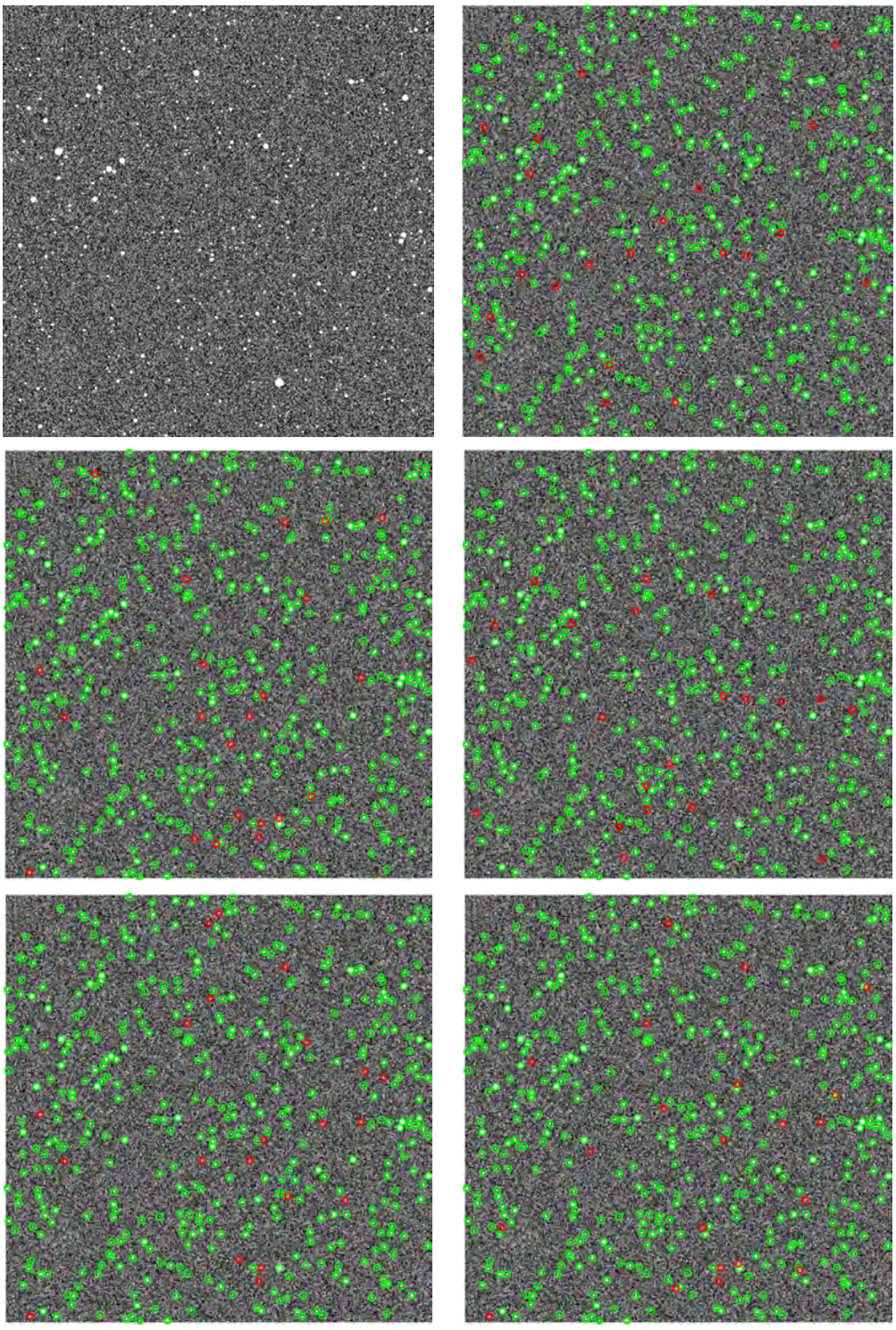

Figure 4.12: Qualitative results obtained in the 0.02 rms simulated image with 95% reliability. From top to bottom and left to right: the raw image, the detections obtained with WALT, RCF, the boosting classifier, SExtractor, and SAD. Green circles indicate TP while red circles indicate FP.

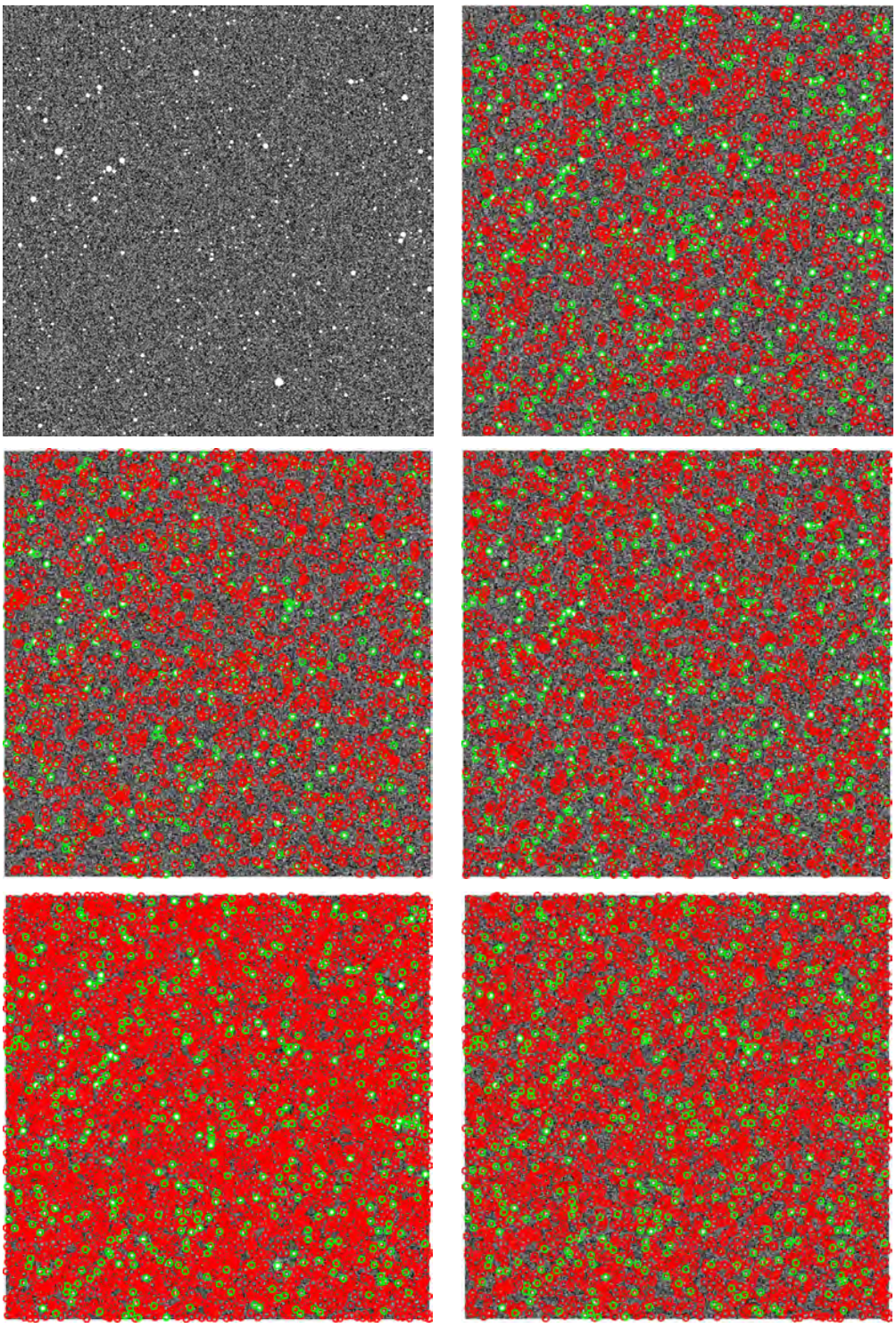

Figure 4.13: Qualitative results obtained in the 0.02 rms simulated image with 95% completeness. From top to bottom and left to right: the raw image, the detections obtained with WALT, RCF, the boosting classifier, SExtractor, and SAD. Green circles indicate TP while red circles indicate FP.

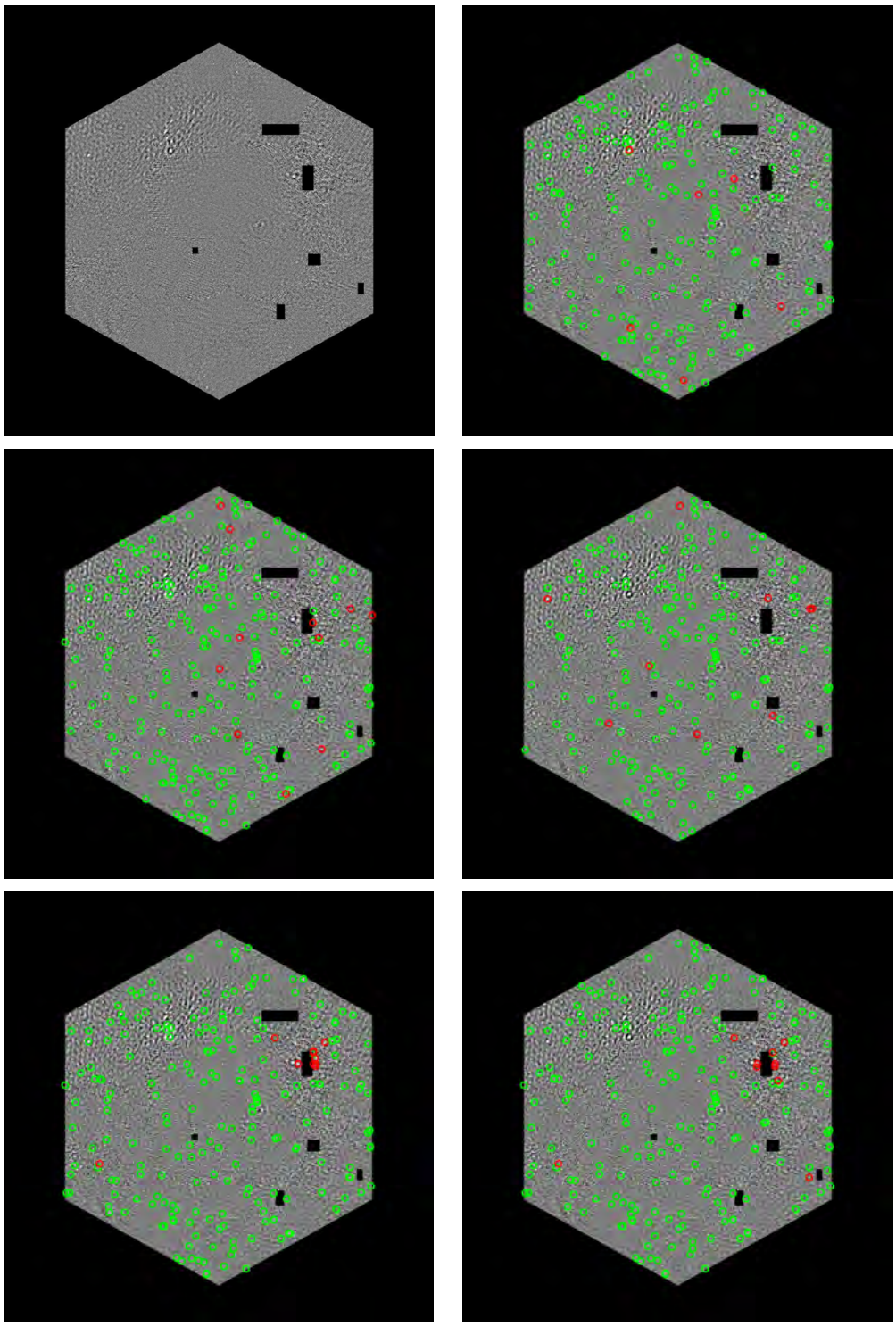

Figure 4.14: Qualitative results obtained in the GMRT image with 95% reliability. From top to bottom and left to right: the raw image, the detections obtained with WALT, RCF, the boosting classifier, SExtractor, and SAD. Green circles indicate TP while red circles indicate FP.

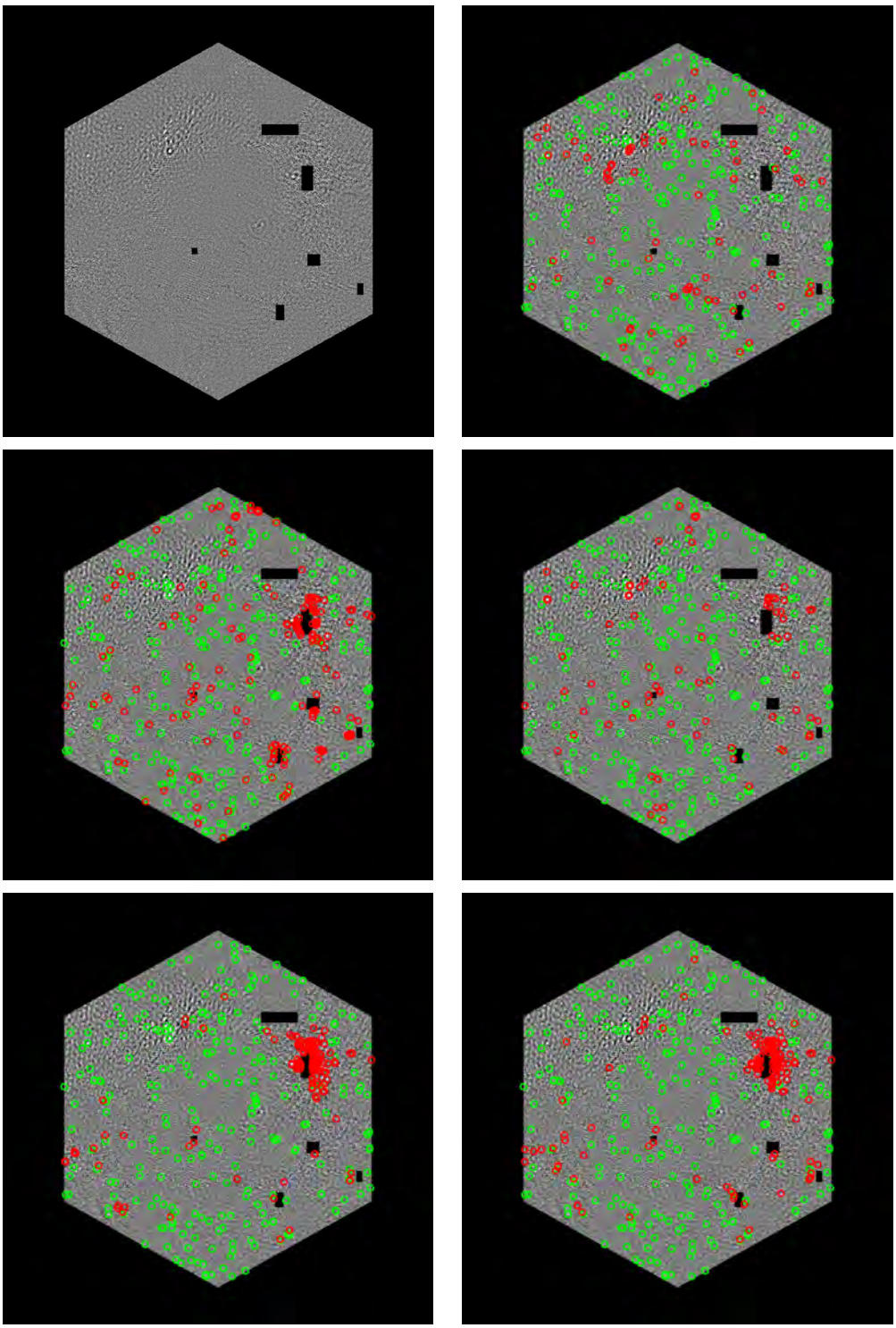

Figure 4.15: Qualitative results obtained in the GMRT image with 95% completeness. From top to bottom and left to right: the raw image, the detections obtained with WALT, RCF, the boosting classifier, SExtractor, and SAD. Green circles indicate TP while red circles indicate FP.

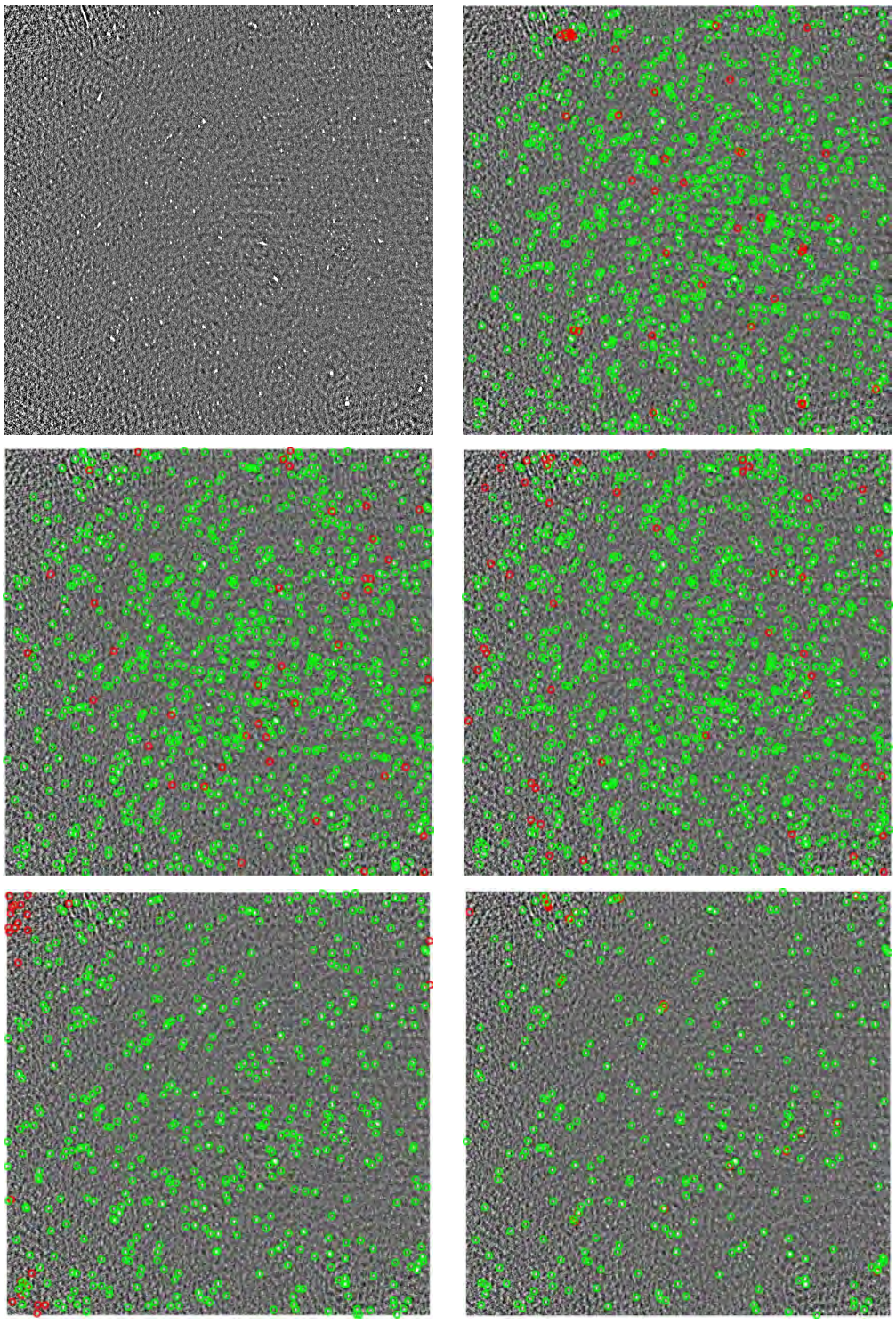

Figure 4.16: Qualitative results obtained in the ATCA image with 95% reliability. From top to bottom and left to right: the raw image, the detections obtained with WALT, RCF, the boosting classifier, SExtractor, and SAD. Green circles indicate TP while red circles indicate FP.

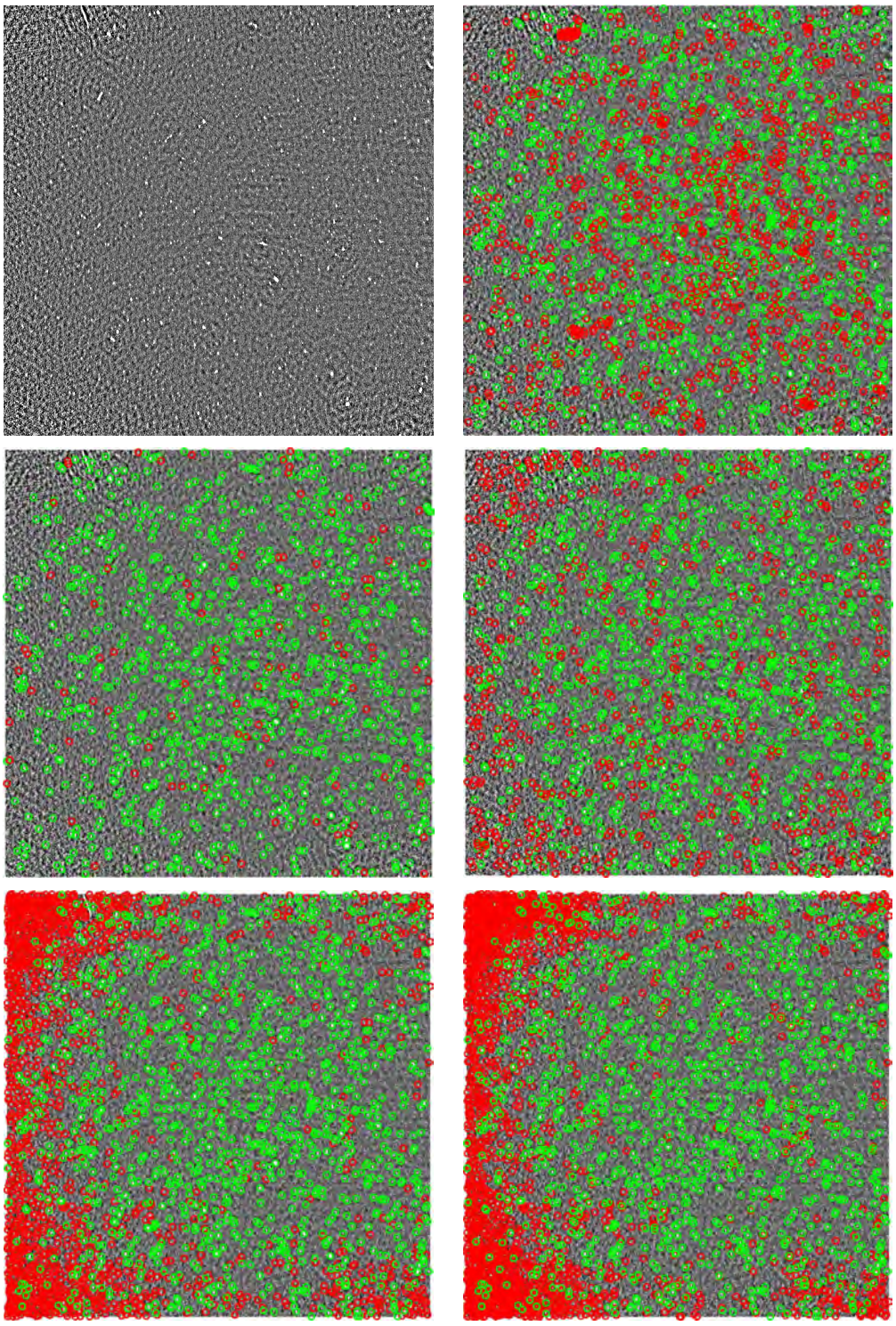

Figure 4.17: Qualitative results obtained in the ATCA image with the new and the reference methods with 95% completeness. From top to bottom and left to right: the raw image, the detections obtained with WALT, RCF, the boosting classifier, SExtractor, and SAD. Green circles indicate TP while red circles indicate FP.

advantage: their parameter setting is simpler than the boosting classifier. They have shown very high performances with the GMRT, specially in terms of completeness. The fact that the distribution of sources in the GMRT image is sparser, and, therefore, overlaps less frequently, has facilitated the thresholding of the sources in WALT and allowed an appropriate contrast radial analysis around the peaks in RCF. Consequently, the number of true sources detected is higher than with the other methods. WALT also achieved a high reliability, probably due to the multiscale component of the approach that has attenuated disruptive effects such as background variabilities or high levels of noise that may provoke spurious detections. Even though WALT has been the method with the best percentage of faint sources detected with a reliability of 90%, in general, RCF has been the method that has performed better at detecting faint sources in the GMRT dataset with 73.94% and 59.86% of them with reliability levels of 90% and 95%. Moreover, as the difference between the rms and the flux of the faintest sources is greater in the GMRT image, thus making the detection range greater, algorithms such as WALT and RCF, which apply thresholding techniques to the raw data, can obtain better results.

4.7 Conclusions

Three novel approaches for the detection of faint sources in wide field radio interferometric images have been proposed. They are based on very different strategies: the first, WALT, on local thresholding in different wavelet scales; the second, RCF, on the pixel spatial coherence described by a radial contrast function; and the third, the boosting classifier, on the extraction of local features and their classification. The application of these algorithms to realistic simulations and real radio images and a posterior comparison of the detections obtained to reference source detection software such as SExtractor and SAD has demonstrated their good performance. For all three algorithms, a quantitative evaluation of the detections performed has pointed out that the percentage of detections corresponding to true sources has been similar and even better than with the reference methods and the number of detected sources in the catalogue has been significantly better than more widely used algorithms. The new methods also present remarkably fewer numbers of false detections, which allows a greater number of true sources detected at high regimes of reliability.

The main strength of these methods is their ability to detect faint sources. Whilst no one method was the best in all test cases, each method is able to outperform the reference algorithms in specific situations. For images with a high density of sources, the boosting

classifier will give the best results both in completeness and reliability. For images with complex background structures, WALT is able to reliably detect sources whilst rejecting noise, and the RCF algorithm is able to extract sources close to the noise level.

Chapter 5

Multiscale Distilled Sensing: source detection for long wavelength images

As shown in Chapter 2, several source detection methods based on different techniques have been developed over the last years. Of special interest is the method called Distilled Sensing (DS) proposed by Haupt et al. (2009) [35] to detect sparse signal in noisy observations. It deals with the detection problem from a different point of view. The strength of DS lies in the idea that it is easier to identify where the signal is absent than where it is present. In other words, it consists of discarding those regions where the signal (sources in the case of astronomical images) is unlikely to be present, and focuses the detection on the remaining regions. This method has proven to work satisfactorily with optical astronomical images as depicted in the quantitative evaluation presented in Chapter 3. However, like many other methods, its performance decreases when images have a complex background with a high level of noise and marked intensity variations. This is the case with images acquired at long wavelengths such as radio and infrared, where an additional image transformation step may be needed to attenuate these harmful effects. Although it presents good percentages of reliability in all bands, its completeness decreases with these types of images.

Aiming to improve the source detection in high wavelength images, specially in terms of completeness, in this chapter we present a proposal based on the combined use of DS with multiscale techniques that are widely applied to astronomical imaging for noise filtering and source highlighting purposes. Unlike the methods proposed in Chapter 4, specially developed to detect faint sources, the application of Distilled Sensing in multiscale space expects an improvement in sources of different brightnesses, and not only in fainter ones.

5.1 Distilled Sensing

Distilled Sensing is an adaptive sampling method for the detection and estimation of sparse signal. These kinds of methods are also known as compressed/sparse signal/sensing and basically recover (i.e. estimate or detect) signal in sparse observations. DS is based on the main principle that in a noisy observation, it is far simpler to identify larger sets of non-singal than smaller sets of signal. It can be seen as an image transformation step where, through different iterations, the data is refined. More resources are iteratively focused on those regions that are more likely to be signal while at the same time ignoring those regions unlikely to be of interest. Hence the name of the method, since this procedure is similar to the purification by distillation performed in chemistry. In this way, the increasing level of certainty of where the sources are located increases along iterations. In the astronomical image domain, this procedure is equivalent to discarding background/noise regions and only taking the sources into account.

Figure 5.1 illustrates a simple example of how DS works. In the raw image, negative components are discarded since they are considered as noise. Afterwards, an iterative process is applied in which the data is refined and noise components are excluded. Notice that after the refinement step, the values of the components slightly change and new negative components arise. A certain amount of energy sensing (a predefined value) is distributed into the iteration steps, and at the same time, this part of the energy is equally distributed into the different interest regions in the image, being all the pixels in the first iteration. A larger value of energy sensing is devoted to the first iterations and decreases exponentially in the later iterations when there are fewer remaining interest regions, finally using the remaining resources in the last iteration. The following formula is a formal representation of this energy sensing allocation among the iterations:

$$R_k = \begin{cases} \epsilon^{k-1} R_1 & j = 2, ..., m-1 \\ R_1 & k = m, \end{cases} \tag{5.1}$$

where R_k is the energy sensing allocated to the iteration k, ϵ is an arbitrary parameter to model the relationship between the energy allocated to an iteration and that of the previous iteration (with $0 < \epsilon < 1$), and m the total number of iterations fixed to:

$$m = \max\{\log_2 \log n, 0\} + 2, \tag{5.2}$$

where n is the total number of components of the observation (pixels in our case).

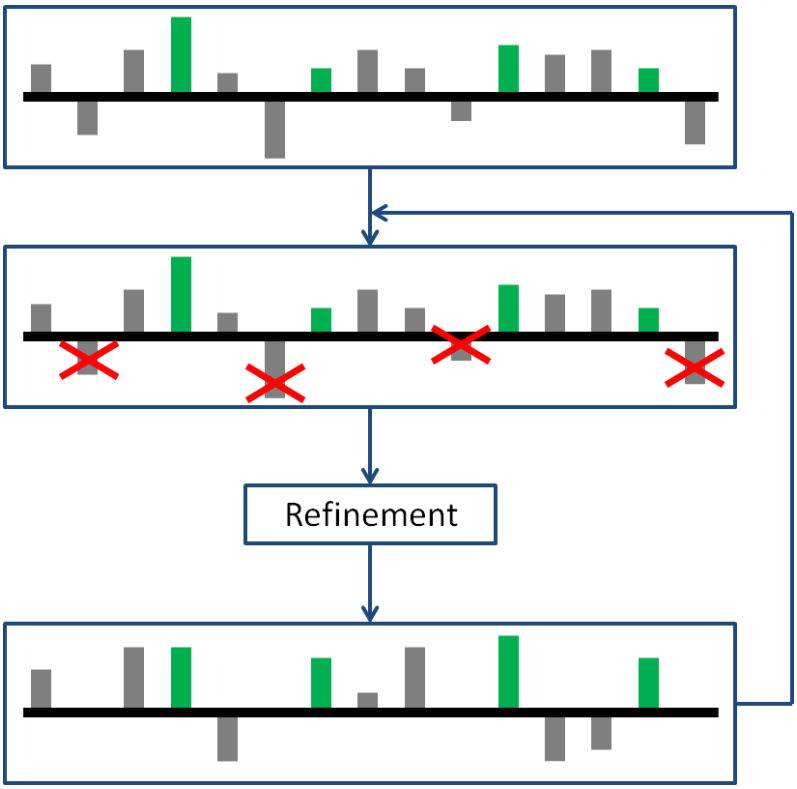

Figure 5.1: Graphical representation of the DS method. Green bars represent true signal components while grey bars represent noise.

As can be seen, the energy of the initial and final iterations is the same because, according to the authors, that benefits the control of the false positives in the first iteration and the false negatives in the last one [35]. The authors also suggest that $\sum_{k=1}^{m} R_k \leq n$. The data is iteratively refined using a function where some uncertainty, a random value drawn from a normal distribution, is added to each interest pixel, and the resulting sum is divided into the square root of the energy sensing value corresponding to the pixel [35]. The formal representation of this refinement or distillation in an iteration follows:

$$Y_k(i,j) = \begin{cases} (I(i,j) + Z)\sqrt{\frac{R_k}{|S_k|}} & I(i,j) \in S_k \\ Z & I(i,j) \notin S_k, \end{cases} \tag{5.3}$$

where Y_k is the refined image in iteration k, $I(i,j)$ is the intensity of the pixel in row i and column j, $Z \sim \mathcal{N}(0,1)$, and S_k is the set of pixels of interest of iteration k. This equation leads to negative values considered as noise, so they are discarded. Afterwards, the interest regions are limited to those with positive values, and the entire process is repeated. As a result of this process, most of the background pixels are discarded. The authors stated that in each distillation iteration, most of the pixels corresponding to signal were retained, whereas approximately half of the background/noise pixels were ruled out. Finally, the source locations are specified by using a data-based thresholding. In Haupt et al. [35], the authors used a threshold that guarantees a detection reliability of 95%, meaning that at least 95% of the detections performed by the method were true sources.

5.2 DS in multiscale space

In order to turn DS into a more robust method able to deal with images with more complex backgrounds, we decided to apply it after a multiscale transform of the original data. These kinds of techniques decompose images into components at different scales or frequencies, and depending on the type of source, they become highlighted in the low or high scales. Thus, every single scale can be treated as an image where the sources have to be detected. As can be seen in Chapter 2, these types of techniques are widely used in astronomical images since, apart from highlighting sources, they are good at filtering noise, removing background, attenuating the background variability and deblending sources. Therefore, by using a multiscale transform the background will have a lesser impact and the detection results should improve.

Different multiscale decompositions have been used in the literature, the wavelet trans-

form (WT) and its variations being the most used by far due to their performance [17, 87, 21, 104, 26]. In this work, we have selected the two types of WT most commonly used:

- The stationary wavelet transform (SWT), more commonly known as the 'à trous' algorithm, which is an extension of the discrete WT designed to overcome the lack of shift invariance [91]. Each scale is defined as the difference between the previous scale and the previous scale convolved with a specific discrete filter. We have used a spline of degree 3 as a filter, as suggested in [91]. More information about this transform can be found in Sections 2.1.4 and 4.1.
- The Mexican hat wavelet transform (MHWT), a special case of the family of continuous wavelets consisting of applying a Laplacian operator to a Gaussian function [91].

When these transformations have been done, we then apply the DS algorithm to provide the source detections. We decided to analyze the first three scales in the SWT since most of the sources to be found were point-like and, as stated in Chapter 2, the most suitable scales in which to find these types of sources are those with higher spatial frequencies (the first ones). On the other hand, we only used the first scale of the MHWT since further scales of this transform are not commonly used in the literature. Afterwards, we applied the DS method to each of the four resulting scales: the three scales in the SWT and the first scale in the MHWT. We call this procedure Multiscale Distilled Sensing (MDS).

5.2.1 Algorithm steps

MDS is based on the following steps:

1. A wavelet transform is applied to the raw image and a significant scale is selected.
2. A certain value, energy sensing, is distributed into a certain number of iterations.
3. In the wavelet scale, the proportional energy sensing is distributed in the regions of interest (the whole image in the first iteration).
4. Pixels in the region of interest are refined:
   4.1 Some uncertainty is added to each interest pixel intensity.

4.2 The resulting sum is divided into the square root of the energy sensing value corresponding to the pixel.

5. Pixels with negative values are excluded from the regions of interest.

6. Steps 3 to 5 are repeated until the specified number of iterations is reached.

7. Finally, connected zones and their centroids are computed to produce the source position catalogue.

The final step is based on a thresholding, and therefore, this cut-off value must be experimentally tuned to achieve the best possible results.

5.3 Experimental results

In order to verify the performance of our approach, we have chosen the images from two public surveys introduced in the quantitative analysis of Chapter 3: the WISE infrared dataset and the CGPS radio dataset, both described in Section 3.2.1. These datasets present a variable noisy background in which we can find both point (most of them) and extended sources over a noisy background with perceptible intensity variations. The evaluation was carried out through the refined catalogues associated with these images (see Section 3.2.2) and following the evaluation strategy used throughout this thesis (see Section 2.3.1) which results in true positives (TP) and true sources detected (TSD) percentages. As mentioned in Section 3.2.1, some regions of the $WISE_{12}$, $CGPS_{21}$ and $CGPS_{74}$ containing extended emissions were excluded.

DS is a thresholding-based method and, as such, it can provide different detections according to the threshold used. An appropriate value must be selected in order to guarantee a suitable compromise between reliability and completeness. We followed the same criterion as with the original DS proposal [35], and found the threshold that provided a certain specified reliability (e.g. Haupt et al. demanded a minimum of 95%). In particular, we conducted two experiments in order to achieve a minimum of 90% and 95% reliability. In other words, the demand was at least 90% and 95% TP (i.e. a maximum of 10% and 5% FP). Therefore, by fixing the TP rate, we could compare the results obtained with DS in the different scales by means of the percentage of true sources correctly detected (completeness). The parameter setting used can be consulted in Section A.3 of Appendix A. In addition, in order to significantly evaluate the power of our proposal, we also applied the well-known SExtractor source detection algorithm [6] to the images.

Tables 5.1 and 5.2 show the different results achieved by directly applying DS and SExtractor to the raw images and by applying MDS. Notice that the MHWT results in the $WISE_{12}$ image, expecting 95% TP, are missing because it was not possible to achieve such a reliability with such a challenging image. It reached at 91.45% best. The vast majority of results obtained using MDS were considerably better than using DS alone. In some scales, the number of true sources detected rose significantly. For instance, in the SWT_1 scale of the $WISE_{4.6}$ image, the percentage of true sources identified increased from 24.47% to 84.36% with a reliability of 95% and from 50.56% to 87.66% with a reliability of 90%. In a similar way, in the SWT_3 scale of the $CGPS_{74}$ image, DS was able to find 60.96% and 68.45% with 95% and 90% reliability respectively of the catalogue sources, whereas DS applied directly to these images was able to find 18.89% and 29.41% with 95% and 90% reliability respectively of the catalogue sources. Figures 5.2, 5.3, 5.4, 5.5 and 5.6 depict the qualitative results achieved in all the images tested with 95% reliability. In them we can see the dramatic improvement in terms of true sources of the catalogue correctly detected. For instance, there were almost 60% more correct detections in the $WISE_{4.6}$ infrared image and more than 40% more in the $CGPS_{74}$ radio one. These increases are due mainly to the greater number of fainter sources detected thanks to the use of a multiscale transform. Furthermore, DS by itself considered blended or very close sources as unique objects as can be seen in the images, a point that was solved with MDS.

Referring to infrared images, the best results were achieved in the first two SWT scales, with fewer values in the third and the MHWT scales. On the other hand, in radio images the results were more similar in all the scales. Moreover, concerning the performance of DS in multiscale space, we noticed that in most cases the rate of true sources detected was similar or even better than when applying SExtractor to the raw images, especially in infrared images. The only case in which SExtractor was slightly better was with the $CGPS_{21}$ image. For the rest of the images, there was at least one scale with higher values than SExtractor, demonstrating that in these particular images, the detection power of MDS can compete with and improve on the results of the reference SExtractor software.

We can achieve even higher TSD rates by combining the detections achieved in the three scales at the expense of obtaining slightly lower TP percentages. By combining the detections with 95% reliability, the percentages of TP and TSD were 93.10% and 88.83% with the $WISE_{3.4}$ image, 92.40% and 89.55% with the $WISE_{4.6}$ image, 94.12% and 64.26% with the $WISE_{12}$ image, 89.53% and 71.98% with the $CGPS_{21}$ image, and 91.85% and 66.31% with the $CGPS_{74}$ image. Whereas by combining the detections with 90% reliability, the TP and TSD percentages were 87.10% and 90.89% with the $WISE_{3.4}$

Table 5.1: Summary of the MDS results obtained demanding 90% reliability. For each image, the number of detections, the percentage of true positives, and the number of true sources detected are shown.

	DS	MDS (SWT_1)	MDS (SWT_2)	MDS (SWT_3)	MDS (MHWT)	SExtractor
	1027	1664	1601	1346	1013	1511
$WISE_{3.4}$	90.17	90.08	90.51	90.19	90.03	90.01
	54.44	**88.12**	85.19	71.37	53.62	79.95
	800	1384	1354	1148	898	1240
$WISE_{4.6}$	90.25	90.39	90.10	90.07	90.09	90.16
	50.63	**87.73**	85.55	72.51	56.73	78.40
	107	188	197	170	126	143
$WISE_{12}$	90.57	90.43	90.36	90.00	90.48	90.21
	38.55	68.27	**71.49**	61.45	45.78	51.81
	629	931	955	723	972	1041
$CGPS_{21}$	90.46	90.55	90.47	90.04	90.02	90.11
	46.07	68.26	69.46	52.71	70.85	**75.95**
	183	376	422	429	384	371
$CGPS_{74}$	90.16	90.69	90.05	90.21	90.10	90.30
	29.41	60.78	67.74	**68.98**	61.68	59.71

Table 5.2: Summary of the MDS results obtained demanding 95% reliability. For each image, the number of detections, the percentage of true positives, and the number of true sources detected are shown.

	DS	MDS (SWT_1)	MDS (SWT_2)	MDS (SWT_3)	MDS (MHWT)	SExtractor
	605	1508	1484	1240	590	1448
$WISE_{3.4}$	95.21	95.16	95.01	95.00	95.08	95.44
	33.86	**84.36**	82.89	69.25	32.98	81.25
	367	1263	1254	1034	503	1183
$WISE_{4.6}$	95.10	95.25	95.14	95.16	95.43	95.35
	24.47	**84.36**	83.66	69.00	33.36	79.10
	83	164	165	132	-	126
$WISE_{12}$	95.18	95.12	95.15	95.45	-	95.24
	31.73	62.65	**63.05**	50.60	-	48.19
	546	824	865	630	847	928
$CGPS_{21}$	95.60	95.39	95.14	95.24	95.03	95.04
	42.27	63.64	66.64	48.58	66.64	**71.42**
	111	324	357	360	308	266
$CGPS_{74}$	95.50	95.68	95.24	95.00	95.15	95.11
	18.89	55.26	60.61	**60.96**	52.41	45.10

image, 85.29% and 90.67% with the $WISE_{4.6}$ image, 88.35% and 73.09% with the $WISE_{12}$ image, 81.46% and 75.06% with the $CGPS_{21}$ image, and 84.38% and 74.15% with the $CGPS_{74}$ image.

An analysis of the sources detected according to their brightness is illustrated in Figures 5.7 and 5.8. From these we can conclude that, in all cases, the number of sources detected is clearly higher in all the brightness bins (faint, mid-intensity and bright) with MDS than with DS. Specially remarkable are the detections in the faint bin with the first two scales of the SWT. In the mid-intensity and bright bins the percentage of detection with DS was already acceptable, but in spite of this fact, the values rose slightly as well. In turn, SExtractor proved to be a very competitive algorithm to detect mid-intensity and bright sources. However, MDS obtained similar results in these brightness levels and outperformed SExtractor at unveiling faint objects.

5.4 Discussion

According to the results obtained with MDS, it is clear that it represents an important improvement. The completeness of DS has increased significantly with its combination of multiscale techniques. In some cases, the completeness of the catalogues obtained more than doubled or tripled. In all the different variants and scales in the wavelet transform, results were better than when using DS alone. In general, the scales that offered more balanced percentages were the SWT_1 and the SWT_2. This is more evident in infrared images. The MHWT has performed better with radio images, although the best scale in the $CGPS_{74}$ image is the SWT_3. In images with mainly point and compact sources, such as $WISE_{3.4}$, $WISE_{4.6}$ and $CGPS_{21}$, the high spatial frequency scales, the first of the SWT and the MHWT, have performed better because they are the most suited scales to highlight sources with these shapes. On the other hand, in images such as $WISE_{12}$ and $CGPS_{74}$, which present more extended emissions, lower spatial frequency scales performed better. Moreover, in the vast majority of cases, MDS outperformed SExtractor, mainly at detecting faint objects. This clearly proves that the use of WT helps DS to perform a better characterization of images with complex backgrounds.

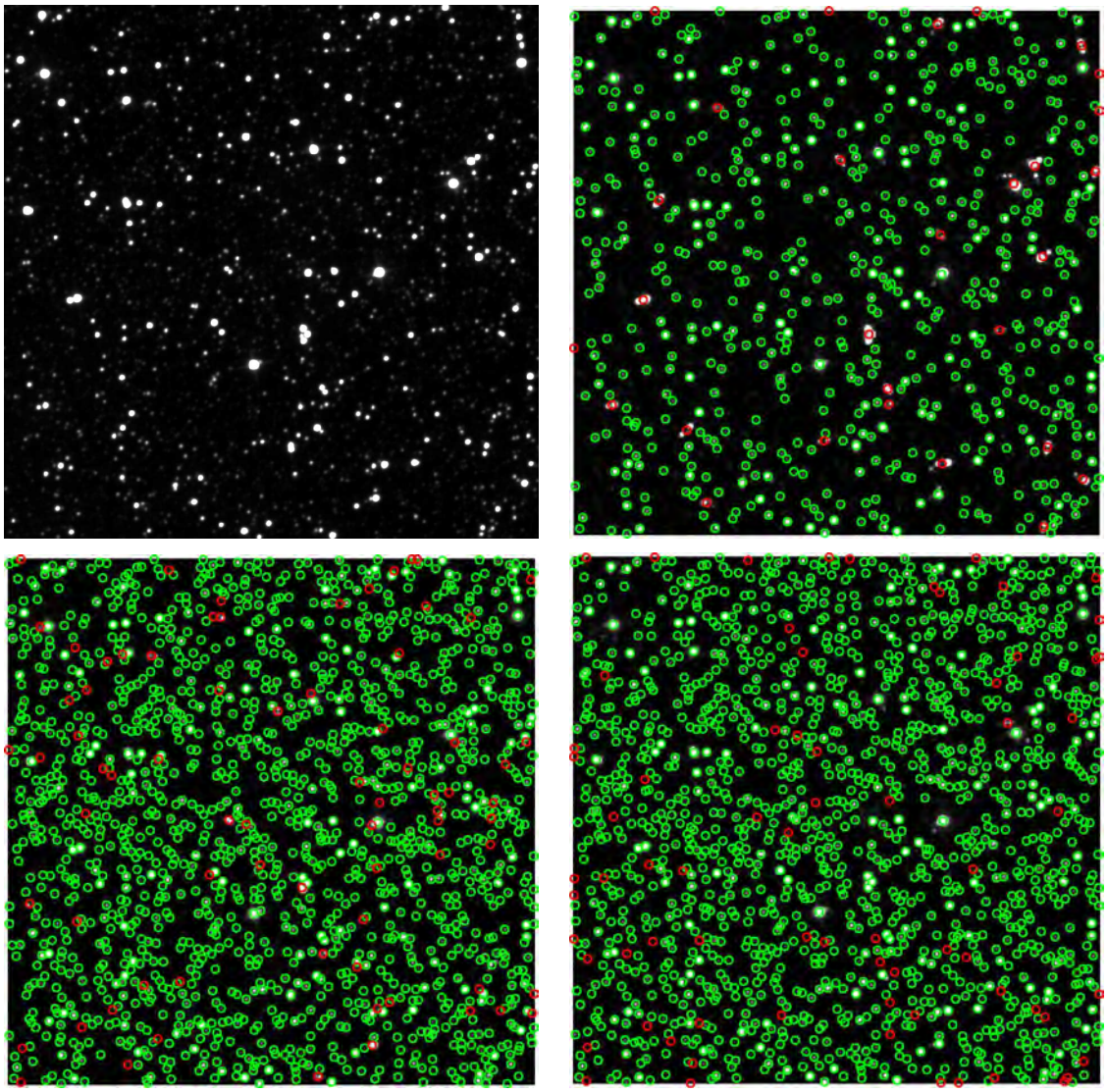

Figure 5.2: Qualitative results obtained in $WISE_{3.4}$ with MDS with 95% reliability. From top to bottom and left to right: the raw image, the detections obtained with DS, those with MDS using the SWT_1 scale, and those with SExtractor. Green circles indicate TP while red circles indicate FP.

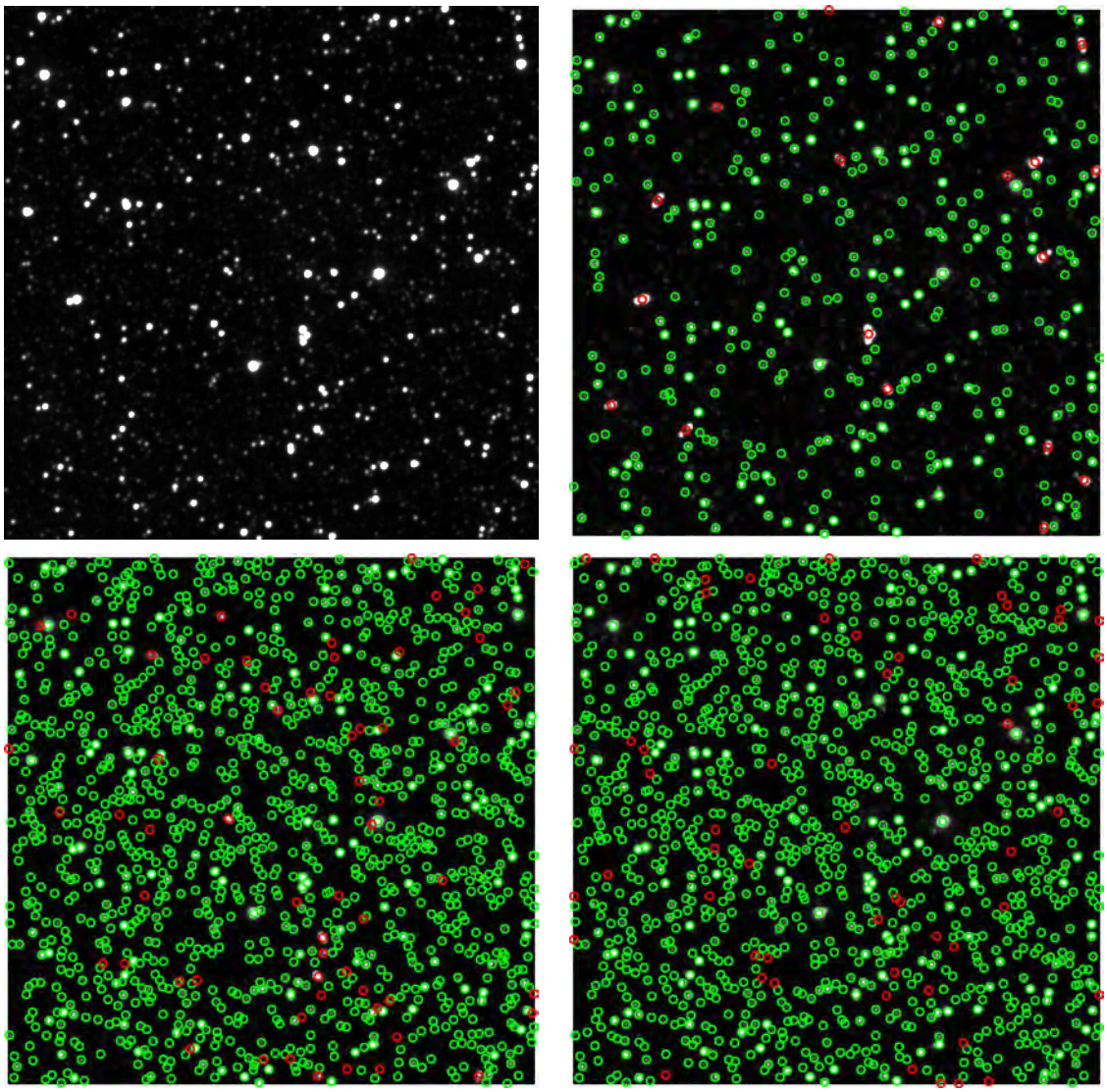

Figure 5.3: Qualitative results obtained in $WISE_{4.6}$ with MDS with 95% reliability. From top to bottom and left to right: the raw image, the detections obtained with DS, those with MDS using the SWT_1 scale, and those with SExtractor. Green circles indicate TP while red circles indicate FP.

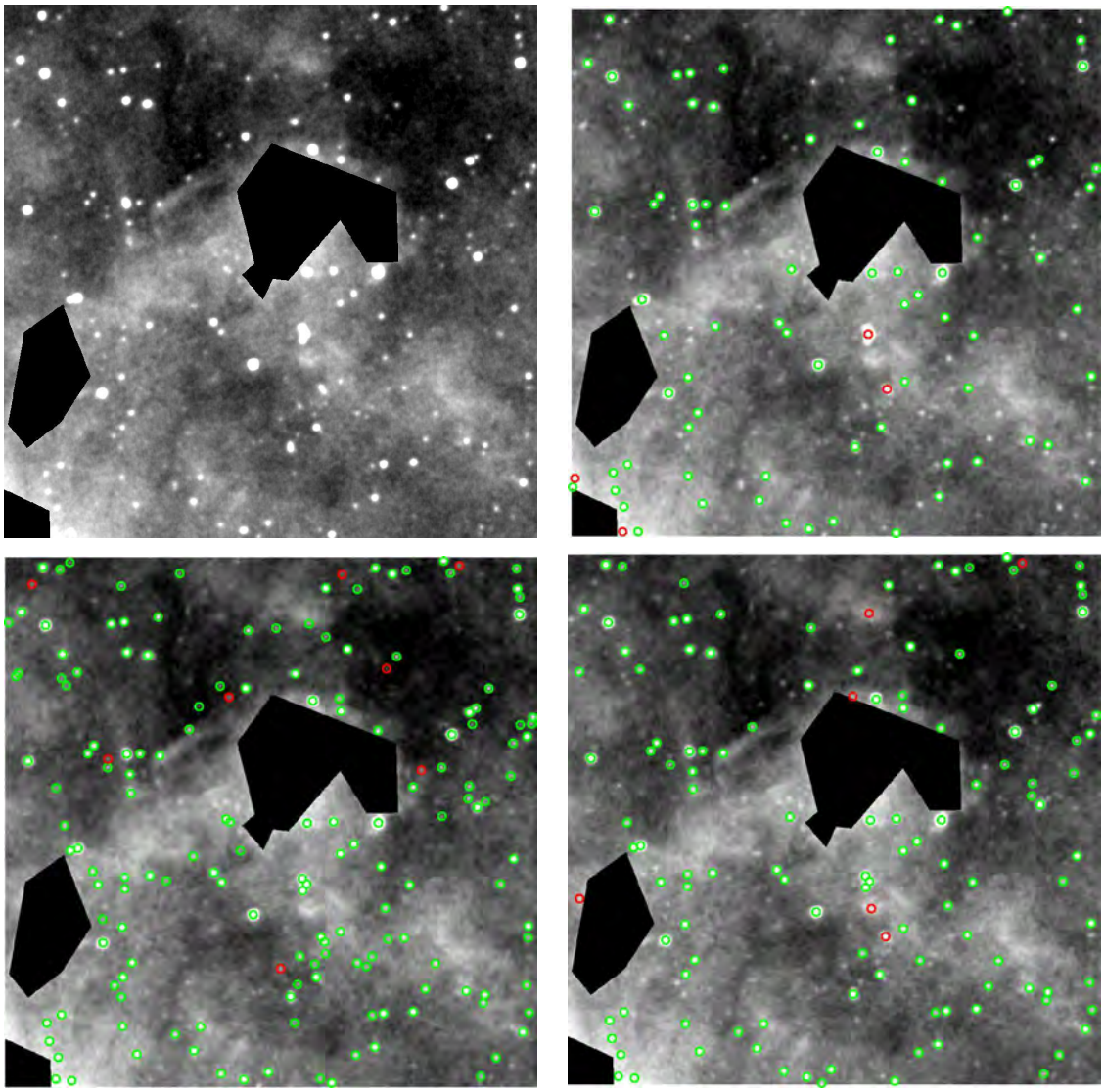

Figure 5.4: Qualitative results obtained in $WISE_{12}$ with MDS with 95% reliability. From top to bottom and left to right: the raw image, the detections obtained with DS, those with MDS using the SWT_2 scale, and those with SExtractor. Green circles indicate TP while red circles indicate FP.

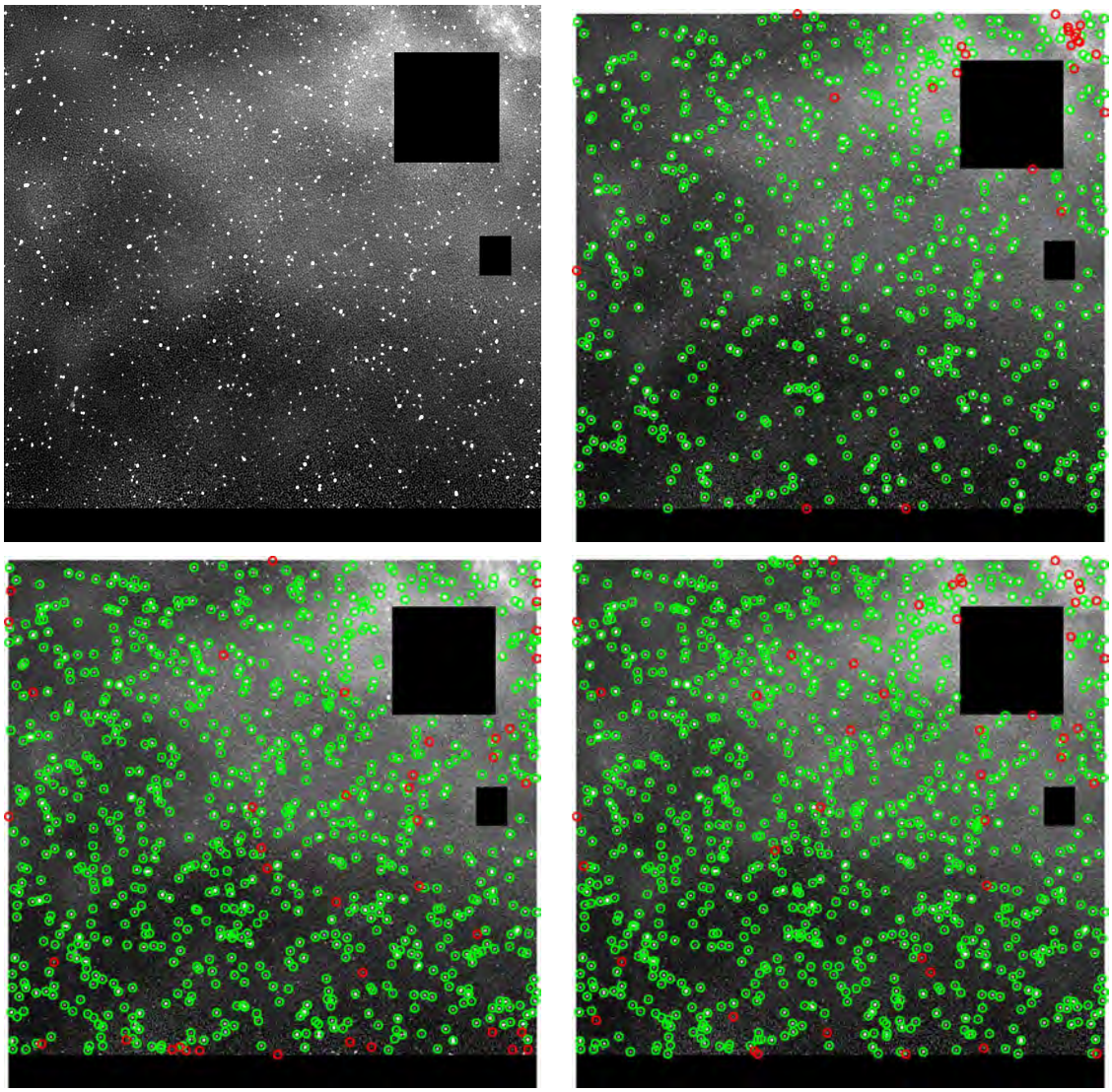

Figure 5.5: Qualitative results obtained in $CGPS_{21}$ with MDS with 95% reliability. From top to bottom and left to right: the raw image, the detections obtained with DS, those with MDS using the MHWT scale, and those with SExtractor. Green circles indicate TP while red circles indicate FP.

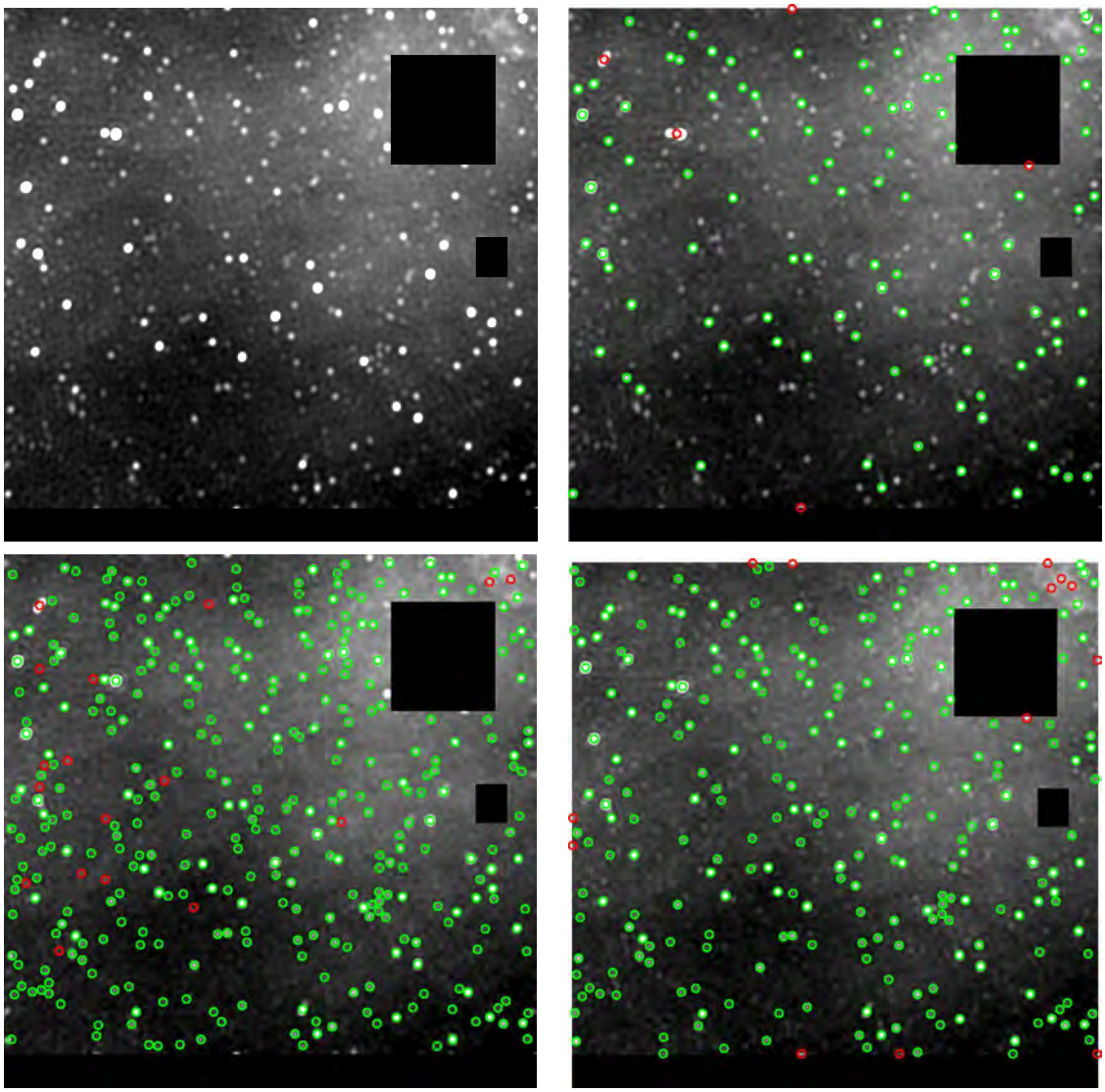

Figure 5.6: Qualitative results obtained in $CGPS_{74}$ with MDS with 95% reliability. From top to bottom and left to right: the raw image, the detections obtained with DS, those with MDS using the SWT_3 scale, and those with SExtractor. Green circles indicate TP while red circles indicate FP.

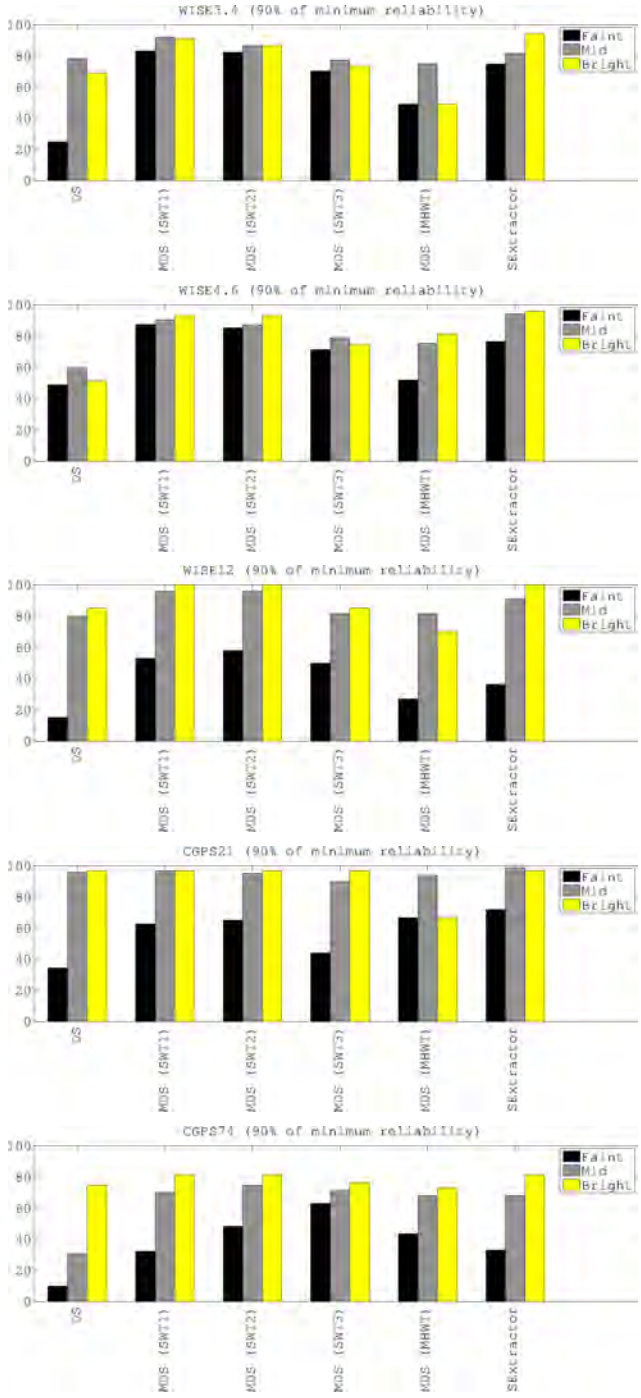

Figure 5.7: Graphical representation of the percentages of TSD demanding 90% reliability according to the brightness of the sources. From top to bottom, the results obtained with DS, MDS using different scales and SExtractor with images $WISE_{3.4}$, $WISE_{4.6}$, $WISE_{12}$, $CGPS_{21}$ and $CGPS_{74}$.

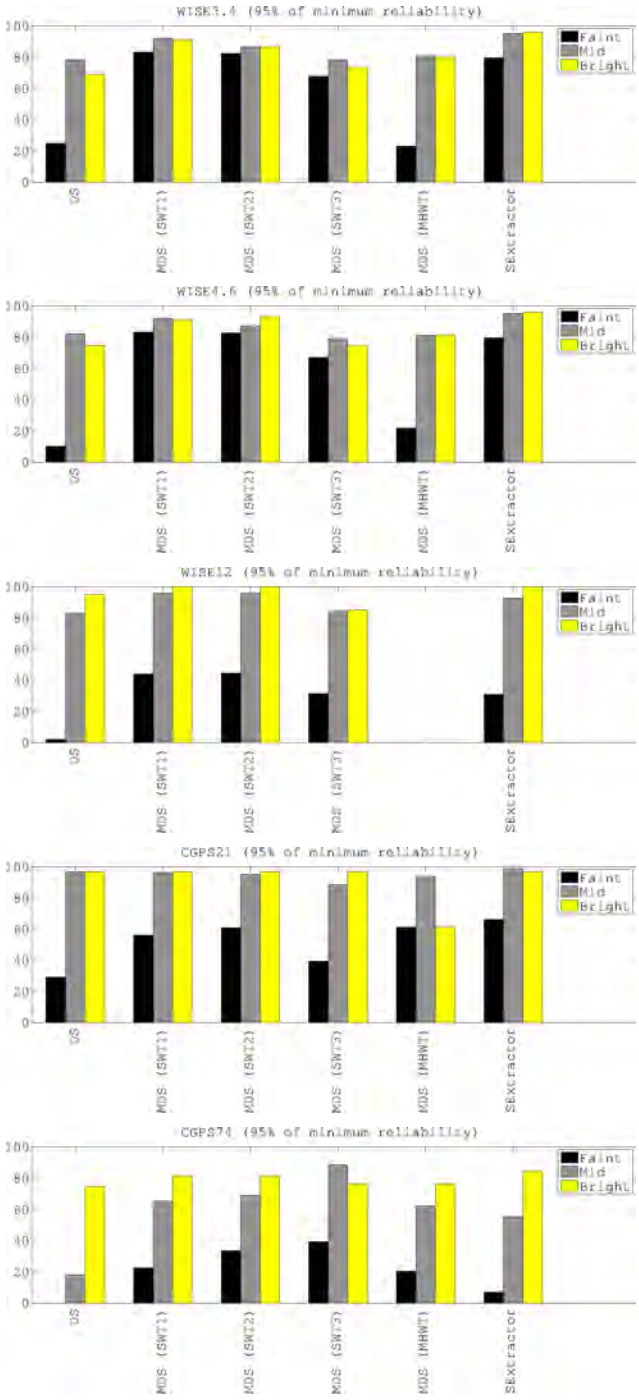

Figure 5.8: Graphical representation of the percentages of TSD demanding 95% of reliability according to the brightness of the sources. From top to bottom, the results obtained with DS, MDS using different scales and SExtractor with images $\text{WISE}_{3.4}$, $\text{WISE}_{4.6}$, WISE_{12}, CGPS_{21} and CGPS_{74}.

5.5 Conclusions

Aiming to deal with long wavelength images such as infrared and radio, we have proposed a new approach based on multiscale decomposition and Distilled Sensing. In these images characterized by complex backgrounds, Multiscale Distilled Sensing has provided satisfactory results since the number of true sources detected has been substantially better than using DS directly. The number of fainter sources identified has dramatically increased in some scales. Specifically, the results have been particularly good in the first two scales of the SWT, the 'à trous' algorithm. Furthermore, the quantitative comparison of the new approach with the original DS and the commonly used SExtractor software has demonstrated the validity of the combined use of DS and wavelets, results obtained with MDS being better in most cases analyzed.

This method and the three others presented in Chapter 4 represent an important contribution to the astronomical community. They are really useful for working on long wavelength images. MDS has significantly outperformed DS, being able to detect more sources of different brightness in radio and infrared images, specially faint ones. Although MDS is also a good choice, WALT, RCF and the boosting classifier are more appropriate methods to use in images with a large population of faint sources, such as the GMRT and ATCA radio images, because they have been developed for this specific purpose.

Chapter 6

Conclusions

6.1 Summary of the thesis

The goal of this thesis has been the analysis and development of different strategies to detect astronomical sources in images. After analyzing a wide variety of techniques from the state of the art, we saw that the detection process can be divided into two main steps: the image transformation and the detection criterion. The first consists of applying modifications in the content of the raw image in order to achieve better conditions to detect sources. The second consists of applying different rules to determine which pixels belong to sources and which not, and consequently, detect the location of the sources. From this review, we realized the importance of transforming the image with simple techniques such as filtering or with more complex ones such as matched filtering, Bayesian or multiscale. Since astronomical images have an important contribution of noise, interferences, variable and inhomogeneous background regions, and a great number of objects with a high dynamic range and different sizes and vague shapes, the use of these types of techniques is fundamental to attenuate all theses harmful effects and to increase the difference between noise/background and sources, and therefore, to boost further detection. This detection process is typically carried out through two main techniques that can be used interchangeably: thresholding and local peak search.

In Chapter 2, advantages and drawbacks of the different methods were provided in a qualitative way. However, they were based on the reported application of the methods with specific types of images with particular features and for specific aims. For instance, it is difficult to compare a method designed for detecting extended sources in radio images with another designed for detecting point sources in X-ray images. Hence, we decided to perform a more meaningful quantitative evaluation of some of the most remarkable methods in the literature. In Chapter 3, eight methods were selected, trying to cover the

whole range of techniques found in the state of the art. They were applied to the same multiwavelength dataset consisting of optical images from the SDSS, infrared images from the WISE, and radio images from the CGPS. Reliable catalogues were used as the ground truth to quantify the quality of the detections of the methods in terms of true positives and true sources correctly identified. These measures led to the identification of the best methods in general and the best for specific types of images. Nevertheless, other characteristics such as the computational cost or the parameter setting were taken into account to recommend the use of the methods in particular cases.

The conclusions extracted from this exhaustive review and the quantitative evaluation of these methods led us to some ideas to propose new detection approaches. We decided to explore the detection limits of new proposals in radio aperture synthesis images, specifically exploiting the challenging detection of faint sources with intensities close to background/noise levels. The choice of this type of image was due to two main reasons: on the one hand, they are excellent benchmarks because they present marked varying interferometric backgrounds and a large population of different types of sources and, therefore, a great number of faint ones; and on the other hand, they are the principal type of image used in the projects this PhD thesis is related to. In particular, we used images from the GMRT and the ATCA instruments as well as simulations. Three new proposals came out: the first, a method that combines the multiscale wavelet transform and local thresholding (WALT); the second, a method based on the structural behaviour of an intensity radial contrast function (RCF); and the third, a supervised method that classifies pixels by means of local features (filtered patches) and a boosting classifier. In Chapter 4, different experiments were conducted with the different methods so that they achieved different levels of reliability, percentage of true detections, and completeness, percentage of sources of the catalogue correctly detected. The comparison of the new proposals with commonly-used software such as SExtractor and SAD demonstrated a remarkable performance by the first ones. They were able to detect more sources than the reference, specially faint ones, and fewer spurious detections were obtained. In general, the boosting classifier offered very reliable and complete results. This was due to the fact that it is a supervised method that requires training data to create a model to classify the pixels. WALT and RCF provided very competitive results too, and have the advantage of a simpler parameter tuning. RCF was the method that generally detected more faint sources, and WALT obtained very reliable detections and dealt better with noisy regions.

Moreover, from the initial qualitative and quantitative analyses, we also found a really interesting method called Distilled Sensing (DS). The innovation of this method lies in

the fact that, instead of trying to detect the sources, it iteratively discards background regions more easily identified as such. This way, at the end of this process, it is easier to unveil the sources, e.g. with a simple threholding. Its quantitative results proved a general good performance in terms of reliability. It was also able to provide complete catalogues in optical data, but as with many other methods, the number of true sources detected decreased in lower frequency bands such as radio and infrared. In Chapter 5, we decided to overcome this lack by means of the combined use of DS and a multiscale technique such as the wavelet transform which is widely used and characterized by attenuating the impact of the more complex backgrounds present in this type of image. Two different variants of the wavelet transform were used: the stationary (SWT) and the Mexican hat (MHWT) wavelet transform. The use of DS in multiscale space (MDS) presented an important improvement with respect to the raw DS method. The reliability of the new method rose dramatically in both datasets and the validity of the method was proven since it achieved better results than the widely-used SExtractor algorithm.

6.2 Contributions

The main objective of this thesis was to provide astronomers with new algorithms to automatically detect sources in astronomical images. Additionally, the discussions provided in this work can be useful for astronomers, and can be used as a starting point when a source detection strategy is to be used or implemented in a particular type of dataset. Therefore, the main contributions of this thesis are:

- An extensive updated review of astronomical source detection algorithms which includes a new classification of the strategies and their main strengths and weaknesses according to their performance.
- A quantitative evaluation of some of the most promising methods in the literature. They were applied to a common radio (CGPS), infrared (WISE) and optical (SDSS) dataset in a level playing field, and their performances were evaluated by means of reliable catalogues and commonly used evaluation measures. The key points and lacks of the algorithms with the various types of images were pointed out, thus this evaluation becomes an appropriate starting point for those who want to identify sources in images.
- Three new algorithms to detect faint sources in radio aperture synthesis images: WALT applies local thresholding, based on a histogram fitting, to the first three

wavelet scales; RCF analyses the spatial coherence of neighbouring pixels through an intensity radial contrast function; while the boosting classifier uses a source model trained with local features to classify pixels into sources or background. They were exhaustively tested using real data from the GMRT and the ATCA instruments and simulations.

- A new algorithm to detect sources in radio and infrared images based on the combined use of the wavelet transform and the innovative Distilled Sensing method (MDS). It was exhaustively tested using real data from the CGPS (radio) and the WISE (infrared) surveys.

- An experimental qualitative and quantitative comparison between our various proposals and well-known state-of-the-art algorithms in terms of reliability and completeness of the detections provided.

- A synthetic dataset of radio aperture synthesis images. It consists of three realistic images with different rms noise levels and many injected sources that can be used to test detection algorithms.

6.3 Future work

We are aware that the automatic detection of astronomical sources is a broad and complex topic. For example, each type of image, noise distribution or source morphology could be analyzed separately. Furthermore, we have seen that detection is just one of the steps in the source extraction pipeline, and, at the same time, it can be divided into different steps such as the image transformation and the detection criteria. Research efforts can focus on particular or multiple parts of the detection or extraction pipelines. We have developed different proposals consisting of techniques that can be studied further. They can even be useful in different topics of the computer vision domain such as medical imaging. Hence, some future work related to the improvement of the proposals presented in this thesis as well as related new work are mentioned below.

An extensive quantitative evaluation of radio, infrared and optical images has been presented. To the best of our knowledge, no other quantitative review involving such a wide number of methods has been conducted. As we have seen in the state of the art, these three bands are characterized by Gaussian background distributions, which makes the use of the same methods possible with all of them. However, there are other bands

such as X-rays and γ-rays that present Poisson background distributions. Therefore, we believe that it would be interesting to carry out a quantitative evaluation of techniques able to deal with these types of images to make our study more complete.

In this thesis, different proposals based on different techniques have been developed. They have been tuned in order to achieve certain requirements of reliability or completeness, and as we have claimed, these two measures tend to be anti-correlated: the more true sources found, the more spurious detections, and vice versa; the more true detections, the more true sources missed. Any kind of postprocess could be used to solve this problem. It is obviously far easier to remove false positives than create true positives from nothing. Therefore, we believe that the development of false detection steps would be a step forward in the automation of the detection of sources in a reliable way. For instance, it could be based on the analysis of the shape of the detections.

As we have already mentioned, the boosting classifier is a very reliable method that, after having prior knowledge, can be useful to automatically detect huge amounts of data. For instance, the astronomical surveys that have come out in the last few years (see Section 1.1.1) are composed of different fields. After using a few of these fields to build the dictionary and to train the classifier, the rest of the fields could be automatically processed. Since we have proposed other methods to detect sources that are able to achieve high regimes of reliability (even 100%), their detections in some fields can be used as positive samples in the training process of the boosting classifier. With just some negative samples, the training can be complete, and the algorithm can be applied to the rest of the fields. Hence, the combination of the boosting classifier with WALT, RCF or MDS could be very useful to astronomers. We believe that MDS is the most appropriate method to be part of this incremental learning approach because, apart from providing reliable detections, it iteratively discards, and therefore, identifies, background pixels.

This PhD thesis is focused mainly on the detection of point and compact sources. However, objects with extended shapes are very important to the understanding of the Universe. For this reason, other future work could be devoted to developing new methods or to adapt those proposed in this thesis to detecting this type of source. For instance, a good starting point could be the adaptation of WALT so that it can apply the thresholding in lower frequency scales (higher index planes) which are more suitable for detecting extended emissions. A method able to detect point, compact and extended sources at the same time would be very interesting to astronomers.

Astronomers are specially interested in the photometry of sources, and hence, they ap-

preciate those methods that provide detections together with additional information on the sources. Therefore, another improvement we propose is the implementation of an additional step to perform a photometric analysis of the detections obtained with our proposals. Moreover, if we translate our codes into a more efficient and optimized programming language (e.g. c++ or python) they could have as much impact and acceptance as other popular source extraction algorithms such as SExtractor. Thus, a toolbox with all the methods together could be placed at the disposal of the community.

Finally, we think that the algorithms we have presented can be useful in other areas of computer vision and image processing. For instance, there are many medical imaging fields that deal with challenges similar to astronomical source detection. The VICOROB group of the university of Girona has been working on medical imaging since 1996. There are several research lines in progress such as those devoted to the detection and diagnosis of different types of cancer (breast, prostate and skin) or multiple sclerosis lesions. Therefore, it would be interesting to see if the astronomical detection methods can be somehow adapted to identify lesions in medical images. Actually, we are already collaborating in these medical fields: the boosting classifier was recently used for the detection of microcalcifications and clusters (small bright spots within an inhomogeneous background that can indicate the presence of a breast cancer) in mammographic images with great success [72]. Still, there are many other possible applications. For example, ultrasound images of breasts or prostates present a high level of noise that make the detection/segmentation of lesions difficult. We could use the image transformation part of our methods to filter the noise and ease further processing.

Appendix A

Parameter setting

A summary of the values assigned to the main parameters of the different methods used is shown below. They have been adjusted in order to omptimize the performance of the methods and to achieve specific requirements.

A.1 Quantitative evaluation of methods

Although we usually refer to automatic detection methods, most of them are not fully automatic since they are based on a set of parameters that have to be tuned in advance. With the exception of SExtractor and Astrometry.net, which are able to detect sources with no user specification, all the other methods need an accurate tuning to achieve the best possible performance. The parameter setting has to be done properly in order to guarantee a suitable compromise between reliability and completeness. Most of the methods have parameters other than those discussed here, but for the purpose of this evaluation, we have used only those parameters that are crucial to achieve acceptable detections. Note that there is no information on the parameters of the Perret method because, for privacy reasons, it was executed by the authors themselves and we have only analyzed the results obtained.

The parameter settings shown in Table A.1 lead us to what we have considered to be the best results obtained. Notice that we have been able to apply SAD successfully to the SDSS images with no parameter setting, while negative thresholds in SourceMiner are due to the fact that a background pixel is more likely than a source one.

We have defined exploration ranges of thresholds with different samplings (intervals) to find the optimal values. The following results show why this type of parameter is so important. For instance, in the $SDSS_i$ image, by setting the absolute threshold of the DS

Table A.1: Summary of the parameter settings used for each method and dataset involved in the quantitative evaluation in Chapter 3.

Method	Parameter	$SDSS_u$	$SDSS_g$	$SDSS_r$	$SDSS_i$	$SDSS_z$	$WISE_{3.4}$	$WISE_{4.6}$	$WISE_{12}$	$CGPS_{21}$	$CGPS_{74}$
SAD	Vector	-	-	-	-	-	11	12	435	6	65
							10	11	430	5.5	60
							9	10	425		55
							8	9			50
Mopex	σ	0.5	0.5	0.5	0.5	0.5	0.5	0.5	0.5	0.5	0.5
GN	σ	1.5	1.5	1.5	1.5	1.5	0.5	0.5	0.5	1.5	1.5
SourceMiner	Threshold	-5.3	-5.7	-5.7	-5.7	-6	-5.7	-5.7	-6	-4.8	-7.2
DS	Threshold	1.5	1.3	1.7	2.2	9.8	26.1	34.0	1198.8	51.0	4903.5

method to 2.1, 2.2 and 2.3 we achieve 89.27%, 91.19% and 92.50% TP and 70.81%, 69.66% and 68.33% TSD, respectively. On the other hand, in $CGPS_{21}$, by fixing the threshold of SourceMiner to -4.7, -4.8 and -4.9, we obtain 93.74%, 86.90 and 71.18% TP and 64.29%, 71.42% and 74.98% TSD, respectively. From these results, we can see that slight changes in the values can provide different results. The higher the TP rate, the lower the TSD rate, and vice versa. Therefore, the threshold values have been chosen in all the tests in order to minimise the errors of both the TP and TSD percentages.

Some of the parameters can be obtained directly from the characteristics of the images or from the information included in the catalogues. For example, the FWHM of the sources is required for González-Nuevo (GN) and SourceMiner, which also uses the pixel scale.

The methods based on matched filtering require samples of the sources expected to be found. In the case of Mopex, a patch of 21×21 pixels containing a sample source has been used.

On the other hand, the detections provided by several methods depend on the accurate tuning of some of their input parameters. In most cases, the most significant parameter is a level or threshold that has to be fixed. That value is frequently related to the flux of the different pixels in the image. SAD, for example, uses a vector of up to ten values with different thresholds corresponding to different flux cut-offs that are applied sequentially in descending order to the image. Mopex and GN are based on a σ-clipping step, a number of σ above the mean of the image pixels, to determine the detection threshold in the first case, and the level above which maximum of the local peak search is considered as a source in the second. In a different way, SourceMiner needs a threshold that becomes the argument of an exponential function that indicates the number of times a pixel is more likely to be part of a source than part of the background. Finally, DS also requires a parameter as an absolute threshold.

A.2 Faint source detection methods

To achieve the best results possible with WALT, RCF and the boosting classifier, we experimented with different parameter settings. Tables A.2 and A.3 show those that provided the best performances in synthetic and real data.

Table A.2: Summary of the parameter settings used for each method and simulated image to achieve levels of 90% and 95% reliability and completeness.

		0.01 rms noise				0.02 rms noise				0.04 rms noise			
Method	Parameter	Completeness		Reliability		Completeness		Reliability		Completeness		Reliability	
		95%	90%	90%	95%	95%	90%	90%	95%	95%	90%	90%	95%
WALT	g	7	7	7	7	7	7	7	7	7	7	7	7
	k	1.72	2.03	2.13	2.21	1.48	1.76	2.07	2.37	1.63	1.72	2.25	2.32
RCF	rsq	0.99	0.99	0.99	0.99	0.99	0.99	0.99	0.99	0.99	0.99	0.99	0.99
	m	1.30	3.95	5.40	6.60	0.94	3.3	4.80	4.84	0.40	0.90	2.90	5.40
Boosting	th	2.15	5.3	5.55	6.33	2.64	5.32	9.29	9.81	0.88	1.49	5.73	6.59
SExtractor	threshold	1.76	3.09	3.39	3.56	1.72	2.70	3.39	3.56	1.22	1.80	3.41	3.6
SAD	threshold	0.022	0.037	0.04	0.042	0.05	0.068	0.0815	0.085	0.073	0.097	0.1597	0.169

Table A.3: Summary of the parameter settings used for each method and real image to achieve levels of 90% and 95% reliability and completeness.

		GMRT				ATCA			
Method	Parameter	Completeness		Reliability		Completeness		Reliability	
		95%	90%	90%	95%	95%	90%	90%	95%
WALT	g	7	7	7	7	7	7	7	7
	k	5.8	7.1	7.9	10.0	2.09	2.44	2.69	2.95
RCF	rsq	0.99	0.99	0.99	0.99	0.95	0.95	0.95	0.95
	m	0.9831	0.9851	0.9864	0.98825	0.98582	0.988	0.98365	0.98756
Boosting	th	9.2	12.7	16.3	19.1	6.9	7.12	15.42	15.49
SExtractor	threshold	6.27	7.4	9.1	9.76	2.96	3.25	5.74	6.46
SAD	threshold	0.0024	0.00251	0.00355	0.00401	0.0000685	0.0000735	0.000166	0.00023

In the WALT algorithm, we used 400 subimages, $g = 7$ and different values for k to reach the requirements of completeness and reliability.

In the RCF algorithm, we fixed the rsq and tested different slopes to reach the requirements of completeness and reliability. The range of radii was set from 1 to 5 in intervals of 0.5 for all the images.

In the boosting classifier, we extracted patches with side sizes of 3, 5 and 7 pixels for all the images. The threshold th was adjusted differently in the various images to fulfil the completeness and reliability requirements. In the training step, about 400 positive and 7000 negative samples were used in all the images. Additionally, other factors had to be taken into account in this algorithm. For example, a leave-one-out strategy was used to build the different datasets. This is an iterative process where, at each step, a different image is used for testing while the others are used to perform the training. In our case, we used three images to generate the dictionary and three more to extract training features. In order to have multiple images, we created more synthetic images by using the GMRT fields independently and dividing the ATCA image into 16 subimages.

To reach the expected levels of completeness and reliability in SExtractor and SAD, we tuned their detection thresholds. In the first case, it was based on σ-clipping while in the second, it was in terms of flux.

A.3 Multiscale Distilled Sensing

A key parameter in both DS and MDS is the detection threshold. It is a data-based value that we have experimentally fixed for each image in each of the scales used. Table A.4 summarizes the thresholds that provided the best results for reliability levels of 90% and

Table A.4: Summary of the thresholds used to achieve reliability levels of 90% and 95% in the comparison of MDS to DS and SExtractor.

Image	DS		MDS (SWT_1)		MDS (SWT_2)		MDS (SWT_3)		MDS (MHWT)		SExtractor	
	90%	95%	90%	95%	90%	95%	90%	95%	90%	95%	90%	95%
$WISE_{3.4}$	460	805	20.7	23.8	45.1	49.6	46.6	54.3	16676	45300	3.3	3.76
$WISE_{4.6}$	274	402	3.94	4.45	8.65	9.6	11	12.7	4661	12940	3.09	3.47
$WISE_{12}$	179578	180343	102.8	119.2	224	267	340	476	289700	-	4.66	5.53
$CGPS_{21}$	50.89	51.85	1.85	2.05	1.87	2.05	1.28	1.47	4.99	5.51	3.36	3.91
$CGPS_{74}$	4934	5388	11.98	13.43	31.8	36.5	63.1	76	239	303	3.24	5.16

95%. Notice that, since they depend on the transformed data, they are quite different.

Moreover, the parameter ϵ corresponding to the relationship between the energy sensing allocation between two successive iterations was fixed to 0.75, since the authors of DS mentioned that this value provides good performance in data with different levels of noise. This value implies that the resources devoted to an iteration are 0.75 times fewer than in the previous iteration.

Bibliography

[1] H. Aihara et al. The eighth data release of the sloan digital sky survey: First data from SDSS-III. *ApJS*, 193, 2011.

[2] S. Andreon, G. Gargiulo, G. Longo, R. Tagliaferri, and N. Capuano. Wide field imaging - I. Applications of neural networks to object detection and star/galaxy classification. *MNRAS*, 319:700–716, 2000.

[3] E. Aptoula, S. Lefèvre, and C. Collet. Mathematical morphology applied to the segmentation and classification of galaxies in multispectral images. In *Proc. EUSIPCO*, 2006.

[4] W. B. Atwood et al. The Large Area Telescope on the Fermi Gamma-Ray Space Telescope Mission. *ApJ*, 697:1071–1102, 2009.

[5] A. N. Belbachir and P. M. Goebel. A combined multiresolution approach for faint source extraction from infrared astronomical raw images sequence. In *Proc. SSP*, pages 459–464, 2005.

[6] E. Bertin and S. Arnouts. SExtractor: software for source extraction. *A&AS*, 117:393–404, 1996.

[7] A. Bijaoui. Sky Background Estimation and Applications. *A&A*, 84:81–84, 1980.

[8] A. Bijaoui, A. Guennec, C. Benoist, and E. Slezak. Analysis of multiband astronomical images using multiscale tools. In *Proc. SPIE*, volume 6001, pages 1–12, 2005.

[9] A. Bijaoui and F. Rué. A multiscale vision model adapted to the astronomical images. *Signal Processing*, 46:345–362, 1995.

[10] H. Bradt. *Astronomy methods: A physical approach to astronomical observations*. Cambridge University Press, Cambridge, UK, 2004.

[11] P. S. Broos, L. K. Townsley, E. D. Feigelson, K. V. Getman, F. E. Bauer, and G. P. Garmire. Innovations in the Analysis of Chandra-ACIS Observations. *ApJ*, 714:1582–1605, 2010.

[12] R. Buonanno, G. Buscema, C. E. Corsi, I. Ferraro, and G. Iannicola. Automated photographic photometry of stars in globular clusters. *A&A*, 126:278–282, 1983.

[13] E. J. Candès and D. L. Donoho. Ridgelets: The key to high dimensional intermittency? *Phil. Trans. Royal Soc. Lond. A*, 357:2495–2509, 1999.

[14] E. J. Candès and D. L. Donoho. Curvelets, multiresolution representation, and scaling laws. In *Proc. SPIE*, volume 4119, pages 1–12, 2000.

[15] P. Carvalho, G. Rocha, and M. P. Hobson. A fast Bayesian approach to discrete object detection in astronomical data sets - PowellSnakes I. *MNRAS*, 393:681–702, 2009.

[16] J. J. Condon, W. D. Cotton, E. W. Greisen, Q. F. Yin, R. A. Perley, G. B. Taylor, and J. J. Broderick. The NRAO VLA sky survey. *AJ*, 115:1693–1716, 1998.

[17] F. Damiani, A. Maggio, G. Micela, and S. Sciortino. A method based on wavelet transforms for source detection in photon-counting detector images. I. Theory and general properties. *MNRAS*, 483:350–369, 1997.

[18] P. E. Dewdney, P. J. Hall, R. T. Schilizzi, and T. J. L. W. Lazio. The Square Kilometre Array. *IEEE Proceedings*, 97:1482–1496, 2009.

[19] V. G. Duval, W. R. Irace, A. K. Mainzer, and E. L. Wright. The wide-field infrared survey explorer (WISE). In *Proc. SPIE*, volume 5487, pages 101–111, 2004.

[20] F. Feroz and M. P. Hobson. Multimodal nested sampling: an efficient and robust alternative to Markov Chain Monte Carlo methods for astronomical data analyses. *MNRAS*, 384:449–463, 2008.

[21] P. E. Freeman, V. Kashyap, R. Rosner, and D. Q. Lamb. A wavelet-based algorithm for the spatial analysis of poisson data. *ApJS*, 138:185–218, 2002.

[22] A. Friedlander, M. Frean, M. Johnston-Hollitt, and C. Hollitt. Latent Dirichlet Allocation for Image Segmentation and Source Finding in Radio Astronomy Images. In *Image and Vision Computing New Zealand Conference*, 2012.

[23] J. Friedman, T. Hastie, and R. Tibshirani. Additive logistic regression: a statistical view of boosting. *The annals of Statistics*, 38(2):337–374, 2000.

[24] R. D. Gehrz and E. E. Becklin. The Stratospheric Observatory for Infrared Astronomy (SOFIA). In *Proc. SPIE*, volume 7012, 2008.

[25] S. N. Goderya and S. M. Lolling. Morphological classification of galaxies using computer vision and artificial neural networks: A computational scheme. *Astrophysics and Space Science*, 279(4):377–387, 2002.

[26] J. González-Nuevo, F. Argüeso, M. López-Caniego, L. Toffolatti, J. L. Sanz, P. Vielva, and D. Herranz. The Mexican hat wavelet family: application to point-source detection in cosmic microwave background maps. *MNRAS*, 369:1603–1610, 2006.

[27] D. Göring, M. A. Klatt, C. Stegmann, and K. Mecke. Morphometric analysis in gamma-ray astronomy using Minkowski functionals: Source detection via structure quantification. *A&A*, 555:A38, 2013.

[28] A. Graps. Introduction to wavelets. *IEEE computational science & engineering*, 2(2):50–61, 1995.

[29] E. W. Greisen. AIPS, the VLA, and the VLBA. *Information Handling in Astronomy - Historical Vistas*, 285:109–125, 2003.

[30] F. Guglielmetti, R. Fischer, and V. Dose. Background-source separation in astronomical images with Bayesian probability theory - I. The method. *MNRAS*, 396:165–190, 2009.

[31] E. Hadjiyska, G. Hughes, P. Lubin, S. Taylor, R. Hartong-Redden, and J. Zierten. The Transient Optical Sky survey data pipeline. *NewA*, 19:99–108, 2013.

[32] M. Haindl and S. Šimberová. A high - resolution radiospectrograph image reconstruction method. *A&AS*, 115:189–193, 1996.

[33] P. J. Hancock, T. Murphy, B. M. Gaensler, A. Hopkins, and J. R. Curran. Compact continuum source-finding for next generation radio surveys. *MNRAS*, 422:1812–1824, 2012.

[34] K. M. Hanson. Introduction to bayesian image analysis. In *Proc. SPIE*, volume 1898, pages 716–731, 1993.

[35] J. Haupt, R. Castro, , and R. Nowak. Distilled sensing: selective sampling for sparse signal recovery. In *Proc. AISTATS*, pages 216–223, 2009.

[36] D. Herranz, M. López-Caniego, J. L. Sanz, and J. González-Nuevo. A novel multifrequency technique for the detection of point sources in cosmic microwave background maps. *MNRAS*, 394:510–520, 2009.

[37] A. D. Herzog and G. Illingworth. The structure of globular clusters. I. Direct plate automated reduction techniques. *ApJS*, 33:55–67, 1977.

[38] M. P. Hobson and C. McLachlan. A Bayesian approach to discrete object detection in astronomical data sets. *MNRAS*, 338:765–784, 2003.

[39] J. A. Högbom. Aperture Synthesis with a Non-Regular Distribution of Interferometer Baselines. *A&AS*, 15:417–426, 1974.

[40] C. Hollitt and M. Johnston-Hollitt. Feature detection in radio astronomy using the circle hough transform. *PASA*, 29:309–317, 2012.

[41] A. M. Hopkins, J. Afonso, B. Chan, L. E. Cram, A. Georgakakis, , and B. Mobasher. The Phoenix Deep Survey: the 1.4 GHz microjansky catalog. *AJ*, 125:465–477, 2003.

[42] A. M. Hopkins, C. J. Miller, A. J. Connolly, C. Genovese, R. C. Nichol, and L. Wasserman. A new source detection algorithm using false-discovery rate. *AJ*, 123:1086–1094, 2002.

[43] S. B. Howell. *Handbook of CCD astronomy*. Cambridge University Press, Cambridge, UK, 2000.

[44] M. J. Irwin. Automatic analysis of crowded fields. *MNRAS*, 214:575–604, 1985.

[45] F. Jansen, D. Lumb, B. Altieri, J. Clavel, M. Ehle, C. Erd, C. Gabriel, M. Guainazzi, P. Gondoin, R. Much, R. Munoz an M. Santos, N. Schartel, D. Texier, and G. Vacanti. XMM-Newton observatory. I. the spacecraft and operations. *A&A*, 365:L1–L6, 2001.

[46] J. F. Jarvis and J. A. Tyson. FOCAS: Faint Object Classification and Analysis System. *AJ*, 86:476–495, 1981.

[47] N. Kaiser, G. Squires, and T. Broadhurst. A method for weak lensing observations. *ApJ*, 449:460–475, 1995.

[48] S. Klepser. A generalized likelihood ratio test statistic for Cherenkov telescope data. *APh*, 36:64–76, 2012.

[49] R. G. Kron. Photometry of a complete sample of faint galaxies. *ApJS*, 43:305–325, 1980.

[50] D. Lang, D. W. Hogg, K. Mierle, M. Blanton, and S. Roweis. Astrometry.net: Blind astrometric calibration of aribrary astronomical images. *AJ*, 139:1782–1800, 2010.

[51] L. F. Lanz, D. Herranz, M. López-Caniego, J. González-Nuevo, G. de Zotti, M. Massardi, and J. L. Sanz. Extragalactic point source detection in WMAP 7-year data at 61 and 94 GHz. *MNRAS*, 428:3048–3057, 2012.

[52] D. Lazzati, S. Campana, P. Rosati, M. R. Panzera, and G. Tagliaferri. The Brera multi-scale wavelet (BMW) ROSAT HRI source catalog I: the algorithm. *ApJ*, 524:414–422, 1999.

[53] O. Le Fèvre, A. Bijaoui, G. Mathez, J. P. Picat, and G. Lelièvre. Electronographic BV photometry of three distant clusters of galaxies. *A&A*, 154:92–99, 1986.

[54] Z. Liu, K. Chiu, and L. Xu. Improved system for object detection and star/galaxy classification via local subspace analysis. *Neural Networks*, 16:437–451, 2003.

[55] M. López-Caniego, D. Herranz, J. L. Sanz, , and R. B. Barreiro. Detection of Point Sources on Two-Dimensional Images Based on Peaks. *EURASIP Journal on Applied Signal Processing*, 15:2426–2436, 2005.

[56] L. B. Lucy. An iterative technique for the rectification of observed distributions. *AJ*, 79(6):745–754, 1974.

[57] D. Makovoz and F. R. Marleau. Point-Source Extraction with MOPEX. *PASP*, 459:341–352, 2006.

[58] S. G. Mallat. Multifrequency channels decompositions of images and wavelet models. In *IEEE Transactions on Acoustics, Speech, and Signal Processing*, volume 37, pages 2091–2110, 1989.

[59] S. G. Mallat. A theory for multiresolution signal decomposition: the wavelet representation. In *IEEE Transactions on Pattern Analysis and Machine Intelligence*, volume 11, pages 674–693, 1989.

[60] D. C. Martin, J. Fanson, D. Schiminovich, P. Morrissey, P. G. Friedman, T. A. Barlow, T. Conrow, R. Grange, P. N. Jelinsky, B. Milliard, O. H. W. Siegmund, L. Bianchi, Y.-K. Byun, J. Donas, K. Forster, T. M. Heckman, Y.-W. Lee, B. F. Madore, R. F. Malina, S. G. Neff, R. M. Rich, T. Small, F. Surber, A. S. Szalay, B. Welsh, and T. K. Wyder. The Galaxy Evolution Explorer: A Space Ultraviolet Survey Mission. *ApJ*, 619:L1–L6, 2005.

[61] M. Masias, J. Freixenet, X. Lladó, and M. Peracaula. A review of source detection approaches in astronomical images. *MNRAS*, 422:1674–1689, 2012.

[62] J. B. Melin, J. G. Bartlett, and J. Delabrouille. Catalog extraction in SZ cluster surveys: a matched filter approach. *A&A*, 117:1113–1128, 2006.

[63] A. Men'Shchikov, P. André, P. Didelon, F. Motte, M. Hennemann, and N. Schneider. A multi-scale, multi-wavelength source extraction method: Getsources. *A&A*, 542, 2012.

[64] K. J. Mighell. Algorithms for CCD stellar photometry. *ASP Conference Series*, 172:317–328, 1999.

[65] S. Molinari, E. Schisano, F. Faustini, M. Pestalozzi, A. M. Di Giorgio, and S. Liu. Source extraction and photometry for the far-infrared and sub-millimeter continuum in the presence of complex backgrounds. *A&A*, 530:A133, 2011.

[66] A. Morselli et al. The space gamma-ray observatory agile. In *Nuclear Physics B*, volume 85 of *Proceedings Supplements*, pages 22–27, 2000.

[67] K. Murphy, A. Torralba, D. Eaton, and W. T. Freeman. *Toward Category-Level Object Recognition*, chapter Recognition of Object Categories, pages 382–400. Springer-Verlag New York, Inc., Secaucus, NJ, USA, 2006.

[68] P. J. Napier, D. S. Bagri, B. G. Clark, A. E. E. Rogers, J. D. Romney, A. R. Thompson, and R. C. Walker. The Very Long Baseline Array. *IEEE Proceedings*, 82:658–672, 1994.

[69] NASA/ESA/STScI. Hubble Site. `http://hubblesite.org/`, 2014. [Online; accessed January-2014].

[70] B. Newell and E. J. O'Neil Jr. The reduction of panoramic photometry. I. Two search algorithms. *PASP*, 89:925–928, 1977.

[71] A. R. Offringa and other. The brightness and spatial distributions of terrestrial radio sources. *MNRAS*, 435:584–596, 2013.

[72] A. Oliver, A. Torrent, X. Lladó, M. Tortajada, L. Tortajada, M. Sentís, J. Freixenet, and R. Zwiggelaar. Automatic microcalcification and cluster detection for digital and digitised mammograms. *Knowledge-based Systems*, 28:68–75, 2012.

[73] N. Otsu. A Threshold Selection Method from Gray-Level Histograms. In *Trans. SMC*, volume 9, pages 62–66, 1979.

[74] J. M. Paredes, J. Martí, C. H. Ishwara-Chandra, J. R. Sánchez-Sutil, A. J Mu noz Arjonilla, J. Moldón, M. Peracaula, P. L. Luque-Escamilla, V. Zabalza, V. Bosch-Ramon, P. Bordas, G. E. Romero, and M. Ribó. Radio continuum and near-infrared study of the MGRO J2019+37 region. *A&A*, 507:241–250, 2009.

[75] W. D. Pence, L. Chiappetti, C. G. Page, R. A. Shaw, and E. Stobie. Definition of the Flexible Image Transport System (FITS), version 3.0. *A&A*, 524, 2010.

[76] B. Perret, S. Lefèvre, and C. Collet. A robust hit-or-miss transform for template matching applied to very noisy astronomical images. *Pattern Recognition*, 42:470–2480, 2008.

[77] B. Perret, S. Lefèvre, and C. Collet. Connected Component Trees for Multivariate Image Processing and Applications in Astronomy. In *Proc. ICPR*, pages 4089–4092, 2010.

[78] B. Perret, S. Lefèvre, C. Collet, and E. Slezak. Hyperconnections and hierarchical representations for grayscale and multiband image processing. In *IEEE Trans. on Image Processing*, volume 21, pages 14–27, 2012.

[79] G. L. Pilbratt, J. R. Riedinger, T. Passvogel, G. Crone, D. Doyle, U. Gageur, A. M. Heras, C. Jewell, L. Metcalfe, S. Ott, and M. Schmidt. Herschel Space Observatory. an ESA facility for far-infrared and submillimetre astronomy. *A&A*, 518:L1, 2010.

[80] W. H. Richardson. Bayesian-based iterative method of image restoration. *Journal of the optical society of America*, 62(1):55–59, 1972.

[81] R. S. Savage and S. Oliver. Bayesian methods of astronomical source extraction. *ApJ*, 661:339–1346, 2007.

[82] L. Shapiro and G. Stockman. *Computer Vision*. Prentice Hall PTR, Upper Saddle River, NJ, USA, 2001.

[83] M. J. Shensa. The discrete wavelet transform: wedding the à trous and mallat algorithms. In *IEEE Transactions on Signal Processing*, volume 40, pages 2464–2482, 1992.

[84] E. Slezak, A. Bijaoui, and G. Mars. Galaxy counts in the Coma supercluster field. *A&A*, 201:9–20, 1988.

[85] J. A. Smith et al. The u′g′r′i′z′ standard-star system. *AJ*, 123:2121–2144, 2002.

[86] J.-L. Starck. Multiscale Methods in Astronomy: Beyond Wavelets. *ASP Conference Series*, 281:391–400, 2002.

[87] J.-L. Starck, H. Aussel, D. Elbaz, D. Fadda, and C. Cesarsky. Faint source detection in ISOCAM images. *A&AS*, 138:365–379, 1999.

[88] J.-L. Starck and J. Bobin. Astronomical data analysis and sparsity: From wavelets to compressed sensing. In *Proc. IEEE*, volume 98 (6), pages 1021–1030, 2010.

[89] J.-L. Starck, D. L. Donoho, and E. J. Candès. Astronomical image representation by the curvelet transform. *A&A*, 398:785–800, 2003.

[90] J.-L. Starck, J. M. Fadili, S. Digel, B. Zhang, , and J. Chiang. Source detection using a 3D sparse representation: application to the Fermi gamma-ray space telescope. *A&A*, 504:641–652, 2009.

[91] J.-L. Starck and F. Murtagh. *Astronomical Image and Data Analysis (Astronomy and Astrophysics Library)*. Springer-Verlag New York, Inc., Secaucus, NJ, USA, 2006.

[92] P. B. Stetson. Daophot. a computer program for crowded-field stellar photometry. *PASP*, 99:191–222, 1987.

[93] A. S. Szalay, A. J. Connolly, and G. P. Szokoly. Simultaneous multicolor detection of faint galaxies in the Hubble Deep Field. *AJ*, 117:68–74, 1999.

[94] A. R. Taylor, S. J. Gibson, M. Peracaula, P.G. Martin, T.L. Landecker, C.M. Brunt, P.E.Dewdney, (...), and D. Durand. The Canadian Galactic Plane Survey. *AJ*, 125:3145–3164, 2003.

[95] A. R. Thompson, B. G. Clark, C. M. Wade, and P. J. Napier. The Very Large Array. *ApJS*, 44:151–167, 1980.

[96] C M. Trott, R. B. Wayth, J. P. R. Macquart, and S. J. Tingay. Source detection in interferometric visibility data. I. Fundamental estimation limits. *ApJ*, 731, 2011.

[97] University of Barcelona. Department of Astronomy and Meteorology. `http://www.am.ub.edu`, 2014. [Online; accessed January-2014].

[98] University of Barcelona. Institute of Cosmos Sciences. `http://icc.ub.edu/`, 2014. [Online; accessed January-2014].

[99] University of Barcelona. University of Barcelona. `http://www.ub.edu/web/ub/`, 2014. [Online; accessed January-2014].

[100] University of Girona. University of Girona. `http://www.udg.edu`, 2014. [Online; accessed January-2014].

[101] University of Jaén. Department of Physics. `http://www10.ujaen.es/conocenos/departamentos/fisica`, 2014. [Online; accessed January-2014].

[102] S. J. Vessey and D. A. Green. b | [the 7C(G) survey of radio sources at 151 MHz - The galactic plane at $80^\circ < l < 104^\circ$ and $126^\circ < l < 180^\circ$, for]. *MNRAS*, 294:607–614, 1998.

[103] VICOROB. VICOROB. `http://vicorob.udg.edu`, 2014. [Online; accessed January-2014].

[104] P. Vielva, E. Martínez-González, J. E. Gallegos, L. Toffolatti, and J. L. Sanz. Point source detection using the Spherical Mexican Hat Waveleton simulated all-sky Planck maps. *MNRAS*, 344:89–104, 2003.

[105] A. Vikhlinin, W. Forman, C. Jones, and S. Murray. Matched filter source detection applied to the ROSAT PSPC and the determination of the number-flux relation. *ApJ*, 451:542–552, 1995.

[106] W. M. Keck Observatory. W. M. Keck Observatory. `http://www.keckobservatory.org/`, 2014. [Online; accessed January-2014].

[107] M. C. Weisskopf, H. D. Tananbaum, L. P. Van Speybroeck, and L. O'Dell. Chandra X-ray Observatory (CXO): overview. In *Proc. SPIE*, volume 4012, 2000.

[108] M. W. Werner, T. L. Roellig, F. J. Low, G. H. Rieke, M. Rieke, W. F. Hoffmann, E. Young, J. R Houck, B. Brandl, G. G. Fazio, J. L Hora, R. D. Gehrz, G. Helou, B. T. Soifer, J. Stauffer, J. Keene, P. Eisenhardt, D. Gallagher, T. N. Gautier,

W. Irace, C. R. Lawrence, L. Simmons, J. E. Van Cleve, M. Jura, E. L. Wright, and D. P. Cruikshank. The Spitzer Space Telescope Mission. *ApJS*, 154:1–9, 2004.

[109] M. T. Whiting. Duchamp: a 3d source finder for spectral-line data. *MNRAS*, 421:3242–3256, 2012.

[110] R. Windhorst, D. Mathis, and L. Neuschaefer. The evolution of weak radio galaxies at radio and optical wavelengths. In *Evolution of the Universe of Galaxies*, volume 10 of *Astronomical Society of the Pacific Conference Series*, pages 389–403, 1990.

[111] C. Winkler. INTEGRAL. The international gamma-ray astrophysics laboratory. *A&AS*, 120:C637, 1996.

[112] A. Wootten and A. R. Thompson. The Atacama Large Millimeter/Submillimeter Array. *IEEE Proceedings*, 97:1463–1471, 2009.

[113] Y. Yang, N. Li, and Y.Zhang. Automatic moving object detecting tracking from astronomical CCD image sequences. In *Proc. ICSMC*, pages 650–655, 2008.

[114] C. Y. Zhang. Robust estimation and image combining. *ASP Conference Series*, 77:514–517, 1995.

[115] Y Zhang, A. Luo, and Y Zhao. Outlier detection in astronomical data. In *Proc. SPIE*, volume 5493, pages 521–529, 2004.